Simulation Based deposition Strategies Evaluation and Optimization in Wire Arc Additive Manufacturing

Mohammed Akram Chergui

Mohammed Akram Chergui. Simulation Based deposition Strategies Evaluation and Optimization in Wire Arc Additive Manufacturing. Chemical and Process Engineering. Université Grenoble Alpes [2020-..], 2021. English. NNT : 2021GRALI040 . tel-03273221

HAL Id: tel-03273221
https://theses.hal.science/tel-03273221v1

THÈSE

Pour obtenir le grade de

DOCTEUR DE L'UNIVERSITE GRENOBLE ALPES

Spécialité : **GI : Génie Industriel : conception et production**

Arrêté ministériel : 25 mai 2016

Présentée par

Mohammed Akram CHERGUI

Thèse dirigée par **Frédéric VIGNAT,** Maitre de Conférences HDR**,** UGA,
et codirigée par **François VILLENEUVE,** Professeur**,** UGA
et **Nicolas BÉRAUD,** Maitre de Conférences**,** UGA

préparée au sein du **Laboratoire des Sciences pour la Conception, l'Optimisation et la Production de Grenoble**
dans **l'École Doctorale I-MEP2 – Ingénierie – Matériaux, Mécanique, Environnement, Energétique, Procédés, Prodcution**

Evaluation et Optimisation des Stratégies de Dépôt en Fabrication Additive Arc-Fil basée sur la Simulation

Simulation Based Deposition Strategies Evaluation and Optimization in Wire Arc Additive Manufacturing

Thèse soutenue publiquement le **26 Mars 2021**,
devant le jury composé de :

Monsieur, Frédéric VIGNAT
MCF HDR, Université Grenoble Alpes, Directeur de thèse
Monsieur François VILLENEUVE
PROFESSEUR DES UNIVERSITES, Université Grenoble Alpes, Co-directeur de thèse
Monsieur Nicolas BÉRAUD
MCF, Université Grenoble Alpes, Co-encadrant
Monsieur Sylvain LAVERNHE
PROFESSEUR DES UNIVERSITES, École Normale Supérieure Paris-Saclay, Rapporteur
Monsieur Cyril BORDREUIL
PROFESSEUR DES UNIVERSITES, Université de Montpellier, Rapporteur et Président
Monsieur Thomas ELGUEDJ
PROFESSEUR DES UNIVERSITES, L'Institut National des Sciences Appliquées de Lyon, Examinateur

"He who finds a new path is a pathfinder, even if the trail has to be found again by others; and he who walks far ahead of his contemporaries is a leader, even though centuries pass before he is recognized as such."

Ibn Khaldun

Acknowledgments

And because it is not the destination that counts most, I would like to thank those who are dear to me and those with whom I have shared this journey.

First of all, I would like to thank all the members of the jury, who did me the honour of carefully studying my work. Thank you Cyril Bordreuil, Sylvain Lavernhe, and Thomas Elguedj for the discussion I had with you during my thesis defense, for your sharp feedback on my manuscript, and for providing me with a multitude of research leads for the coming years.

I would like to thank my thesis supervisors and my scientific family. Thank you Frédéric Vignat, for giving me the chance to work on such a fascinating topic. Thanks to you, I discovered the world of additive manufacturing and I ended up becoming passionate about it. Thank you for your guidance and your abundance of ideas and for always pushing me to my best. Thank you François Villeneuve, for the trust you have put in me, for your many advices and for all the hours you have devoted to supervise this research. I was extremely sensitive to your human qualities of listening and understanding throughout this work. Thank you Nicolas Béraud, for your guidance and support, for having contributed closely to the development of this work. I would also like to tell you how much I appreciated your great availability and your advice, and that you always had the right words.

I would also like to express my gratitude to my friends and PhD students in the laboratory, Mansour and Cédric, my co-offices, Amer, Tomek, and Manoch, as well as the whole additive manufacturing team, especially Maxime and Pascal. You have contributed enormously to my thesis being carried out in excellent scientific conditions and in a good general atmosphere due to the geographical proximity of our respective offices and their unwavering good humour, even in certain delicate moments.

Finally, I would like to thank those who are dear to me and who have accompanied me with their attention and encouragement throughout these years. I would like to thank my family, who have always surrounded me, who have given me so much and continue to do so. I am indebted to my parents, to whom I owe everything, for their moral and material support and their unfailing confidence in me and in my choices. Thank you Malika for the person that you are, for believing in me, and being there for me all the time, no matter the distance. Thanks to my two little sisters, for the big brother look that you continue to give me, and for the confidence that you instil in me. Thank you aunt Malika for your constant support and for always believing in me. I have a special thought for my grandfather Boucif, and my uncle Mohammed, whose memory I will never forget. It was a pleasure to know you and a privilege to bear your name. I finally thank those people whose role goes far beyond that of friend, Habib, Amine, Ryadh, Taha, Sofiane, Larbi, Bassim, Yahia, Yacine, Boucif, Youcef and Hichem.

Contents

List of Figures

List of Tables

Introduction

Wire arc additive manufacturing (WAAM) enables the production of metallic parts by depositing beads of weld metal, layer-by-layer, using arc-welding technologies. Combined of an electrical arc as a heat source and a wire as feedstock, this technology has the ability to manufacture large parts at a high deposition rate. However, the quality of the obtained parts is greatly affected by the various thermal phenomena present during the deposition process such as heat accumulation, and changing substrate temperature. The quality of the fabricated parts can be evaluated from two aspects, the geometric accuracy and the material integrity, and can vary drastically depending on the deposition strategy chosen, because it shapes the part's thermal history during the manufacturing process. Numerical simulation remains an effective tool in order to tackle such issues. In this study, a thermal simulation model is built in order to investigate the thermal behavior in WAAM process, based on a novel metal deposition technique. Afterwards, a set of thermal quality criteria is developed based on the proposed simulation model, allowing a better prediction of the different defects in WAAM parts. Finally, a simulation-based optimization method is proposed in order to optimize deposition strategies in WAAM process, with the aim of improving the quality of the fabricated parts. In this method, the part's desired thermal history is dictated by adjusting the deposition strategy parameters along the deposition path. The optimized strategies are determined using the previously developed thermal simulation, with respect to the different thermal quality criteria. The overall method is validated by series of experiments, and has proven effective in predicting quality and optimizing deposition strategies in WAAM.

Context

Additive Manufacturing

Additive Manufacturing (AM) is the process of joining materials to make parts from 3D model data, layer upon layer, as opposed to subtractive and formative manufacturing technologies (ISO/ASTM, 2015). Additive manufacturing takes its roots from rapid prototyping, developed for creating models and prototype parts. The latter is known as the first form of creating a 3D object, in a layer-by-layer manner, using Computer-Aided Design (CAD) (Wong and Hernandez, 2012). Nevertheless, additive manufacturing has experienced a remarkable growth over the last three decades, and its use is no longer limited to the production of prototypes, but is now intended for the direct manufacturing of functional metal parts (Vayre et al., 2012). In fact, the recent fast growth rate of AM among industrials and researchers in several fields is proof that it has the potential to be an effective technology for manufacturing components and final products (Pour et al., 2016). Based on its maturity in some extent, AM becomes today a main technology in some manufacturing contexts since it can be used in several application fields, especially in customized production, thanks to its ability to manufacture designed parts with complex geometries without using fixtures, tooling, or mold (Zhang et al., 2014).

Additive manufacturing methods and processes are increasing in terms of industrial applications such as automotive, aerospace, and medical, and this growth is expected to continue over the next few years (Bikas et al., 2015). The AM processes are very numerous and can be classified according to different criteria: the material feed stock, energy source, build volume. (Frazier, 2014) reviewed the metal additive manufacturing technologies, and classified these processes into three main categories: (i) powder bed systems, (ii) powder feed systems, and (iii) wire feed systems. But overall, the different AM processes can be categorized into two main groups:

- Powder Bed Fusion (PBF): Processes in which a heat source (e.g. laser, electron beam) is applied to selectively fuse the material in powder form into the desired shape. The powder is contained in a powder bed that is progressively indexed downwards as each layer is completed, and new powder is spread over the build area.

- Direct Energy Deposition (DED): Processes in which a heat source is used to fuse the material (wire or powder) by melting it as it is deposited, i.e. the deposition and melting of the material are carried out simultaneously.

In this manuscript, the focus will be on Wire Arc Additive Manufacturing. This AM technology is one of the most promising direct energy deposition processes. Compared to other additive manufacturing processes, this technology is inexpensive, offers a large workspace and allows for high productivity and energy efficiency. All the studies described in this manuscript were performed on a WAAM cell. The work presented in this thesis was carried out in the G-SCOP laboratory, and the WAAM cell is hosted by S.mart Grenoble Alpes.

Wire Arc Additive Manufacturing (WAAM)

WAAM enables the production of metallic parts by depositing beads of weld metal, in a layer-by-layer fashion, using arc-welding technologies. It combines an electrical arc as a heat source and a metal wire as feedstock. As illustrated in Figure 0.1, The wire is melted by the electric arc and then fed into the molten pool following a predefined path to form the desired structure.

Currently, WAAM combines standard and off-the-shelf equipment, namely:

- Welding equipment: welding power source and welding torches (e.g. gas metal arc welding (MIG/MAG)), and wire feed systems.
- Positioning and motion systems: robotic systems (multi-axis robots), computer numerical control systems (CNC milling machines).

WAAM has made enormous progress thanks to the increasingly advanced development welding equipment. This being the case of Fronuis Cold Metal Transfer (CMT) process. CMT is an improved version of MIG/MAG welding, based on a short-circuiting transfer process in which the droplet detachment is assisted mechanically, and thus ensuring a lower heat input to the base material and spatter free metal transfer.

In practice, WAAM has revealed many advantages compared to other additive and traditional manufacturing processes, especially in the manufacture of large and complex thin-walled structures, for instance:

- It allows high deposition rates (about 50–130 g/min compared to 2–10 g/min for electron beam or laser deposition (Liberini et al., 2017)).

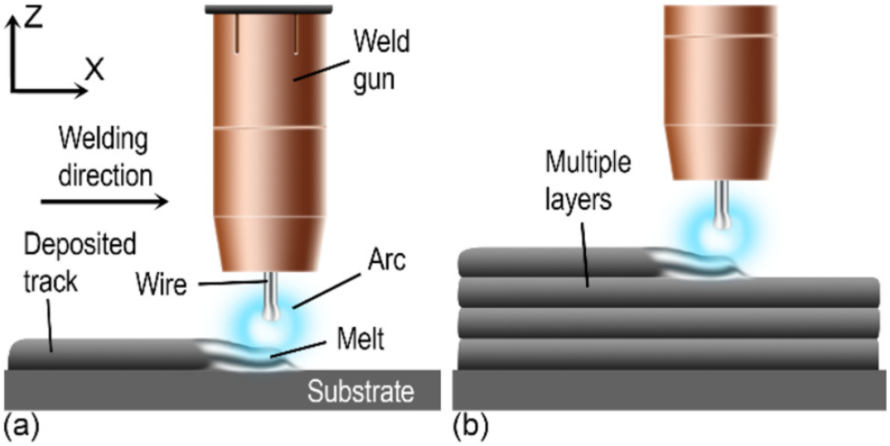

Figure 0.1: Illustration of Wire Arc Additive Manufacturing: (a) initial single layer; (b) subsequent multiple layers (Näsström et al., 2019).

- It enables to manufacture large-scale parts in a large workspace (theoretically there are no dimensional limits for the manufactured parts (Derekar, 2018)).
- It allows the use of a wide range of materials (any metal that can be welded, including aluminum alloys, stainless steel, nickel-based alloys, titanium alloys, etc).
- It reduces production time (reduces manufacturing time by 40-60% and post-machining time by 15-20% depending on part size (Wu et al., 2018)).
- Low equipment and operation costs (about 100 to 500k€ compared to 600 k€ to 1.5M€ for powder bed processes and 800 k€ to 2 M€ for powder spraying (Campocasso et al., 2017)).

Problematic (thermal influence)

Despite the promising advantages of WAAM process, the quality of parts manufactured using this AM technology is greatly affected by the various thermal phenomena present during the manufacturing process. For instance, the non-uniform temperature field experienced by the part during the deposition process, the constantly changing thermal conditions, heat accumulation and overheating phenomena, which could lead to several geometrical and material defects in the final parts (e.g. variation in layer dimensions, structural collapses, residual stress and distortions, porosity formation). In fact, it is well accepted that the quality of WAAM parts highly depends on their thermal history during the manufacturing process (Wu et al., 2018; Zhao et al., 2020; Montevecchi et al., 2018; Derekar, 2018).

The thermal history of parts manufactured by WAAM is strongly dictated by the deposition strategy according to which they were deposited. In fact, a part's final quality can vary drastically depending on the deposition strategy chosen, namely, the deposition path along with the different deposition parameters, such as: heat input, travel speed, wire feed speed, arc current and idle-times between layers. For instance, manufacturing the same part according to two different deposition strategies can lead to two different qualities in the final part. In order to illustrate the influence of deposition strategies on the quality of manufactured parts, two examples are provided in the following:

The first example consists of manufacturing a 60-layers thin-walled part according to two different strategies : Strategy 1 and Strategy 2. The strategy parameters are identical for both strategies, except for the idle-time (cooling time between layers), which changes from 2 seconds in Strategy 1, to 30 seconds in Strategy 2. The deposited parts, illustrated in figure 0.2, show a great difference in geometrical quality. Indeed, a significant variation in the layers' width can be observed in the part manufactured according to strategy 1, compared to that manufactured according to S2. In addition, a significant difference in total height can be found between the two thin-walled parts.

In the second example, a "V" thin-walled structure was manufactured according to three different strategies: Strategy 1, Strategy 2 and Strategy 3. Only this time, the deposition path was varied between the three strategies, while all other deposition strategy parameters are kept constant. The three deposition trajectories along with the three fabricated parts are shown in Figure 0.3, where different geometric defects can be observed in the final parts.

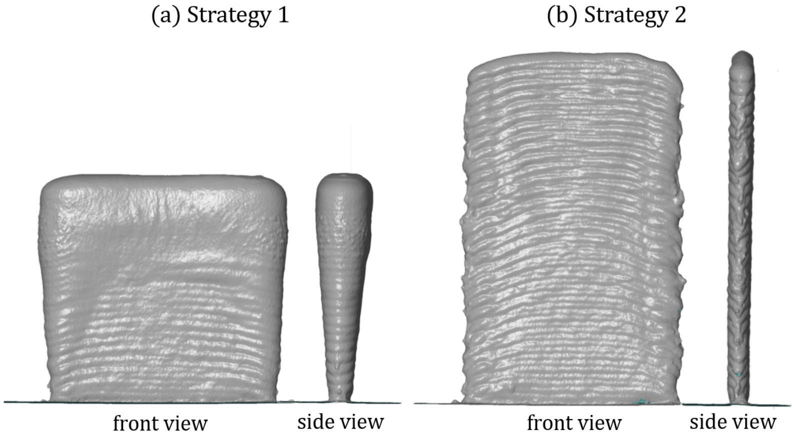

Figure 0.2: Thin-wall part fabricated according to: (a) Strategy 1; (b) Strategy 2

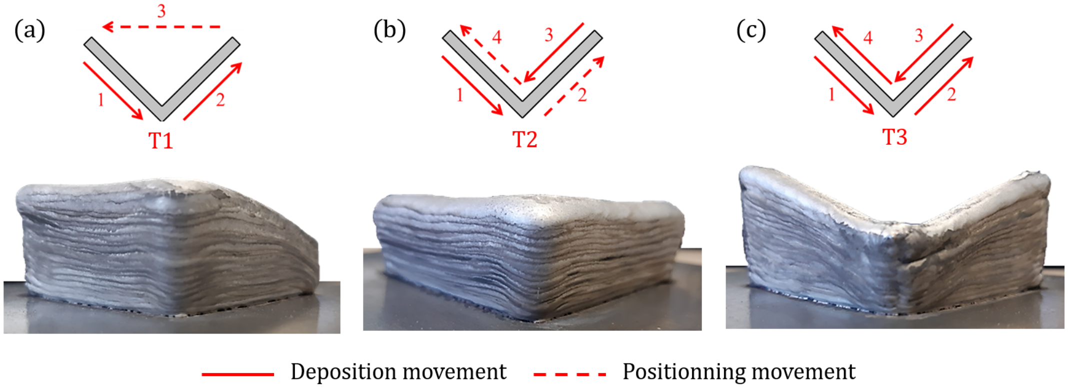

Figure 0.3: "V" Thin-walled part fabricated according to: (a) Strategy 1; (b) Strategy 2; (c) Strategy 3

These two examples clearly show the influence of WAAM deposition strategies on the thermal history of the deposited parts and thus on their final quality.

Research question and motivation

As highlighted in the previous section, the major problem limiting the widespread adoption of WAAM process is the difficulty in controlling the quality of the produced parts (i.e., geometric accuracy and material integrity) due to the inherently complex thermal nature of the process. A quality that is known to vary considerably depending on the deposition strategies, as they shape the thermal history of the parts during deposition. Therefore, optimization of WAAM deposition strategies appears to be a promising approach for a better quality control in WAAM, which leads to the main research question:

How to control and optimize WAAM deposition strategies in order to manage the quality of the deposited parts ?

The ultimate goal of this study is to guarantee the quality of WAAM deposited parts by optimizing their deposition strategies, in a reasonable time and at a lower cost. However, this optimization can only be achieved if the quality defects as well as the thermal phenomena at their origin are understood and can be controlled. Therefore, the understanding of the thermal behavior of WAAM process is a step of paramount importance towards its optimization. This understanding can be gained either by simulation or experimentation. The latter approach requires the execution of several experiments that can be costly and time consuming. As for simulation, and although it allows access to more details regarding the thermal behavior of the process, the current models seem unable to simulate an entire deposition strategy in reasonable time and with sufficient accuracy allowing for its off-line optimization. Therefore, in order to answer to the previous research question, this study will first need to address the following underlying questions:

How to simulate the thermal behavior of WAAM process in a reasonable time allowing for its optimization ?

How to evaluate the quality of WAAM produced parts using process simulation ?

How to optimize WAAM deposition strategies using simulation ?

Thesis approach

In order to answer the main research question of the study, a simulation-based deposition strategy optimization approach is proposed in this manuscript. The basic idea of this approach is to dictate the part's desired thermal history by adjusting the strategy parameters along the deposition path. The optimal deposition strategy is determined based on a thermal simulation of the process, with respect to a set of thermal quality criteria ensuring the quality of the produced parts. As illustrated in Figure 0.4, the approach is composed of three main steps, each of which addresses one of the three underlying questions (the detailed operation of the approach will be described in chapter 4).

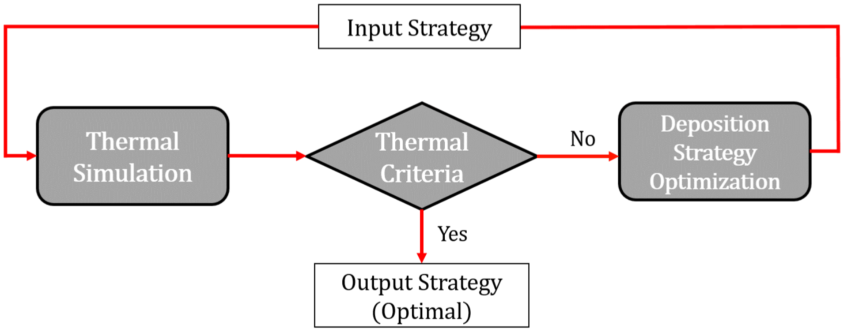

Figure 0.4: Proposed simulation-based deposition strategy optimization approach

The present research study will therefore focus on the development of these three main steps:

- **Thermal simulation:** Development of a finite element model allowing to simulate the entire thermal history of a given deposition strategy and a deeper understanding of the thermal behavior of parts fabricated in WAAM.
- **Thermal quality criteria:** Development of a set of thermal quality criteria allowing a better prediction of the main defects affecting the quality of WAAM fabricated parts, and the evaluation of deposition strategies.
- **Deposition strategy optimization:** Proposition of optimization techniques, in which the deposition strategy parameters are optimized based on the results of the thermal simulation, with respect to the thermal quality criteria.

Manuscript content

The present manuscript will be organized as follows:

Chapter 1 is devoted to the development of a thermal simulation model in order to investigate the thermal behavior of parts manufactured in WAAM using finite element method. Since WAAM process simulation has already been addressed in literature, the focus will be on the development of a part-scale thermal simulation allowing to achieve a compromise between the computational costs and the precision required for the off-line optimization of the process. The existing models will be briefly reviewed and their limitations will be discussed. Afterwards, the various proposed modeling and computational techniques used in the model will be detailed. Finally, the effectiveness of the proposed model will be validated with an experimental test case, and the results will be presented.

Chapter 2 will focus on the study of the main defects affecting the quality of WAAM parts using the proposed finite element simulation. First, the most common quality defects encountered in WAAM are reviewed and the thermal phenomena at their origin are identified. Then, a set of thermal quality criteria will be proposed in order to predict these defects and evaluate the quality of the fabricated parts. The relevance of the proposed thermal criteria will be checked by means of an experimental validation, by comparing the results of the thermal criteria to the measurements of the different defects performed on two test-case parts.

Chapter 3 proposes two simulation-based deposition strategy optimization techniques in order to improve the quality of the fabricated parts. In these techniques, two different strategy parameters are adjusted in order to dictate the desired thermal history in the fabricated parts. The different stages of the optimization technique will be described, and the optimization results will be presented.

Chapter 1

Thermal simulation of WAAM process

1.1 Introduction

In this chapter, a thermal simulation is developed in order to investigate the thermal behavior of parts manufactured in WAAM. Within the framework of its use, the objective is to understand the physical behavior of the process and the influence of its parameters on the quality of the fabricated parts. That, in a second step, this will allow for the best possible optimization of these parameters. For this purpose, the knowledge of the thermal history seems sufficient to evaluate the quality of the produced parts in terms of geometric accuracy and material integrity. This statement will be demonstrated by the different studies discussed in the following section, and will be further validated in chapter 2. This chapter therefore details the main modelling and computational techniques used to simulate the entire thermal history of a given deposition strategy, within a reasonable time. The proposed model is based on a novel FE metal deposition technique, allowing to gradually construct the mesh representing the deposited regions along the deposition path. The proposed technique is combined with an adapted heat source model, originally proposed by (Goldak et al., 1984) in order to model material and heat input in WAAM process simulation. The proposed method allows not only to take into account the energy distribution between the filler material and the molten pool, but also to consider the changing in the boundary conditions during the deposition process using a model-update procedure. The overall model is validated with an experimental test case, and the results are presented.

1.2 State of the art

“Only the fundamental understanding of a manufacturing process allows for its optimization”(Klocke et al., 2002). This understanding can be gained either by experimentation or simulation. Simulation has proven to be an effective and a valuable tool to build the necessary knowledge in different manufacturing processes, such as machining, electrical discharge machining (EDM), extrusion... Not only it provides a low cost, secure, and a fast analysis tool allowing for the system's behavior to be learnt and tested (F. Hosseinpour and H. Hajihosseini, 2009), but it provides deeper insights on the different physical phenomena governing the manufacturing process. An output barely achieved by means of experimentation.

(Smith, 2003)defines simulation as the development of descriptive computer models of a system and exercising those models to predict the operational performance of the underlying system being modeled. Models are the abstract representation of a process that establishes a relation between input and output quantities (Bikas et al., 2015), and can be categorized into three main categories, namely analytical, empirical and numerical models. The same authors reviewed the different process modelling approaches of additive manufacturing processes, and found that the most utilized modeling approach for dimensional accuracy related issues is by using empirical models, while mechanical properties and dimensional stability problems are usually studied using numerical heat transfer models. In the same perspective, (Stavropoulos and Foteinopoulos, 2018) reviewed the different modelling approaches of additive manufacturing processes, and underlined the importance of modelling heat transfer related phenomena as it directly impacts the dimensional accuracy, topology, mechanical properties and microstructure of the final part. They also stated that numerical approaches remains the most suitable for modelling such phenomena, as they provide an overview of the physics of the whole duration of the process, requiring less assumptions compared to analytical approaches that are not always able to solve the whole system. Therefore, the knowledge of the entire thermal history of the part will allow a better understanding of the part's thermal related issues, and the best possible optimization of the process.

Numerical methods can be categorized into two main groups: (i) “Mesh-free methods” such as smoothed particle hydrodynamics (SPH) and element free Galerkin method (EFGM); and (ii) “Mesh-based methods” such as finite element method (FEMs), boundary element methods (BEMs), and finite difference methods (FDMs) (Parandoush and Hossain, 2014). Numerical methods have proven to be an essential tool for solving multiple physical problems in almost every engineering field, including additive manufacturing. For instance, (Foteinopoulos et al., 2018) proposed to model the thermal history of parts manufactured in powder bed fusion additive manufacturing (PBF) processes using finite difference method (FDM). (Ganeriwala and Zohdi, 2016) developed a coupled discrete element-finite difference model of selective laser sintering (SLS) process, where the powder particles are modeled as discrete, thermally and mechanically interacting spheres, while the solid underneath substrate is modeled via the finite difference method. (Xia et al., 2016) proposed a transient three-dimensional powder-scale model in order to investigate the thermo-dynamics, heat and mass transfer and surface quality within the molten pool during selective laser melting (SLM) using finite volume method (FVM). Among all these methods, finite element method has proven to be the most popular for studying the physical behavior of the different additive manufacturing processes, and became the most common technique for predicting the porosity, the residual stress and the distortions in the additively produced parts (Schoinochoritis et al., 2016).

Finite element (FE) method, originally introduced by (Turner et al., 1956), relies on the discretization of a domain (a continuum of matter with a known boundary) into a finite number of subdomains, called elements, for which the systematic approximated solution is constructed. And thus, reducing the problem to that of a finite number of unknowns (Madenci and Guven, 2006). There are several FE models and techniques in the literature for modelling and simulation of the various additive manufacturing processes. The state-of-the-art FE models in the simulation of powder bed fusion processes were reviewed by (Luo and Zhao, 2018) and (Schoinochoritis et al., 2016) . A focus on the FE thermal analysis methods in SLS and SLM processes was presented by (Zeng et al., 2012), while FE models for electron beam melting (EBM) process were reviewed by (Galati and Iuliano, 2018). Other studies also relate to the simulation of direct energy deposition (DED) processes using FE method. For instance, (Stender et al., 2018) proposed a thermal-mechanical FE workflow for direct energy deposition additive manufacturing process modeling. Another finite element based methodology for modeling the thermal and mechanical behavior of metal (Ti-6Al-4V) in laser engineered net shaping (LENS) process was also presented by (Yang et al., 2016). The common goal of these models is to understand the physical behavior of the different AM processes and study the effect of process parameters on the mechanical properties, dimensional accuracy, and metallurgical integrity of the produced parts. Thus allowing the selection of the optimal process parameters while minimizing the manufacturing costs.

In WAAM process modeling and simulation, the objectives remains the same as for other AM processes. Eventhough existing numerical models are not yet state of the art (Graf et al., 2018), the studies carried out to date have drawn major conclusions on the thermal and the thermo-mechanical behavior of parts produced in WAAM, and the influence of the non-homogenous thermal phenomena on the part's quality in terms of mechanical properties and final dimensions. (Xiong et al., 2017, 2018) studied the influence of substrate preheating on the thermal behavior of cylindrical thin-walled parts made by WAAM using a thermal FE model. Another FE model was proposed by (Montevecchi et al., 2016)and validated by comparing the measured distortions of a WAAM tests-case with the simulated ones. Nevertheless, the high computational cost of the FE simulation remains an important drawback preventing its application in process optimization for example. For this reason, some studies aimed to improve efficiency and reduce the computational time in finite element modeling of WAAM process. (Ding et al., 2011) proposed a finite element approach based on two models (transient and stationary) in order to investigate the thermomechanical behavior of parts manufactured in WAAM, and showed that the steady-state thermal model allows to reduce the computational time by 80%. In the same perspective, (Montevecchi et al., 2017) developed a FE model based on a mesh coarsening technique in order to reduce the computational cost of the process simulation. (Michaleris, 2014) reviewed the existing techniques for metal deposition modeling, and proposed a new hybrid algorithm in order to reduce the computational time. These techniques can significantly reduce the computational time, but this can be detrimental to the accuracy of the results. Therefore, a trade-off must be found between the computational costs and the precision required for a given application.

Recall that the interest of opting for numerical methods to simulate a manufacturing process is the possibility of simulating a complete manufacturing entity throughout its manufacturing process, which will allow to optimize the manufacturing process afterwards. However, the set of FE models developed so far for WAAM process do not seem to be up to the task, for several reasons:

- It is difficult to simulate an entire deposition strategy of a large-scale part in a reasonable time because of the imposing size of the mesh (i.e., the high number of degrees of freedom (DOFs)) to consider, and the important number of simulation time-steps to run. Moreover, taking into account the phase change in the simulation requires a refined mesh around the molten pool, as well as an extremely short time-steps in order to ensure the convergence and stability of the simulation. This will result in an extremely high computational time, even if adaptive time-steps and mesh coarsening techniques are applied to the model.

- The finite element modelling techniques adopted in existing models, such as material deposition modelling techniques, and assumptions made to simplify the consideration of boundary conditions, can be a major source of errors in the finite element analysis depending on the geometry of the part to be simulated, which calls into question the accuracy of the obtained results and the reliability of these techniques.
- Existing models are often implemented via commercial simulation softwares, which hinders the possibility of considering other modeling techniques or improvements, and in some cases it would be impossible to simulate a part according to a given deposition strategy, or even less to vary the strategy parameters during the simulation. Moreover, this rigidity imposed by commercial simulation softwares completely restrain the possibility of integrating optimization or correction algorithms within the simulation.

These limitations will be illustrated gradually in this manuscript, where other solutions will be proposed. Thus, a high-performance finite element simulation for WAAM process, enabling its off-line optimization in order to improve the quality of the produced parts while minimizing the manufacturing costs, must meet the following specifications:

- A macro-scale simulation: the finite element analysis must extend to the part-scale level, thus enabling to simulate complete deposition strategies of a given part.
- An adequate trade-off between accuracy and computational efficiency: simulation results must be obtained within a reasonable time, with sufficient accuracy for process parameters optimization.
- Flexibility: the simulation must enable the part to be simulated regardless of its deposition strategy, with the possibility to adjust these parameters internally, by integrating optimization algorithms into the simulation.

In the following, the development of a finite element simulation meeting the above specifications is detailed.

1.3 Finite element modelling for WAAM process

A finite element simulation workflow was proposed by (Schoinochoritis et al., 2016) describing the different stages of a typical finite element simulation, including the pre-processing, the processing, and the post-processing stage. This workflow is illustrated in Figure 1.1.

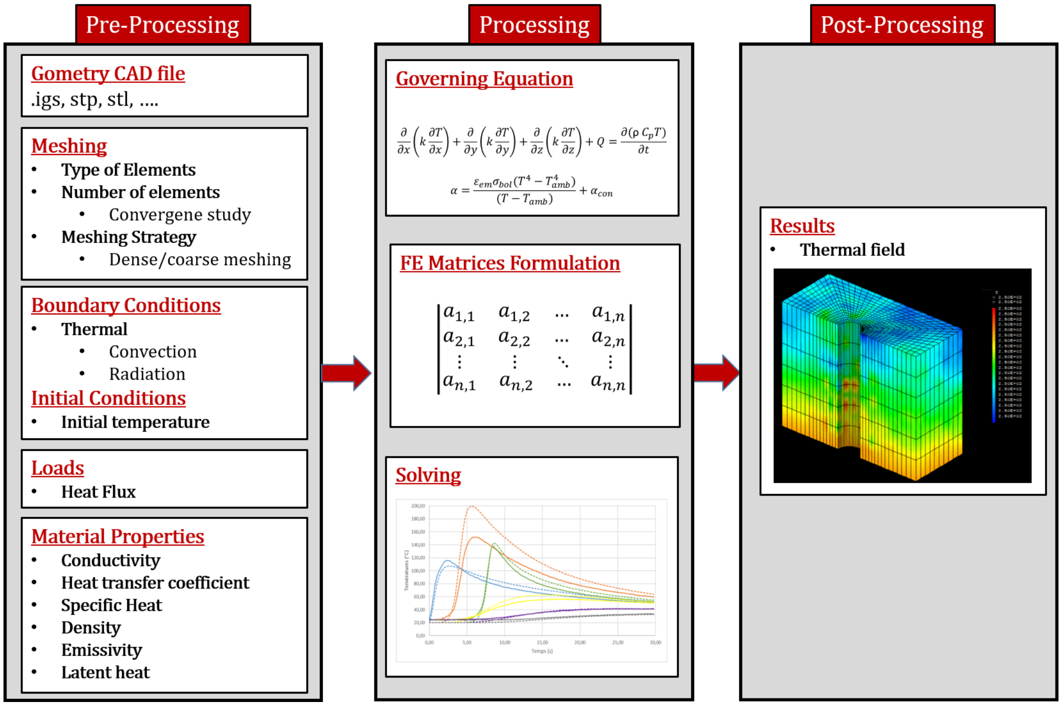

Figure 1.1: Finite element analysis workflow adapted from (Schoinochoritis et al., 2016)

In finite element simulation of additive manufacturing processes in general, and of WAAM in particular, the pre-processing stage is of a main importance due to the nature of the process, i.e. the layer-by-layer material deposition feature. In fact, the pre-processing inputs including, the mesh, the heat input, the material properties and the boundary conditions are changing constantly during the deposition process, which requires special modelling techniques. Therefore, WAAM process modelling efforts should focus on addressing the following issues:

- How to model material input ?

- How to model heat input ?
- How to consider the changing in boundary conditions and material properties ?

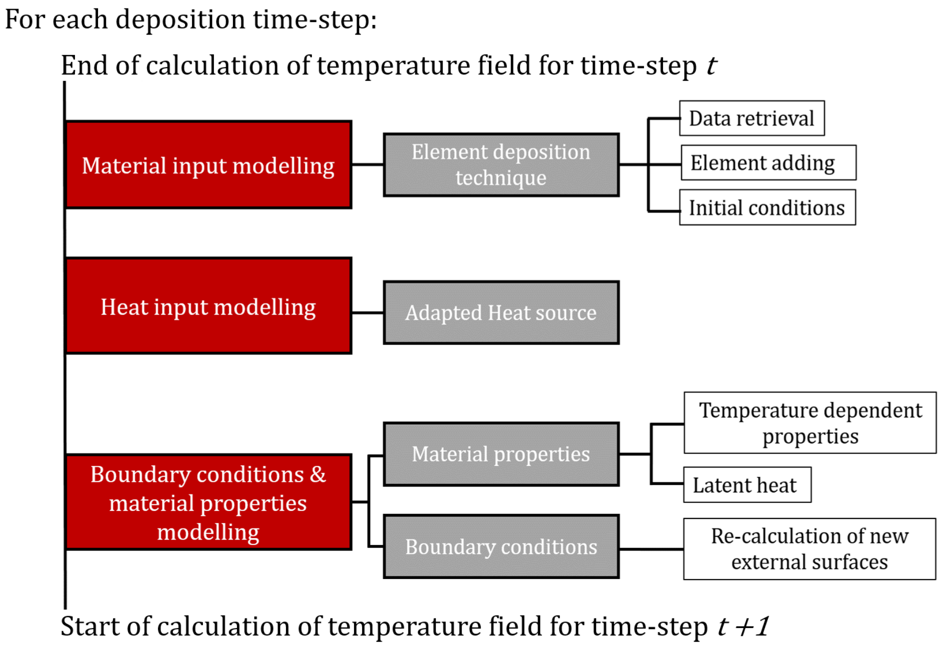

Figure 1.2: Proposed FE model workflow for WAAM process

In order to address the aforementioned questions, a finite element model is proposed in this chapter based on a new metal deposition modeling technique. The main objective of this model is to incorporate the metal deposition feature of the process by taking into account the constantly evolving pre-processing inputs in the finite element analysis of the deposition phase. Indeed, the proposed model consists of three main steps, allowing each to properly model the material input, the heat input, the material properties and the boundary conditions, respectively. Each step includes a set of functions and procedures that are called in the order between each two time steps in the deposition phase simulation, as illustrated in Figure 1.2. These functions and procedures allows to update the pre-processing inputs at each deposition time-step, based on which the temperatures fields are calculated and stored successively. Consequently, the mesh representing the deposited layers as well as the corresponding temperature maps are constructed gradually according to the deposition path.

In the following sections, the three main stages of the proposed FE model are detailed. The model is implemented using the open-source finite element code "Cast3M 2018". The latter uses an object-oriented programming language, called Gibiane, to describe data and operations, and independently supports the processing stage including the finite element formulation and solving. Cast3M is also a meshing and a results visualization program, and unlike most commercial finite element softwares, it allows a great programming flexibility, which facilitates the implementation of the different modelling techniques and procedures. The post-processing stage, including results visualization and analysis, is performed using "ParaView" software. The latter enables to explore data interactively in 3D or by programming using qualitative and quantitative techniques.

1.3.1 Material input modeling (Meshing)

1.3.1.1 Existing techniques

There are two finite element techniques for modeling material deposition in additive manufacturing process simulation, namely: (i) inactive element method and (ii) quiet element method, as reviewed in literature by (Michaleris, 2014).

In the quiet element method, all elements are present from the start of the analysis, but low values are assigned to their material properties (conductivity k and specific heat C_p), so they do not affect the analysis. These material properties are then switched to the real values according to the deposition path:

$$k_{quiet} = s_k k \tag{1.1}$$

$$C_{p_{quiet}} = s_{c_p} C_p \tag{1.2}$$

Where $k_{quiet}$and $C_{p_{quiet}}$ are the quiet values of thermal conductivity and specific heat respectively, $s_k$and $s_{c_p}$are the scaling factors. This method can be easily implemented using commercial finite elements codes via subroutines, and no equation renumbering and additional solver initialization are required since all elements (both active and quiet) are considered in the analysis. However, taking into account the entire mesh size representing all layers to be deposited from the start of the analysis leads to a significant increase in the computational time.

Moreover, the scaling factors s_k and s_{c_p} are likely to introduce errors into the finite element analysis if not well defined.

In the inactive element method, the elements representing the deposited regions are initially inactive (i.e. removed from the analysis), and activated gradually according to the deposition path. The advantage of this method is that only active elements (active nodal DOFs) are considered in the finite element analysis, resulting in smaller algebraic systems to solve. This would considerably reduce the computational time, even though equation renumbering and solver initialization are required after each element activation time-step. Nevertheless, this method cannot be implemented easily using commercial simulation softwares, and errors can still be introduced into the finite element analysis because of the artificial numerical thermal energy introduced during element activation.

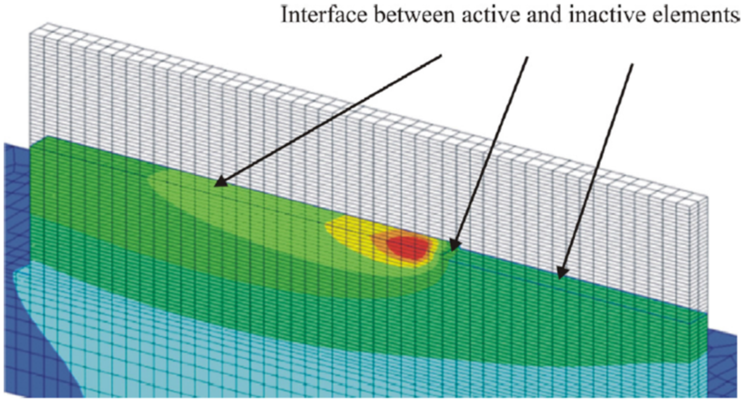

Figure 1.3: Interface between inactive and active elements (Michaleris, 2014)

Eventually, both inactive and quiet methods can be used to model metal deposition in WAAM process, and each presents some advantages over the other. But also some disadvantages such as introducing errors into the finite element analysis, and taking a longer time to run. But more importantly, the interface between inactive (or quiet) and active elements, illustrated in Figure 1.3, is continuously evolving during the deposition phase, making it difficult to compute this internal interface and consider its surface convection and radiation. For this reason, convection and radiation on this interface are neglected on both inactive and quiet element techniques, leading to additional errors in the finite element analysis (Michaleris, 2014). These errors depend on the geometry of the part to be simulated, and may be minor if the size of the interface is negligible. But generally, this interface is quite significant and constantly evolving in WAAM of large-complex parts, which leads to increased errors.

1.3.1.2 Proposed technique: Element deposition technique

In the present model, metal deposition is taken into account using a new finite element technique called “element deposition technique”. In this technique, each deposited droplet is modeled by a set of elements, representing together a numerical droplet. Every numerical droplet is created at its corresponding time-step in the deposition phase simulation. The new created elements are then added to the elements already created in the previous time-steps. Thus, the mesh representing the deposited regions is constructed gradually along the deposition path.

This technique is implemented in the finite element code through different functions and procedures that are summarized in the following steps, and illustrated in Figure 1.4:

- Data retrieval: this procedure consists in recovering the mesh as well as the temperature field, at a given time-step *t,* in the deposition phase simulation. This temperature field as well as the associated mesh corresponds to the already deposited regions, and will be used as input data in the next steps.

- Elements adding function: this function handles the mesh. In fact, it enables to create, for each time-step in the deposition phase, a numerical droplet (i.e. a set of elements representing the deposited droplet). These elements are then added to the existing mesh (substrate mesh) at their corresponding position, as defined by the deposition path. The duplicated nodes at the interfaces between the substrate mesh and the new numerical droplet are removed, and the two meshes are subsequently merged into one.

- Initial conditions update: Once the new mesh is constructed, the previously retrieved temperature field is applied to the mesh representing the already deposited regions. A uniform temperature field is also applied to the new deposited elements. The value of this temperature field is calculated based on the energy attributed to the new deposited elements and is called deposition temperature ($\mathrm{T_d}$). The new constructed mesh and temperature field will be therefore selected as input mesh and initial temperature field for temperature calculation of the next deposition time-step (time-step t+1).

(The calculation of the deposition temperature will be detailed in the next section).

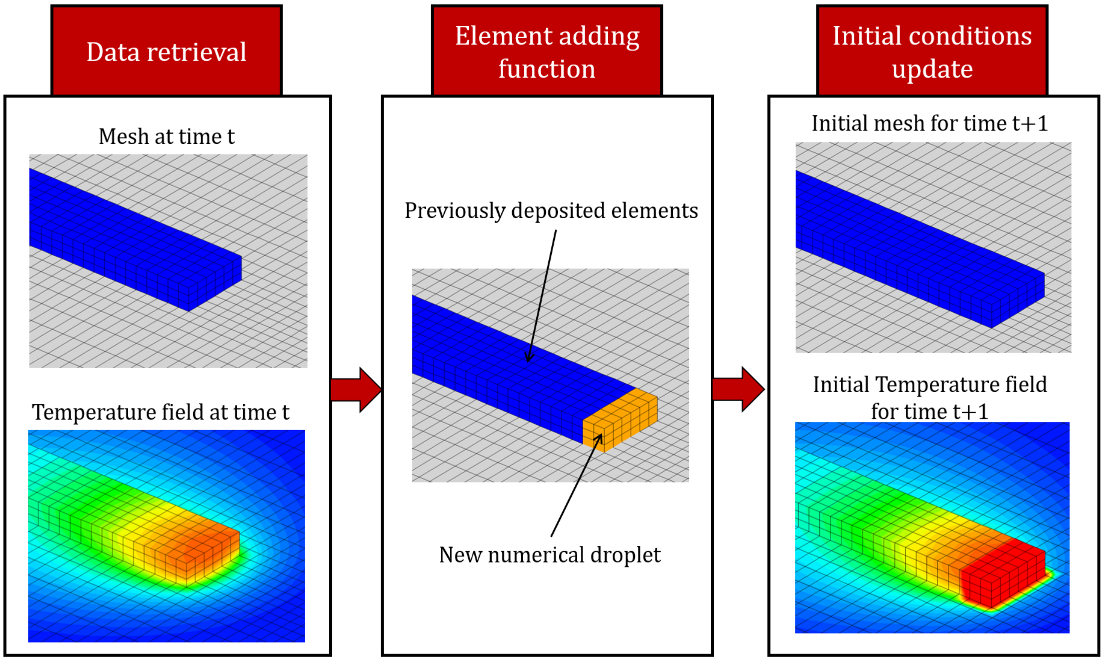

Figure 1.4: Main steps of element deposition technique

1.3.2 Heat input modeling

From the perspective of a simulation, WAAM process is very similar to multi-pass welding process (Xiong et al., 2018). However, the physics of welding process put forward some complex physical phenomena, involving thermodynamics, heat and mass transfer, electricity and magnetism (Hu and Tsai, 2007). Modeling such phenomena at a part scale level can be costly due to the unreasonable computational time requirements. For this reason, most studies in literature recommend to model the heat input using a heat source model, prescribing a heat generation per unit volume, and taking into consideration the energy contribution of the different physical phenomena occurring in the molten pool.

1.3.2.1 Double-ellipsoidal heat source model

(Goldak et al., 1984) proposed a volumetric heat source model in the form of a double-ellipsoidal, defined in a moving frame of reference, as shown in Figure 1.5.a, where x axis is oriented in the deposition direction. The model is defined by two Gaussian distributed power densities (Figure 1.5.b), allowing to better take into account the heat distribution asymmetries in the molten pool.

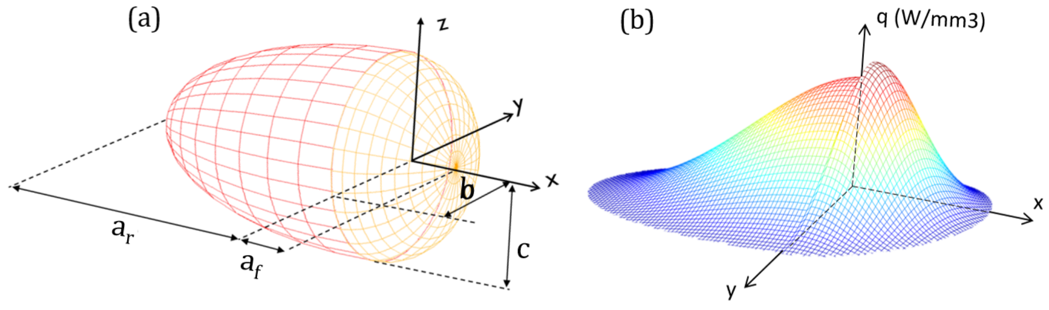

Figure 1.5: Goldak double-ellipsoidal heat source

The power density distributions in the front and rear half of the source are expressed by the following equations:

$$for\ x > 0;\ y \epsilon]-\infty, +\infty[;\ z \epsilon]-\infty, +\infty[:$$

$$q_f(x,y,z) = \frac{(6\sqrt{3}f_f Q)}{(\pi a b a_f \sqrt{\pi})} exp(-3\frac{x^2}{a_f^2} - 3\frac{y^2}{b^2} - 3\frac{z^2}{c^2}) \tag{1.3}$$

$$for\ x < 0;\ y \epsilon]-\infty, +\infty[;\ z \epsilon]-\infty, +\infty[:$$

$$q_r(x,y,z) = \frac{(6\sqrt{3}f_r Q)}{(\pi a b a_r \sqrt{\pi})} exp(-3\frac{x^2}{a_r^2} - 3\frac{y^2}{b^2} - 3\frac{z^2}{c^2}) \tag{1.4}$$

Where q_f and q_r are the power density distributions in front and rear the center of the arc (origin of the frame of reference, as shown in Figure 1.5), respectively. b and c are the half-width (y semi-axis) and the depth (z semi-axis) of the source, a_f and a_r are the lengths of the front and rear ellipsoids (x semi-axes), respectively. Q is the total power supplied by the arc, and is expressed in equation (1.5) as the product of welding current I, welding voltage U, and arc efficiency η. f_f and f_r are the heat distribution factors of the front and rear ellipsoids, and can have different values, provided to respect the condition expressed in equation (1.6).

$$Q = \eta UI \tag{1.5}$$

$$f_f + f_r = 2 \tag{1.6}$$

$$2Q = 2\eta UI = \int_{-\infty}^{+\infty}\int_{-\infty}^{+\infty}\int_{-\infty}^{+\infty} q(x,y,z)dxdydz \tag{1.7}$$

The determination of the heat source semi-axes lengths a_f, a_r, b, and c, is not an easy task, and requires an experimental calibration (temperature measurements or observations of the molten pool area). In the absence of this data, (Goldak et al., 1984) recommend taking the length a_f equal to half the depth c, and a length a_r equal to the penetration depth of the source.

1.3.2.2 Adapted heat source model

The double-ellipsoidal heat source model has been widely used for modeling heat input in welding simulation, and is still relevant in WAAM process simulation. However, in order to use it in the present model, this sophisticated heat source need to be adapted and further developed, for several reasons. First, the amount of heat delivered to the substrate and new deposited elements is conditioned based on their relative position according to the heat source frame of reference. According to (Goldak et al., 1984), the integral of the two power density functions in spacial coordinates is equal to twice the total arc power, as described by equation 1.7. Therefore, in order to deliver the right amount of heat to the part, the heat source origin according to z-axis should be placed on top surface of the current layer (new and previously deposited elements), as illustrated in Figure 1.6.a. In this case, the arc power is mainly transmitted to the elements of the current layer, and no weld penetration into previous layers is considered, which is not what actually occurs in physical reality. On the other hand, by placing the origin of the heat source on top surface of the substrate (previous layer) as in Figure 1.6.b, the transmitted power is doubled, leading to additional heat being introduced in the finite element analysis.

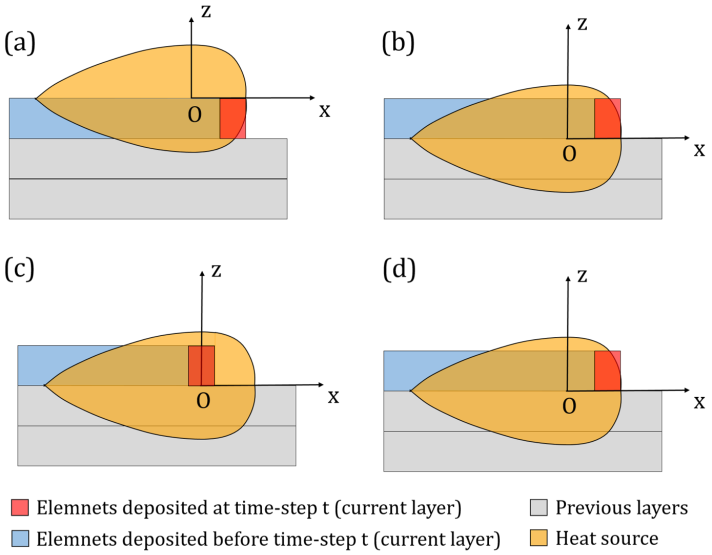

Figure 1.6: Heat source relative positioning

Moreover, the relative position according to x-axis between the heat source origin and the elements of the current layer is also problematic. In fact, such origin should be centered on the new deposited elements, as illustrated in Figure 1.6.c, so that the maximum heat source power is delivered to the elements representing the new deposited droplet, thus allowing to simulate the molten pool correctly. Nevertheless, in this case, part of the power delivered by the upper half of the heat source will be not considered in the analysis. On the contrary, in order to deliver the entire source power to the deposited elements, the origin according to x-axis should be rather shifted rear the new deposited elements, as shown in Figure 1.6.d, but this assumes that the molten pool is located rear the last deposited droplet. Finally, the double-ellipsoid heat source does not allow to take into account the energy distribution between the wire and the substrate. In fact, the arc power is not fully delivered to the substrate directly. According to previous works (Montevecchi et al., 2017) and (Dupont and Marder, 1995), only 50% of the total arc power is delivered to the substrate via direct transfer, while the remaining 50% is used to melt the feed wire. This melting energy is subsequently transmitted to the part through the enthalpy of the deposited droplets.

In order to tackle the aforementioned issues, the Goldak heat source is adapted and combined with the proposed element deposition technique in order to model the heat input in WAAM process, taking into consideration the energy distribution between the wire and the substrate, as illustrated in Figure 1.7. In fact, the direct energy transfer from the arc to the substrate is considered using only the inferior half of the double-ellipsoid Goldak model. The remaining 50% of the total arc power is delivered by means of the deposited elements. These latter are charged with an amount of energy equivalent to the energy delivered by the adapted heat source, and expressed as follows:

$$Q_{source} = Q_{elements} = \frac{\eta U I}{2} \tag{1.8}$$

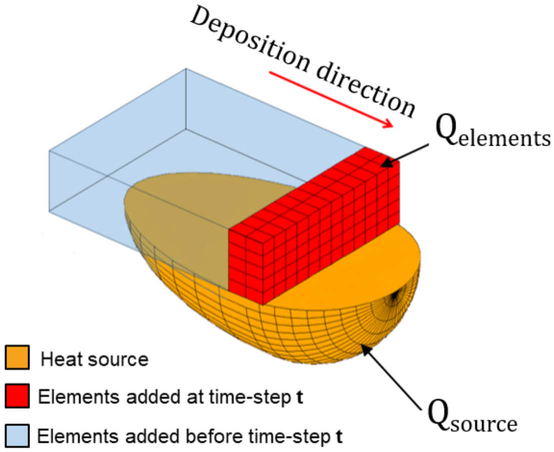

Figure 1.7: Adapted heat source

As expressed in equation 1.8, the total power of the heat source is halved, allowing the heat source to be correctly positioned relative to the z-axis, i.e. on top surface of the previous layer, as illustrated in Figure 1.6.b. This enables to consider the correct penetration of the heat source, without introducing additional heat into the analysis. Furthermore, by replacing the upper half of the heat source with equivalent energy attributed to the deposited elements, it is possible to position the lower half of the heat source correctly, i.e. an x-origin centered on the newly deposited elements, as shown in Figure 1.6.c. This will allow the molten pool to be simulated correctly, while delivering the entire heat source power.

As mentioned in section 1.3.1.2, the energy attributed to the deposited numerical droplet is expressed as a uniform temperature field imposed on the elements representing the deposited droplet. The value of the deposition temperature is calculated as follows:

$$T_d = \frac{\eta U I \triangle t}{2 \rho V C_p} + T_{ini} \tag{1.9}$$

Where T_d is the deposition temperature, Δt is the value of the deposition time-step, V, ρ, are the volume and density of the deposited elements respectively, C_p is the average of the material specific heat capacities of the deposited elements and T_{ini} is the initial temperature of the welding wire. The reason why latent heat is not considered in this formula is explained later in section 1.3.3.2.

This adapted model could be proposed thanks to the element deposition technique, which made it possible not only to properly simulate the wire melting energy transferred to the molten pool by means of the deposited droplets enthalpy, but also to correctly position the heat source origin along z and x axes according to the deposited elements, as these latter become independent. Thus allowing to simulate the molten pool properly.

1.3.3 Boundary conditions and material properties modelling

In the proposed simulation, a model-update procedure is developed in order to implement the element deposition technique properly. This procedure is called after each deposition time-step, and updates the following pre-processing inputs of the finite element analysis :

- Material properties: This step consists on assigning the relevant material properties, such as conductivity, specific heat, and density to the new deposited elements. These material properties are temperature dependent as detailed in sub-section 1.3.3.1.
- Boundary conditions: After the new elements are deposited and the new mesh is updated, the external mesh surface is recalculated in order to prop-

erly apply surface convection and radiation, as detailed further in sub-section 1.3.3.2.

Once these pre-processing inputs are updated, the overall model is considered up-to-date in turn, and FE analysis can start, allowing to properly calculate the temperature field of the next deposition time-step.

1.3.3.1 Material properties

In this manuscript, two aluminum alloys are considered in the different experiments and simulations. Parts are manufactured using an AA5356 (AlMg5Cr) alloy metal wire, deposited on an AA5083 (AlMg4,5Mn0,7) alloy base plate. The chemical composition of both aluminum alloys is presented in Table 1.1. These two aluminum alloys have very similar material properties, and are assumed isotropic and temperature dependent. Nevertheless, in the absence of technical data in literature regarding the temperature dependent material properties of 5356 alloy, and due to the similarities between the two alloys, the evolution of AA5083 conductivity, specific heat and density as functions of temperature is considered for both base and filler metals. Their values were obtained from (El-Sayed et al., 2018), and are presented in Table 1.2.

	Element									
	Cu	Cr	Fr	Mg	Mn	Si	Ti	Zn	Other	Al
AA5083	0.1	0.05-0.25	0.4	4.0-4.9	0.4-1.0	0.4	0.15	0.25	0.15	Balanced
AA5356	0.1	0.05-0.2	0.4	4.5-5.5	0.05-0.2	0.25	0.06-0.2	0.1	0.15	Balanced

Table 1.1: Chemical composition (%) of the base plate and filler alloys

Temperature (°C)	25	80	180	280	380	480	580
Conductivity (W/m °C)	120	122.7	131.6	142.3	152.5	159.5	177.2
Specific heat (J/Kg °C)	924.1	984.2	1039.6	1081.2	1137.6	1178.2	1261.4
Density (Kg/m3)	2673.9	2642.7	2629.4	2611.5	2589.3	2567	2549

Table 1.2: Temperature-dependent material properties of aluminum alloy 5083

1.3.3.2 Latent heat modeling

During the deposition process, the deposited material undergoes multiple heating and cooling cycles that results in a local change of state from solid to liquid during melting and from liquid to solid during solidification. Unlike unalloyed aluminum that change state at a constant temperature (660°C), the aluminum alloy considered in this study undergoes a phase transformation over a range of temperatures, i.e. between solidus temperature (580°C) and liquidus temperature (632°C), with a latent heat of 380 kJ/Kg. Indeed, during the cooling process of the deposited material (in liquid phase) for instance, the heat loss leads to a strong decrease in temperature until reaching liquidus temperature (the lowest temperature at which the alloy is completely liquid). From this point, the temperature decreases very slightly until the heat loss equals the latent heat of the material. At this point, the material temperature reaches solidus (the highest temperature at which the alloy is completely solid), from which it starts to decrease sharply again with the heat loss.

Today, phase change simulation using existing FE modelling techniques seems to be a weighty task. Indeed, taking into account the latent heat during the finite element analysis of an entire deposition strategy presents many problems in terms of simulation convergence and computational time. In fact, two phase change modelling techniques were tested in this study, namely: the heat counting method proposed by Cast3M, and the specific heat artificial variation technique (often used to model the phase change in welding and AM simulation). These two techniques were not able to ensure the convergence of the simulation with “Cast3M 2018”, even when using extremely short calculation time-steps. For this reason, an alternative method is proposed in this section in order to take into account the phase change differently. The basic idea of this method is not to model the phase change during the finite element calculation, but rather to readjust the obtained temperature maps according to the latent heat, as illustrated in Figure 1.8. This method is carried out in two steps:

- Calculation of the temperature fields: the deposition strategy is simulated entirely using the finite element simulation without taking into account the latent heat, and the temperature fields of all time steps are stored successively.

- Readjustment of the temperature fields: the previously calculated temperature fields are processed in a second step by a C++ code. This code allows to browse the calculated temperature fields, and to readjust the temperatures exceeding solidus temperature, at each single node, as a function of latent heat, as shown in figure 1.8.

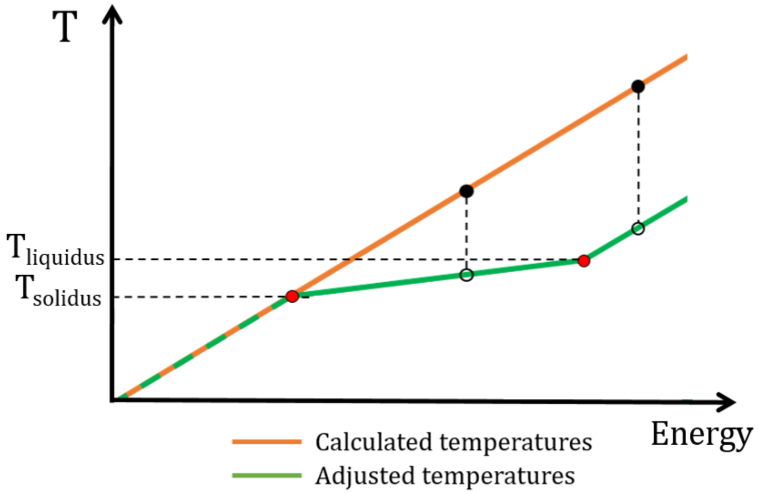

Figure 1.8: Heat capacity evolution

Therefore, the proposed method does not require extremely short time-steps, and a refined mesh around the molten pool in order to ensure the convergence of the simulation. This results in a more stable and a faster simulation. The effectiveness of the proposed method will be tested later on in section 1.5, where it will be compared with other phase change modelling methods.

1.3.3.3 Boundary conditions

As discussed earlier in section 1.1.1, the internal interface between inactive (or quiet) and active elements is difficult to compute, because it changes continuously during the deposition phase. Therefore, surface convection and radiation are often neglected on this interface using inactive and quiet element methods, thus introducing errors to the finite element analysis, especially in the case of large parts simulation, where the size of this interface may be considerably important.

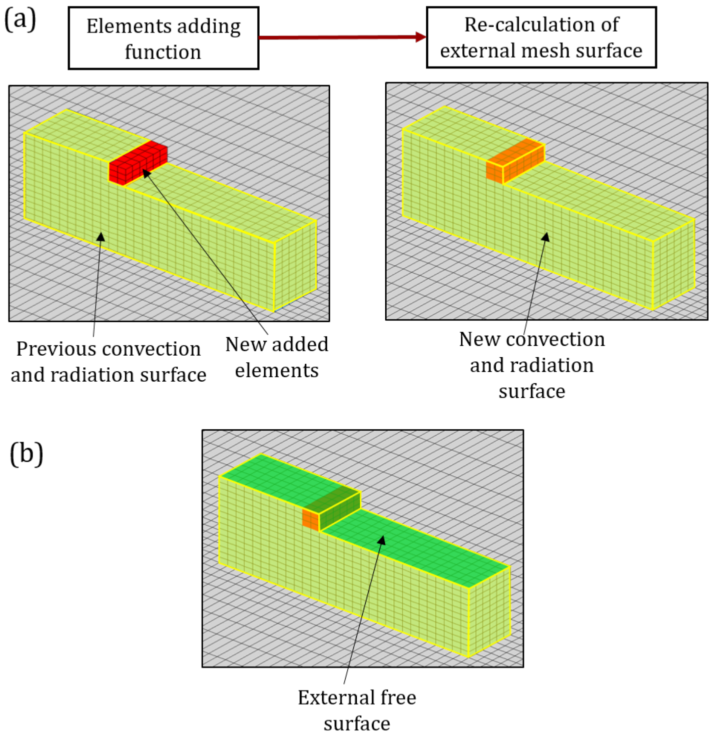

Figure 1.9: External surface recalculation

It is possible to overcome such issue using the proposed element deposition technique. In fact, the overall mesh considered in the FE analysis at a given time-step t is composed only of the elements that are deposited up to this time-step and no inactive or quiet elements are contained in the total mesh. As a result, the internal active/inactive interface becomes an external free surface, as shown in Figure 1.9.b. This allows to apply surface convection and radiation properly regardless of the geometric complexity of the part or the way the mesh evolves. This external mesh surface is continuously adjusted as the mesh representing the deposited regions is gradually constructed during the deposition phase simulation, as illustrated in Figure 1.9.a. This task is carried out by means of the model-update procedure, that allows to compute the external surface of the total mesh, after each deposition time-step, and to update convection and radiation heat loads according the new obtained external mesh surface.

1.4 Model validation

In order to check the effectiveness of the proposed simulation model, an experimental validation is carried out and presented in this section. The accuracy of the model is tested by comparing simulated and experimental temperature curves of a test case obtained. Details of the experimental design and the obtained results are provided in the next sub-sections.

1.4.1 Experimental design

The test case parts are fabricated using a WAAM cell including a Fronuis CMT welding torch mounted on a Yaskawa MA1440 six-axis robot, and a two-axis positioner as shown in Figure 1.10. The materials used in these experiments are a consumable wire electrode (A5356 aluminum alloy) with a diameter of 1.2mm. Layers are deposited on substrate plate (A5083 aluminum alloy) placed on the positioner and maintained fixed during the deposition process. The layers are deposited under 100% Argon gas protection with a flow rate of 13 L/min.

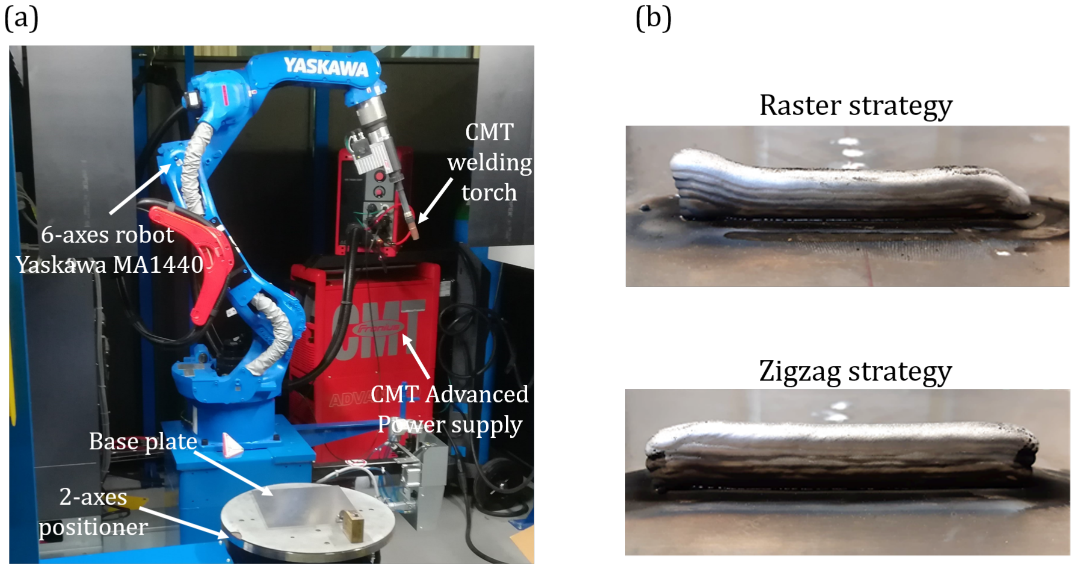

Figure 1.10: Experimental WAAM system

The test case consists of fabricating two thin-wall parts of eight single-pass layers each. The test case parts dimensions are 80 mm in length and 6 mm in width, and the base plate dimensions are 250 mm in length and width, and 5 mm in thickness, as illustrated in Figure 1.11. The thin-wall parts are deposited on two different substrate-plates, and centered in the middle of the plates. Each thin-wall part is fabricated according to a different deposition strategy. The first thin-wall part (Figure 1.10.b) is made according to a “Raster” trajectory, where the layers are deposited only in one direction, as illustrated in Figure 1.11.b. The second thin-wall part (Figure 1.10.b) is fabricated according to a “Zigzag” trajectory, where the layers are deposited in both directions, as illustrated in Figure 1.11.b. Details of both deposition strategies are presented in Table 1.3.

	Deposition trajectory	Welding current (A)	Welding Voltage (V)	Travel speed (mm/s)	Wire feed speed (m/min)	Idle-time (s)
Strategy 1	Raster	12	80	10	5	2
Strategy 2	Zigzag	12	80	10	5	2

Table 1.3: Test-case strategies parameters

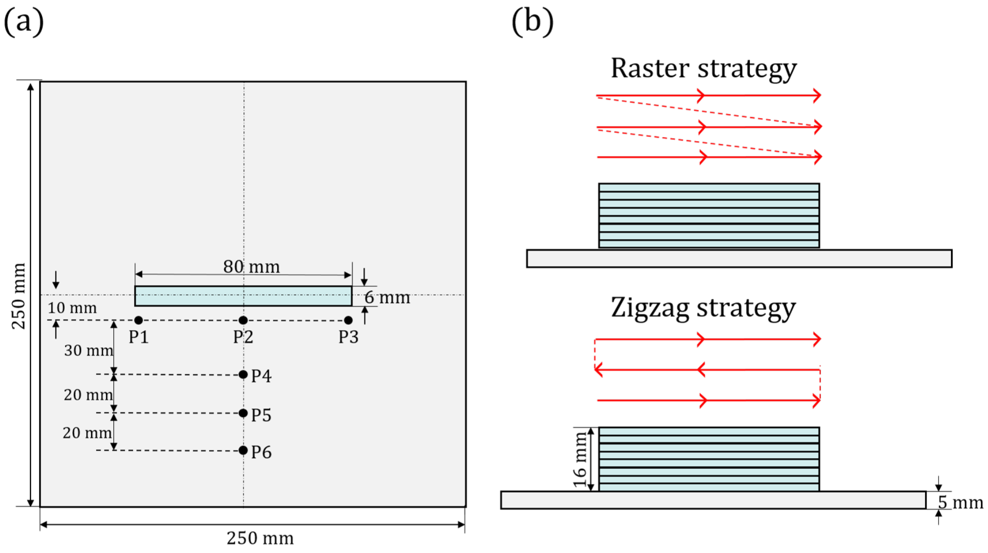

Figure 1.11: Experimental design

During the manufacturing process (deposition and cooling phases), temperatures are measured at six different control points aligned in both x and y direction on the base plate, using six k-type thermocouples. The thermocouples are positioned on the surface of the base-plate at points P1, P2, P3, P4, P5, and P6, as illustrated in Figure 1.11. Temperatures as a function of time are acquired during a 80 seconds deposition phase (corresponding to the eight deposited layers) and an 88 seconds cooling phase. The six K-type thermocouples characteristics are presented in Table 1.4.

Precision (°C)	Measurement range (°C)	Sample rate (Hz)
±2.2	[-200, 1250]	10

Table 1.4: K-type thermocouples characteristics

1.4.2 Test case simulation

The test case parts described in the previous section were simulated using the proposed FE simulation. The overall mesh, including both base plate and deposited elements, contains 57270 8-nodes brick elements, and is shown in Figure 1.12. The adapted heat source semi-axes used in the simulation are calibrated using the macro-scratch patterns of the molten pool as recommended by (Goldak et al., 1984), and their values are presented in Table 1.5.

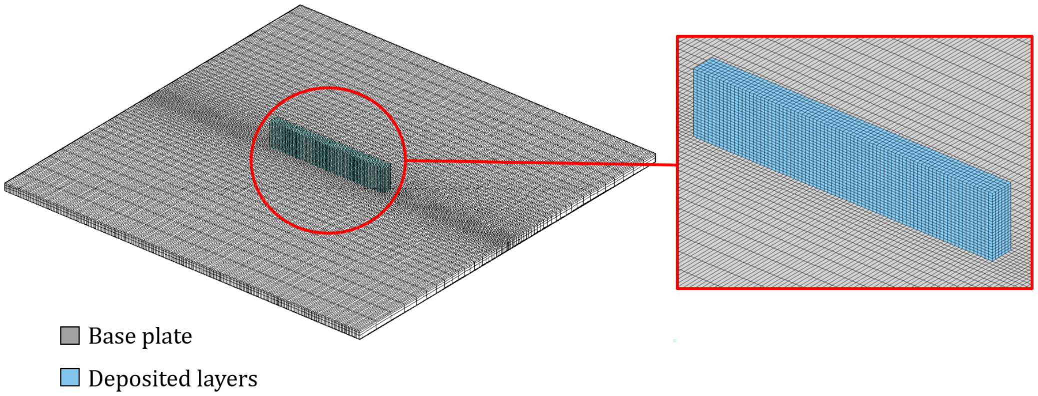

Figure 1.12: FE model of the test case

Parameters	Q (W)	η	a_f (mm)	a_r (mm)	b (mm)	c (mm)
Values	960	0.83	3	6.5	3	3

Table 1.5: Heat source parameters

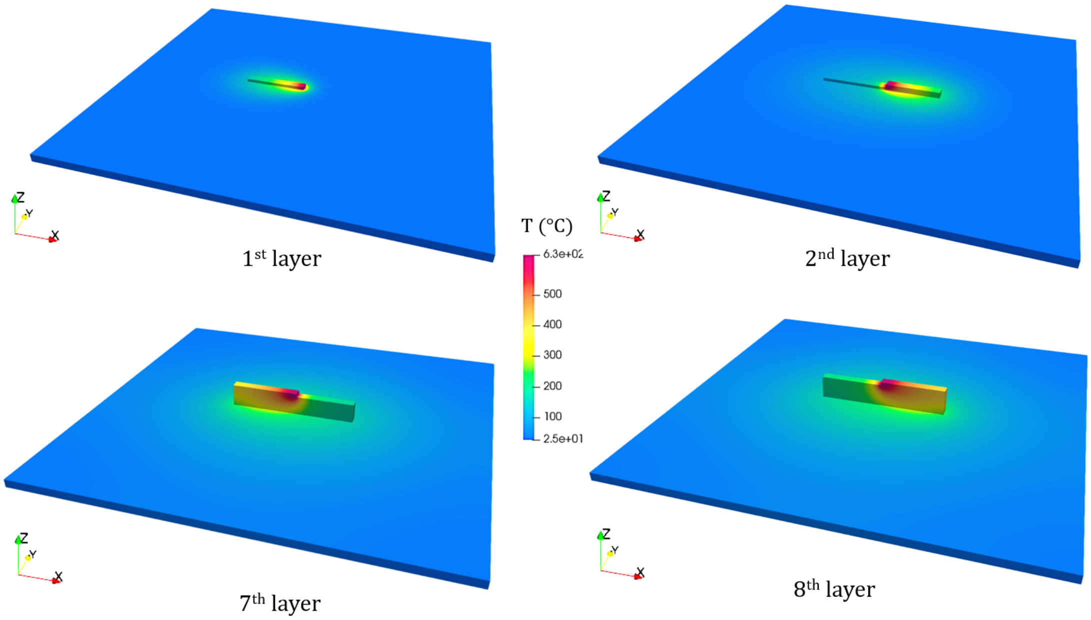

Figure 1.13: Simulated temperature field of Zigzag strategy at different layers (zigzag strategy)

In the simulation post-processing stage, the evolution of the mesh and the corresponding temperature field can be visualized. The simulated temperature fields at the first, second, seventh and the eighth layers are illustrated in Figure 1.13 using the wall fabricated according to zigzag strategy as an example. Also at this stage, the temperature curves as a function of time are extracted from the nodes representing the control points P1, P2, P3, P4, P5, and P6.

1.4.3 Results and discussion

The experimental temperature curves as a function of time are compared to the results obtained with the proposed simulation. Comparisons at control points P1, P2, and P3 (x-axis direction) for both Raster and Zigzag strategies are shown in Figure 1.14.a and Figure 1.14.b, respectively. The dashed lines and continuous lines are the simulated and the experimental temperature curves, respectively.

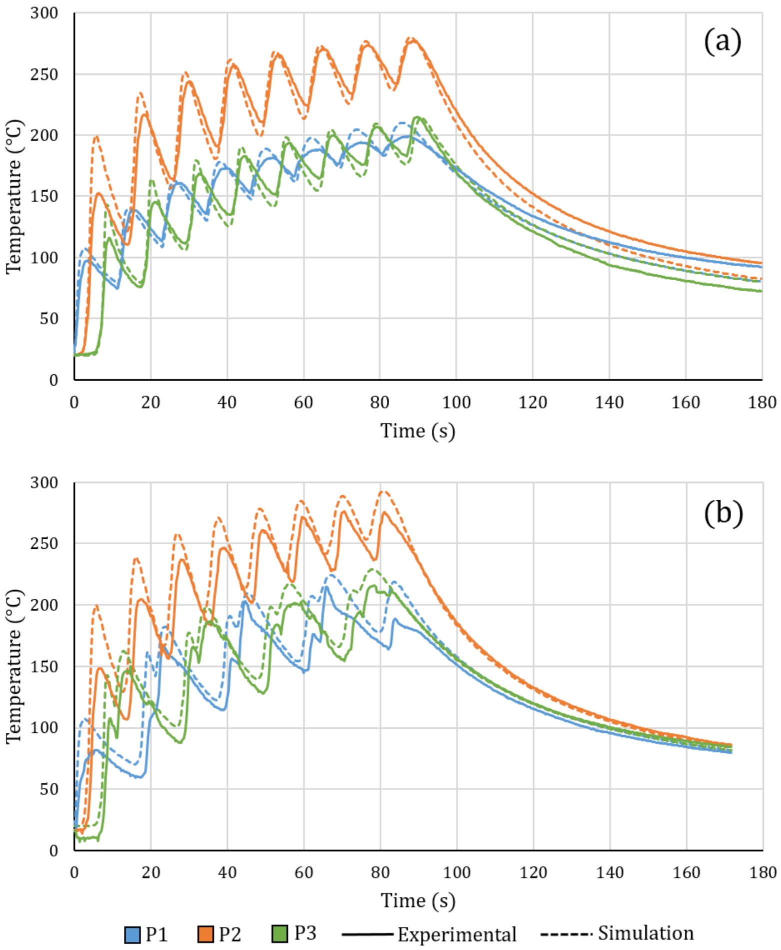

Figure 1.14: Comparison of simulated and experimental temperature curves at P1 P2 and P3 for: Raster strategy (a) and Zigzag strategy (b)

The results shows that the simulated and the experimental temperature curves at control points P1, P2, and P3 are correlated with good agreement between them. It can also be observed that during the deposition phase of the first test case part (Raster strategy), eight peaks can be distinguished on both experimental and numerical curves, as shown in Figure 1.14.a. These peaks represent the eight passages of the heat source near control points P1, P2, and P3, located 5 mm from the deposited layers. In the case of the thin-wall part manufactured according to Zigzag strategy, a set of four peaks composed of two successive vertices each, are recorded on the curves corresponding to control points P1 and P3 instead of eight separate peaks, while the curve corresponding to middle control point P2 remain the same as for Raster strategy (i.e. eight separate peaks), as shown in Figure 1.14.b. This is because in Zigzag strategy, control points P1 and P3 are considered both as the arc striking (start) and extinguishing (end) points, in an alternative way, depending on the deposition direction. In other words, the torch quickly passes and returns to the same end point in order to initiate the deposition of the next layer, leaving little time for cooling, which explains the two successive vertices. This detail was not only measured by thermocouples, but was also obtained by the simulation. Thus, it is possible to assess the accuracy of the results that can be obtained by means of the proposed simulation.

A good agreement is also achieved between the experimental and numerical temperature curves at control points P4, P5, and P6 (y-axis direction) for both strategies, as shown in Figure 1.15.a and Figure 1.15.b. In this direction, it is quite normal not to distinguish the eight temperature peaks on the curves, given the important distance between these control points and the deposited layers. Nevertheless, these correlations provide further validation on the effectiveness of the proposed model, and have allowed a better calibration of the heat exchange coefficients (i.e. convection and radiation coefficients).

The differences that can be noticed between the experimental and the numerical curves are inevitable, and can be due to measuring or numerical errors. The average error between the simulated and experimental values is about 10%. However, the gap is higher in the early peaks. Possible sources of such error could be the thermal inertia of the thermocouples. But overall, these correlations made it possible to demonstrate the reliability and the accuracy of the results obtained by the proposed finite element model.

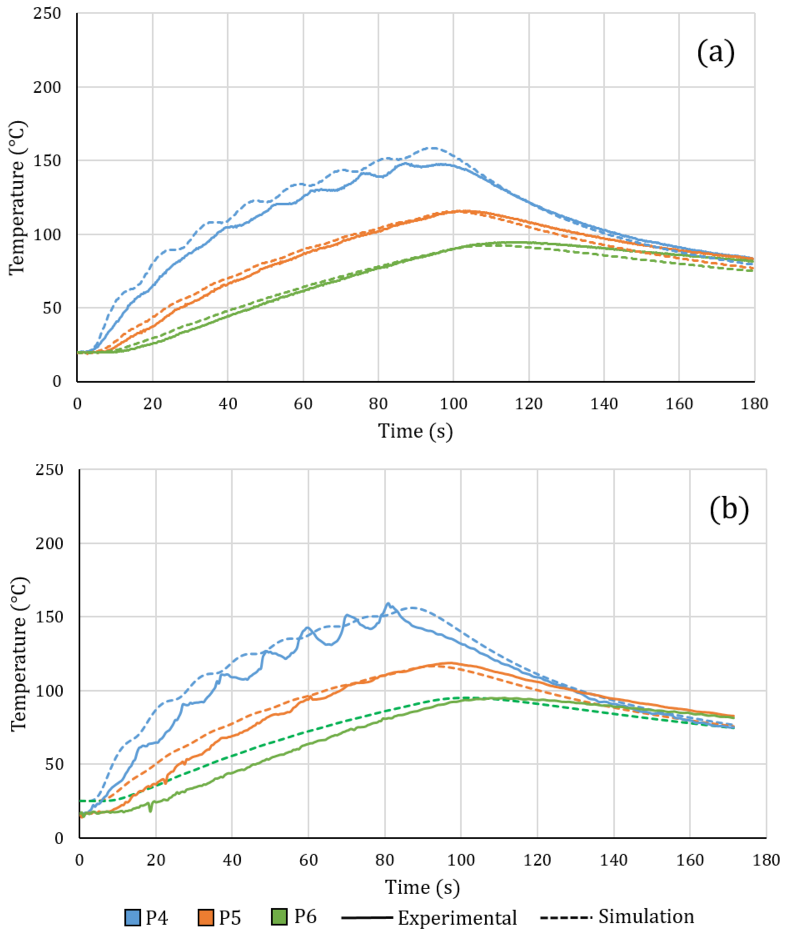

Figure 1.15: Comparison of simulated and experimental temperature curves at P4 P5 and P6 for: Raster strategy (a) and Zigzag strategy (b)

1.5 Computational time and phase change considerations

One major problem in finite element simulation of WAAM process is the high computational costs, which makes it difficult to simulate an entire deposition strategy of a large-scale part in a reasonable time. These high computational time requirements are associated with two simulation aspects:

- The size of the model: simulation of large-scale parts requires a large mesh size. Indeed, a high number of elements is required in the finite element analysis in order to achieve the accuracy desired in the description of the temperature fields.
- The number of simulation time-steps: similarly, simulating an entire deposition strategy requires an important number of simulation time-steps.

These two simulation variables are greatly conditioned by phase change modelling and simulation. Indeed, in order to ensure the convergence and stability of the simulation during phase change, a fairly dense mesh around the molten pool and very short calculation time-steps are required, which will result in an extremely high computational time. In this section, three phase change modelling methods (including the method proposed previously in section 1.3.3.2) will be investigated and compared in terms of results accuracy, simulation convergence, and computational time. The three methods are described in the following.

1.5.1 Considered phase change models

1.5.1.1 Method A: phase change modelling by heat counting

This method is the native method proposed by the finite element code “Cast3M” in order to model the phase change. The input parameters of this method are the melting point (a single phase change temperature), and the latent heat of the material. The method operates as follows:

During heating/cooling of an element, its temperature changes according to its specific heat capacity, until it reaches the phase change temperature. At this point, the temperature of the element is kept constant and the heat losses/gains of the element are accounted for. When these are equal to the latent heat, the temperature is "released" and resumes its evolution according to its specific heat.

This method is quite easy to implement as it is already integrated into the FE code Cast3M. However, the phase change simulation is performed at a constant temperature, assuming that solidus and liquidus temperatures are equal. This is true for unalloyed metals but not for the considered aluminum alloy (a difference of 52°C exists between solidus and liquidus temperatures).

It should be noted that the convergence of this method is a difficult, if not virtually impossible, task with the 2018 and 2019 versions of Cast3M, particularly with the use of FE material deposition modelling techniques. Nevertheless, this phase change algorithm has been significantly improved in "Cast3M 2020", making it finally possible to simulate phase change with this method.

1.5.1.2 Method B: phase change modelling by specific heat variation

The second method is to artificially increase the specific heat capacity as a function of temperature in the phase change range, in order to manage the real thermal inertia of the material. Thus, the latent heat can be numerically considered as a triangular variation of the specific heat between solidus and liquids temperatures, as illustrated in Figure 1.16, respecting equation (1.11):

$$\int_{T_{solidus}}^{T_{liquidus}} C_p(T)dT = L_f \tag{1.10}$$

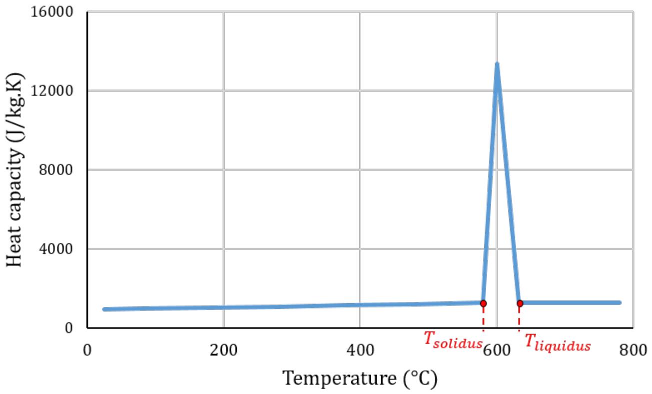

Figure 1.16: Specific heat capacity evolution during phase change for Al5356

This method is the most common in modeling latent heat in welding and WAAM process simulation, and unlike the previous method, the solidus and liquidus temperatures are well taken into account in phase change simulation. Nevertheless, the steep heat capacity triangular gradient requires a refined mesh around the molten pool, as well as an extremely short time-steps in order to ensure the convergence and stability of the simulation.

1.5.1.3 Method C: phase change modelling by readjusting the temperature fields

The third method is the one proposed in the present finite element model. It consists in not modelling the phase change during the finite element analysis, but rather in readjusting the temperature fields as a function of the latent heat, once the finite element analysis is completed. This method was described more in detail, previously in section 1.3.3.2.

1.5.2 Comparison test-case

In this section, the three phase-change modelling methods described above are implemented in the proposed WAAM simulation model using "Cast3M 2020". The “zigzag” test case part, presented in section 1.4.1, will be used as a comparison test-case. The 8-layers part, illustrated in Figure 1.17, is simulated using the three methods while keeping the same mesh size. Thus, only the calculation time-steps are varied in this study in order to compare the three methods. Table 1.6 provides details on the mesh data used in the simulation.

First, the results of the three methods in terms of convergence and computational time are compared. In a second step, the accuracy of the temperature fields provided by the three methods is evaluated at two levels:

1. By comparing the simulated temperature curves with the experimental curves measured using the three thermocouples positionned on control points P1, P2, and P3, as shown in Figure 1.17.(a).

2. By comparing the simulated temperature curves obtained by the two methods (A & C) more locally over a temperature control line (along the layer), at different times, as shown in Figure 1.17. (b)

Type of elements	Element volume (mm^3)	Numerical droplet volume (mm^3)	Elements per droplet	Elements per layer
8-nodes brick	2/3	1x6x2	18	1440

Table 1.6: Mesh data for deposited regions

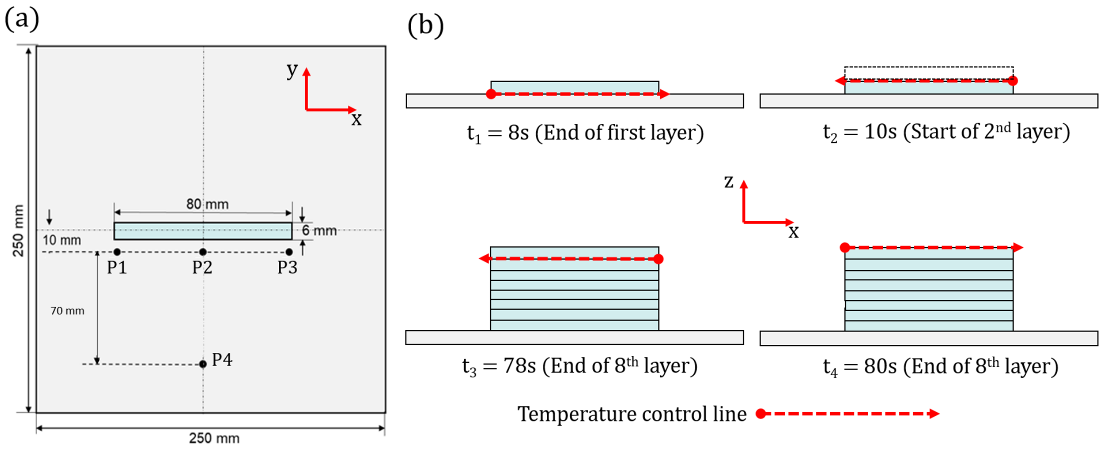

Figure 1.17: Comparison test case part

1.5.3 Results and discussion

1.5.3.1 Convergence and computational time

Table 1.7 presents the number of deposition time-steps possible to simulate using the three methods. While methods A and C allow the deposition strategy to be fully simulated with a fairly coarse time-step, the heat capacity variation method does not allow for convergence. In fact, this method was only able to simulate a few millimeters of the first deposited layer before the crash of the FE computation, even when using a 200 times smaller calculation time-step compared to the other methods.This convergence problem occurs when the droplet is in the process of phase change at the end of the calculation time step, due to the steep heat capacity gradient. As for computational time, the two methods A and C are equivalent, with a simulation time of 3h20min for the entire deposition strategy simulation.

Method	A	B				C
Time-step duration (s)	0.1	0.1	0.01	0.001	0.0005	0.1
Number of simulated time-steps (s)	172 (Total)	10.9	0	9	3.7	172
Computational time for full simulation (min)	201	No convergence				198

Table 1.7: Convergence and computational time of the three methods using Cast3M 2020

1.5.3.2 Results accuracy

Comparison between simulated and experimental temperature curves

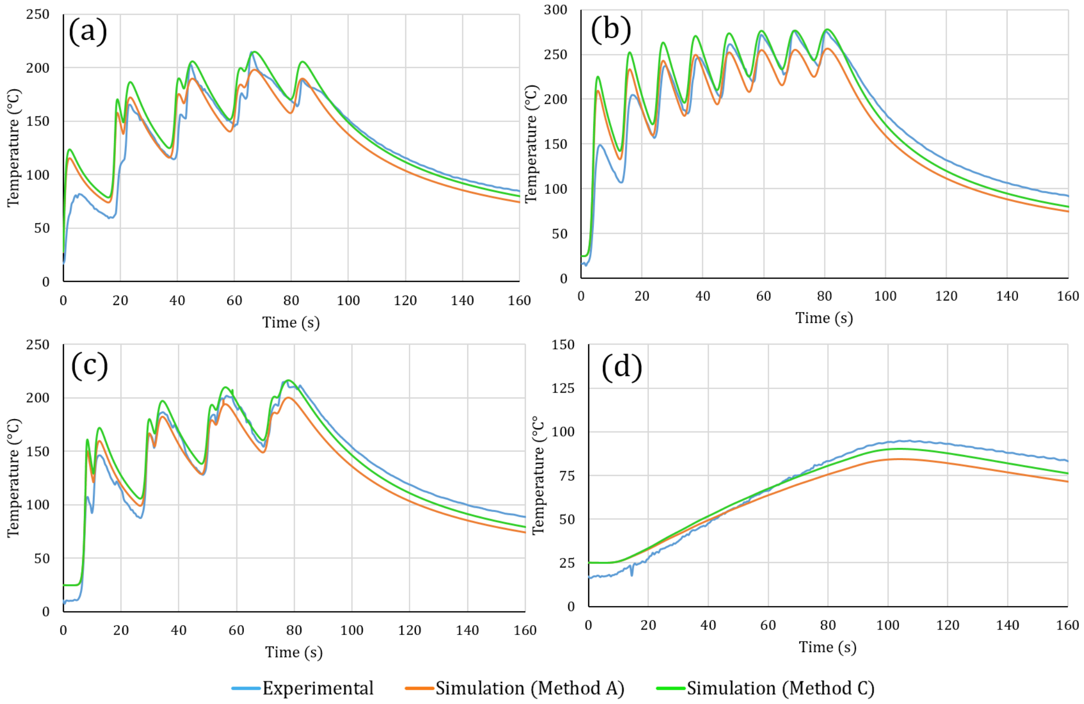

Figure 1.18: Comparison of simulated (Method A & C) and experimental temperature curves at: (a) P1; (b) P2; (c) P3; and (d) P4

The simulated temperature curves as a function of time are compared to the experimental curves measured using the four thermocouples at control points P1, P2, P3, P4, as shown in Figure 1.18. The results shows that the trends of the simulated temperature curves obtained with the two phase change modelling methods correspond well to those measured using thermocouples at the four control points. The mean error between the simulated and experimental curves for each control point, shown in Table 1.8, indicates a slight advantage of method C over method A. But overall, the two phase change modelling methods remain equivalent in temperature prediction when the control point is located far from the molten pool.

	P1	P2	P3	P4
Mean error of method A (%)	12.7	12.2	11.5	10.87
Mean error of method C (%)	11.8	9.8	8.7	7.4

Table 1.8: Comparison of the mean error between the simulated temperature curves (methods A and B) and the measured temperature curves.

Comparison between simulated temperature curves over control lines

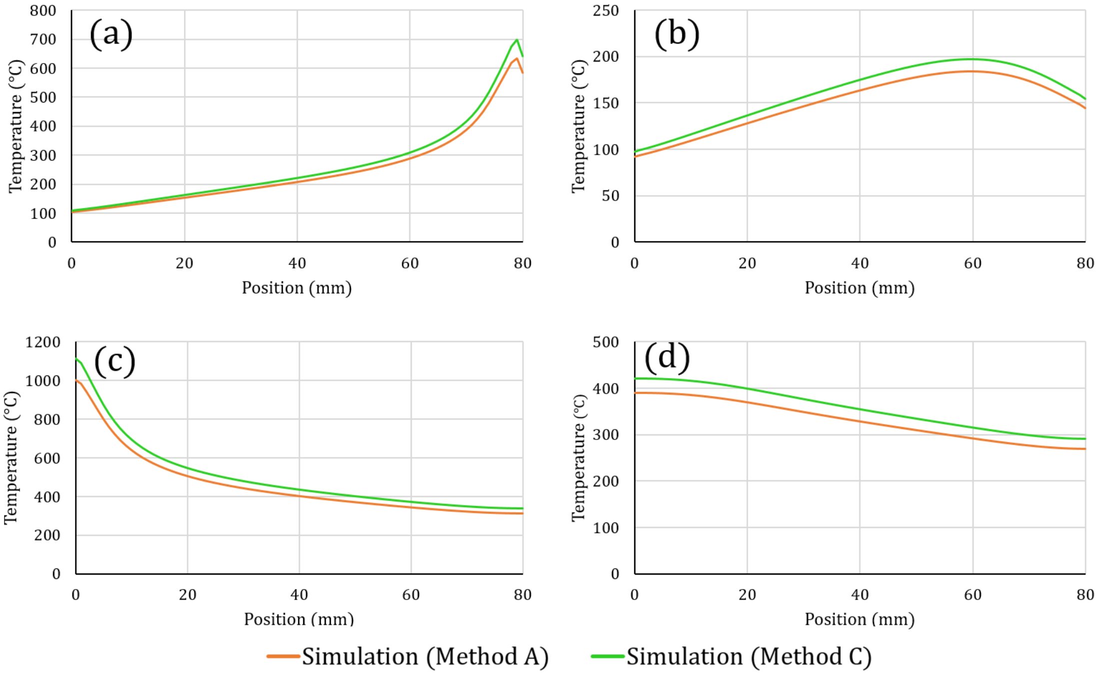

Figure 1.19: Comparison of simulated temperature curves (Method A & C) over control lines at: (a) t_1; (b) t_2; (c) t_3; and (d) t_4

The simulated temperature curves over control lines (as a function of position) at times: $t_1 = 8s$, $t_2 = 10s$, $t_3 = 78s$, and $t_4 = 80s$ are plot in Figure 1.19, allowing a more local comparison of the two phase change modelling techniques. As shown in the figure, the temperature curves simulated by methods A and B show the same trend at all four moments of the deposition phase. Indeed, the simulated curves are nearly identical, nevertheless, a gap is present between the two temperature curves. This difference is very small but becomes more important near the molten pool. A maximum error of 9% is recorded at the points closest to the molten pool (at the end of the deposition of the first and eighth layers), which respectively corresponds to a deviation of 60°C and 100°C, as can be seen in figures 1.19.a and 1.19.c. The mean error between the two temperature curves is presented in Table 1.9. Possible sources of such local deviation is the non consideration of the temperature difference between solidus and liquidus when simulating the phase change using method A.

	t_1	t_2	t_3	t_4
Temperature mean error (°C)	18.2	10.5	38.8	10.87
Mean error (%)	6.7	6.5	7.8	7.4

Table 1.9: Comparison of the mean error between the simulated temperature curves (methods A and B)

1.5.4 Conclusion

In this section, three phase change modeling technique were compared in terms of simulation convergence, computational time, and results accuracy. The specific heat variation method showed difficulties in simulation convergence and stability, while the heat counting technique was able to converge with the 2020 version of Cast3M. Like the temperatures readjustment method proposed in this chapter, the heat counting technique allowed the simulation of the entire deposition strategy within a reasonable time. The results show that the two methods are equivalent in terms of computational time and results accuracy.

In the remainder of this manuscript, all simulations are carried out using the proposed temperature readjustment. For future work, the use of the method proposed by Cast3M is rather recommended, given its ease of implementation.

1.6 Conclusion

In this chapter, a thermal finite element model is proposed for WAAM process based on a new metal deposition technique. This element deposition technique enables, for each deposition time-step, to add new elements to the previous mesh, following the passage of an adapted heat source. Thus, allowing to model both material and heat input, and to better consider heat exchange in the external surfaces. In addition, an alternative technique was proposed in order to take into account the phase change differently. This creative method was proposed to overcome temporary shortcomings in the existing FE phase change algorithms. Finally, the proposed modeling techniques were validated through an experimental test case, where simulated results are shown to be in agreement with the experimental curves.

Thanks to the proposed FE modeling techniques, it is possible to simulate the thermal history of an entire WAAM deposition strategy with sufficient precision, and within a reasonable time. The proposed FE simulation is therefore a fast and valid tool, which will be used in what follows for:

- The development of a set of thermal quality criteria, allowing for the evaluation of the quality of WAAM fabricated parts, and thus their deposition strategies.
- To optimize WAAM deposition strategies and improve the quality of the fabricated parts by integrating optimization algorithms into the simulation.

Chapter 2

Thermal quality criteria

2.1 Introduction

As seen in the previous chapters, the thermal behavior of WAAM process has a significant influence on the final quality of the deposited parts. The constantly changing thermal deposition conditions, such as heat dissipation conditions, and the non-uniform temperature field experienced by the part during the deposition process make it difficult to control and ensure a constant part quality. A quality that can vary drastically depending on the deposition strategy chosen, as the latter dictates the part's thermal history during the manufacturing process.

In order to gain more insights on the different thermal phenomena affecting the quality of parts, a macro-scale thermal simulation was developed in the previous chapter, enabling to predict and study the thermal behavior of WAAM process. The proposed finite element model allows to simulate an entire deposition strategy for a given part, and provides the corresponding temperature maps with sufficient precision and within a reasonable time. Also, recall that the thermal simulation was developped for optimization purposes, i.e. it will be further used to optimize WAAM process, and produce good quality parts by optimizing deposition strategies. But to achieve such objective, the different quality problems affecting WAAM deposited parts must be identified, and the thermal phenomena at the origin of these defects must be investigated. Indeed, this optimization can only be achieved if the quality defects are known, and the causes behind their appearance, especially thermal, are understood and can be controlled. It is for this reason that this chapter will be dedicated to study the defects affecting the quality of WAAM produced parts, using the previously developed simulation. In the following, the main defects affecting part's quality, as well as their causes are characterized. On the basis of this characterization, a set of thermal quality criteria are proposed. The latter enables to track the thermal phenomena at the origin of these defects, and therefore to predict their appearance. These thermal criteria are calculated based on the thermal history of the part as provided by the simulation, and must meet the following specifications:

- Only thermal quality criteria: the criteria only detect thermal-caused defects, i.e. defects that appear due to a thermal phenomenon.

- A failure/success quality criteria: the function of the criteria is to predict the appearance or not of the defects, and even if they allow to give an order of magnitude, or to follow the evolution of a given defect, they will not be used to accurately quantify the defect.

- Flexibility: the criteria must be able to be calculated using the previously developed simulation, as the finite element analysis progresses (between calculation time steps), or after its completion. This will allow these criteria to be integrated internally into the simulation, and later used in deposition strategy optimization algorithms.

- Robustness: the criteria must be independent, as much as possible, of the simulation parameters (duration of the time step, number of DOFs, etc.)

In the following, a bibliographic study summarizes the most common defects encountered in the manufacture of parts using WAAM technology, especially those encountered during the manufacturing of thin-walled structures type of parts. This state of the art made it possible to classify these defects and to establish a first potential link between a defect and its thermal cause. These links will be further verified and explained in depth thanks to the thermal simulation, during the construction of the thermal quality criteria.

2.2 Defects characterization (State of the art)

The quality of WAAM deposited parts can be evaluated from two aspects, namely, the geometric accuracy, and the material integrity.

2.2.1 Geometric defects

2.2.1.1 Dimensional accuracy

This defect can be defined as the variation of the layers dimensions, and therefore of the final part dimensions, according to a given direction. In the case of thin-walled structures, this variation is often encountered in build direction, according to which the width of the deposited thin-wall structures varies considerably. In order to illustrate this defect, a thin-wall part was manufactured using the WAAM cell described in section 1.4.1. The part is composed of sixty successive layers of 100 mm in length, continuously deposited according to a zigzag strategy. The manufactured part is shown in Figure 2.1. where the defect in question may be clearly observed. Indeed, it can be seen that the width of the layers increases as the thin-wall part grows tall, leading to a significant increase in the part's total width along build direction. Several studies have already studied this very common defect in thin-walled structures, and different solutions have been proposed in order to correct it. But the cause behind remains unique, namely, heat accumulation. In fact, during deposition of thin-walled structures, the heat is mainly transmitted from the molten pool to the substrate plate through conduction. As the part grows tall, the heat dissipation to the substrate is slowed down gradually. As a consequence, the molten pool increases, and its solidification is slowed down (Li et al., 2018; Bai et al., 2013). This heat accumulation phenomena can also be observed by one of its major consequences, that is, the progressive increase of the part's average temperature (Montevecchi et al., 2018).

Figure 2.1: Width variation in thin-wall parts

(Wu et al., 2017) studied the effects of heat accumulation on arc characteristics and metal transfer behavior in WAAM of Ti6Al4V. They proposed to quantitatively estimate heat accumulation for each layer of a thin-wall part, using the equation of specific heat. They also showed that the layers geometry vary along build direction due to the changing heat dissipation conditions and increasing interpass temperature, namely, the temperature of the last deposited layer at the start of the next layer deposition. Indeed, this interpass temperature has a significant influence on the geometry of the manufactured parts. (Wu et al., 2017) also showed that the total height of a deposited thin-wall part is reduced by 11.7%, and its width is increased by 12.2% when the interpass temperature passes from 100 ° C to 300 ° C, even though all other process parameters are kept constant.

2.2.1.2 Start/End deposition failures

Another common geometric defect in WAAM deposited parts is the collapse of the start and end portions in thin-wall parts. This defect can also be found in the inner and outer corners in more complex thin-walled structures (Venturini et al., 2016; Diourté et al., 2021). In order to visualize this defect, two 60-layers thin-wall parts were manufactured according to two strategies: Zigzag and Raster. The manufactured parts are presented in Figure 2.2.(a), and Figure 2.2.(b), respectively. It can be seen that the part manufactured according to raster strategy experiences a significant collapse on the final portion of the part. This is because the height in the arc striking portion tend to be higher than that of the arc extinguishing area, and given the one direction deposition trajectory, this difference accumulates with the increasing number of layers. This collapse is less present in the thin-wall part manufactured according to zigzag strategy, but it is rather noticed on both start and end portions of the thin-wall part. This is due to the fact that the height different between the arc striking and extinguishing areas is compensated by the alternation in the deposition direction of the successive layers, which makes this strategy the most adopted and preferable one. Despite this, a significant height difference between the start/end portions and the middle portion of the part can still be observed.

(Xiong et al., 2015, 2016) studied the forming appearances in WAAM process, and more particularly the deposition failures in the arc striking (start) and extinguishing (end) areas of thin-walled parts. They explained that the difference in the total height between the start/end portions and the medium portion of the thin-wall part is due to the bad heat dissipation condition of both ends. Consequently, the fluidity of the molten pool is stronger at both ends, which favors their collapse. (Zhang et al., 2003)also affirm that the layer geometry depends on the substrate temperature on which it was deposited. That is because with a low substrate temperature, the layer geometry tend to be narrow and high. However, if the substrate temperature is high, the deposited droplet will flow randomly. In the same perspective, (Manokruang et al., 2020) studied the effect of substrate temperature on the layers geometry for a constant ratio of wire feed speed to travel speed, i.e for a constant volume of deposited material. They showed that the height and width of a layer are strongly linked, and dependent on the substrate temperature on which it has been deposited. That is, as the temperature of the substrate increases, the height of the layer decreases and its width increases, and vice versa, but their product remains constant. They explain this by the fact that the increase in substrate temperature favors the fluidity of the deposited metal, and thus the flattening of the deposited layer.

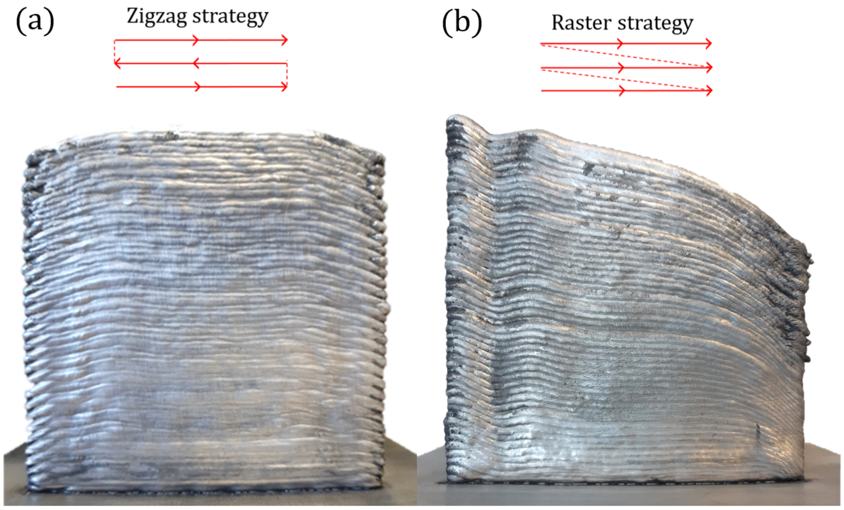

Figure 2.2: Start/End deposition failures in thin-wall parts: (a) Zigzag strategy; (b) Raster strategy

To counter this start/end deposition failures, studies generally recommend to vary the arc voltage and current, as well as the wire feed speed between the start, middle, and the end portions of each single layer(Xiong et al., 2016; Nie et al., 2018). (Zhang et al., 2003) proposed to vary the travel speed between the three portions, and to add another pass at the end portion of each layer in order to rectify the height difference caused by the collapse of this portion. However, these approaches do not allow to keep a constant volume of deposited material. In other words, the variation of wire feed speed to travel speed (WFS/TS) ratio, and the addition of a second deposition pass at the end of each layer causes the variation of the layer's width along the perpendicular to the build direction, even though it may correct its height.

2.2.1.3 Humping

The humping effect is a common defect in WAAM of thin-walled structures. This defect appears in the form of a series of periodic undulations on the deposited layer. These undulations consists of a typical sequence of humps and valleys (Adebayo et al., 2013), as shown in Figure 2.3. This phenomenon occurring at the layer's level accumulates with the increasing number of layers, and can extend to the part scale level, as illustrated in Figure 2.4.

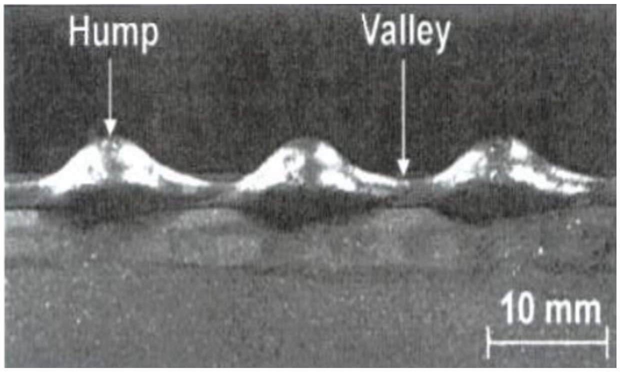

Figure 2.3: Weld bead hump (Adebayo et al., 2013)

Several theories have been put forward on the causes behind the appearance of this defect in welding literature. (Bradstreet, 1968) explains that humped weld is caused by fluid flow patterns and surface tension force during welding. (Xu et al., 2016) proposed a numerical model for bead hump formation in high speed gas metal arc welding, and explained that the strong backward fluid flow is the major factor for bead hump formation. (Yuan et al., 2020) investigated the humping formation mechanisms for multi-directional WAAM, and explained that the strong molten pool metal flow and the premature solidification of the liquid jet are responsible for humping formation. In practice, this defect is often produced following an improper choice of process parameters, including wire feed speed, travel speed, and energy input. Studies carried out to date claim that humping defect may form at increased wire feed speed (Jia et al., 2020), and when travel speed is too high compared to the wire feed speed (Wu et al., 2017; Nie et al., 2018).

Figure 2.4: Humping defect in thin-wall part

2.2.1.4 Distortions

Like in other additive manufacturing processes, WAAM fabricated parts are prone to distortions led by residual stress. These deformations often appear in large-scale thin-walled structures (Colegrove et al., 2013), and can take several forms: longitudinal and transverse shrinkage, bending distortions, angular distortions and rotational distortions (Wu et al., 2018). The cause behind these distortions is the non uniform thermal expansion and contraction experienced by the part during the repeated heating and cooling cycles (Wu et al., 2019).

Different approaches have been proposed in order to reduce distortions leading to imprecise geometry in the final parts. (Ding et al., 2011) proposed a finite element model in order to analyze the thermo-mechanical behavior of WAAM process, and minimize residual stress and distortion in the fabricated parts. (Wu et al., 2019) proposed an active interpass cooling process in order to reduce flexural distortions in WAAM of Ti6Al4V wall structures. (Wu et al., 2019) investigated the effects of WAAM deposition parameters on distortion using a thermomechanical model, while (Hönnige et al., 2018) showed that vertical interpass rolling, and post-deposition side rolling can be effective in controlling and eliminating residual stress and distortions in WAAM of aluminum thin wall-parts.

2.2.2 Material integrity

2.2.2.1 Cracking and delamination

Cracking and delamination are fairly common issues for the additively manufactured parts, including those manufactured by WAAM. The occurrence of these defects depends both on the thermal behaviour of the process, and on the material properties of the deposited metal. Cracking can be categorized into two types depending on the formation mechanism, namely, solidification cracking, and boundary cracking (Sames et al., 2016). The former type of cracking, also known as hot cracking, depend on the solidification nature of the material, and is caused by the high shrinkage strain in the molten pool (Bordreuil and Niel, 2014; Wu et al., 2018). Hot cracking is a famous topic in WAAM of aluminum alloys, and is highly related to the alloys composition (Derekar, 2018), high heat inputs, and re-heating caused by the deposition of subsequent layers (Horgar et al., 2018). Boundary cracking on the other hand, occurs along the grain boundaries of the material. This type of cracking is material-dependent and relies on grain morphology, and the formation or dissolution of precipitate phases (Sames et al., 2016). However, both types of cracking occur on a microscopic scale, and should not be confused with macroscopic cracks that results from other defects, such as porosity.

Delamination is the separation of adjacent layers that occurs due to incomplete melting between layers, or insufficient remelting of the underlying solid. This type of defect is quite visible and cannot be repaired by post-processing treatments (Sames et al., 2016).

2.2.2.2 Porosity

Porosity is another material integrity issue that strongly affects the mechanical properties of WAAM produced parts. This defect can be classified as either raw-material induced, or process induced (Wu et al., 2018).

One reason limiting the use of aluminum alloys as raw materials in WAAM process is the presence of alloying elements responsible for pore formation (Derekar, 2018). (Bai et al., 2017) studied porosity evolution and distribution in additively manufactured aluminium alloys during high temperature exposure, and explained that aluminum alloys are the most susceptible to hydrogen pores formation, since hydrogen is much less soluble in solid aluminum than in liquid aluminum (Lee and Hunt, 2001). Indeed, during the deposition phase, and as the welding torch advances, the molten pool, formed by the liquid portion of substrate metal as well as the last deposited droplets, begins to solidify. At this point, the atomic hydrogen dissolved in the molten pool is rejected from the newly formed solid into the surrounding liquid, due to the important difference in hydrogen solubility between solid and liquid states of the metal (0.036 cm3/100 g against 0.69 cm3/100 g, at a melting point of 660°C) (Bai et al., 2017). Therefore, the solidification process will increase the concentration of hydrogen in the liquid until the solubility limit is exceeded. Consequently, the hydrogen pores begin to nucleate and grow along dendrite grain boundaries (Bai et al., 2017), then float and gather at the top of the molten pool (Hwang et al., 2001). For this reason, porosity is often distributed over the inter-layers fusion line zone. (Bai et al., 2017) also showed that the number of pores highly increases during high temperature exposure, while their average size is slightly increased.

(Cong et al., 2014)studied the effects of the different CMT arc modes on the porosity of additively manufactured aluminum parts. They confirmed that porosity formation in aluminum alloys is mainly due to the mutation of hydrogen solubility during liquid to solid phase change. They also showed that conventional CMT is not adequate for additive manufacturing purposes, due to the large amount and size of gas pores produced by this mode compared to the other advanced modes. In the same perspective, (Fang et al., 2018) investigated pore size distribution and micro-structure evolution regarding the different CMT arc modes in WAAM of 2219 aluminum alloy. They showed that CMT Advanced mode (CMT-ADV) significantly reduced the number of gas pores compared to conventional CMT. Both studies concluded that CMT Pulse-Advanced mode (CMT-PADV) mode is the most suitable for additive manufacturing purposes, since it can further reduce the number and size of gas pores, due to its low heat input.

The differences between these CMT arc modes will be detailed later in section 3.5.1.1.

2.2.2.3 Residual stress

Residual stress is the stress that remains in the material after all external loading stresses are removed. In additive manufacturing in general, and WAAM in particular, residual stress is caused by the large thermal gradients experienced by the part, due to the repeated heating and cooling cycles. A fairly high residual stress has a strong impact on the mechanical properties and fatigue performance of the manufactured parts (Wu et al., 2018).

2.2.2.4 Summary

	Defect	Description	Cause
Geometric defects	Dimensional accuracy	Variation of beads dimensions along build direction	Heat accumulation along build direction and resulting temperature variation
	Start/end deposition failures	Collapse of the start and end portions in thin-wall parts.	Bad heat dissipation conditions at the layers end portions
	Humping	Series of periodic undulations on the deposited layers	Strong molten pool fluid flow & premature solidification
	Distortions	Shrinkage, bending distortions, angular and rotational distortions	Large thermal gradients
Material integrity defects	Cracking & Delamination	Microscopic cracks & separation of adjacent layers	Solidification nature of the material, grain morphology & incomplete inter-layer melting
	Porosity	Formation of gas pores inside the deposited layers	Hydrogen solubility difference between solid and liquid & high temperature exposure
	Residual stress	Stress remaining within the material	Large thermal gradients

Table 2.1: WAAM defects classification

In this section, the most common defects encountered in WAAM of thin-walled structures were characterized, and their potential causes were identified and explained through a literature review. These defects as well as their causes are summarized in Table 2.1. However, the list of defects mentioned above is not exhaustive, and parts manufactured by WAAM are subject to other defects that may affect the quality of the final parts, as well as their performance, such as surface quality or micro-structure evolution.

In the present manuscript, only three defects are investigated. These defects are of solely thermal cause, and remain difficult or even impossible to rectify through post-processing treatments. The considered defects are:

- Dimensional accuracy.
- Start/End deposition failures.
- Porosity.

The thermal phenomena behind these defects will be further investigated using the finite element simulation, and a set of thermal quality criteria reflecting these phenomena will be constructed. The two 60-layers thin-walled parts presented in the introduction of this manuscript will be used as test parts in the study of the three defects and the illustration of the different thermal phenomena at their origin. Details of the test-case parts deposition strategies are reminded in Table 2.2 and Figure 2.5.

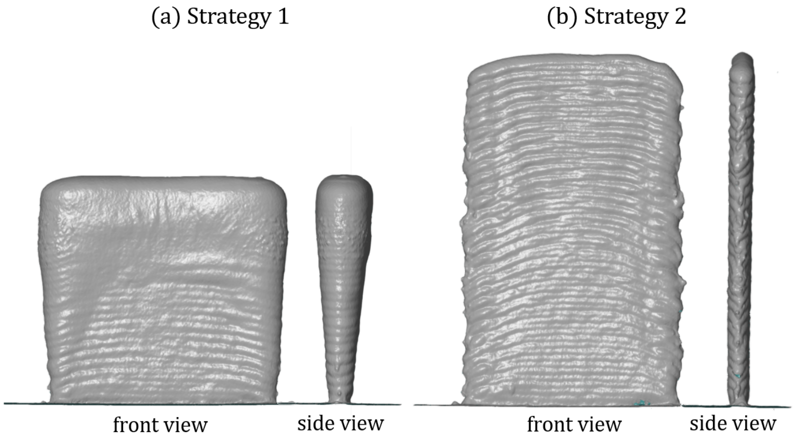

Figure 2.5: Manufactured test-case parts

	Deposition trajectory	Energy input (J/mm)	Travel speed (mm/s)	Wire feed speed (m/min)	Idle-time (s)
Strategy 1	Zigzag	77.8	10	5	2
Strategy 2	Zigzag	77.8	10	5	30

Table 2.2: Test-case parts strategy parameters

In what follows, a first thermal criterion, called substrate temperature (T_{sub}) is proposed in order to demonstrate and further investigate the thermal phenomena, as assumed by the literature, at the origin of the three considered defects. After that, three other thermal quality criteria are proposed in order to predict each defect more accurately, by tracking its direct thermal cause. The proposed thermal criteria are calculated for the two test-case parts based on their respective simulated thermal history, and the results are plotted in the form of a 3D colormap, using the mesh of the two simulated parts as a support. This representation allows a better interpretation of the results and a visual analysis of the different defects. Finally, an experimental validation is conducted by comparing the resulted thermal criteria to the measurements of the different defects present on the two test-case parts . The geometric defects are measured using a 3D scanner, while porosity defects are measured using an x-ray computed tomography.

2.3 Proposed thermal quality criteria

2.3.1 Substrate Temperature (T_{sub})

2.3.1.1 Definition

As explained in the previous section, the substrate temperature is of great importance. This temperature has a direct impact on the geometry of the deposited layers. A relatively cold substrate temperature results in a high and narrow layer. Whereas a high substrate temperature results in a wider and flatter layer. Of course, the geometry of the deposited layers, and the substrate temperature in turn, depend also on other process parameters such as energy input, and the amount of deposited material. But in the case where these two parameters are kept constant, the substrate temperature remains the most influential parameter on the evolution of the layers geometry (Manokruang et al., 2020). In this manuscript, the substrate temperature refers to the temperature on which a layer is deposited. This implies the temperature of the substrate plate if the first layer is being deposited, or the temperature of the previous deposited layer, if the layer in question is a subsequent layer.

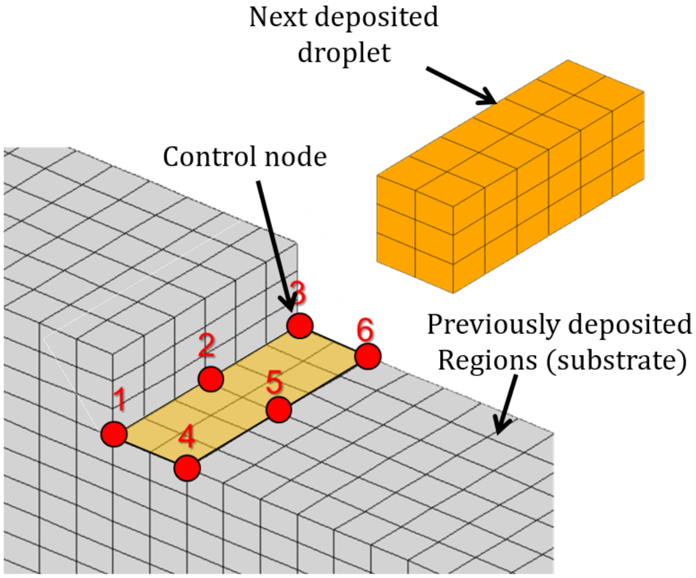

Figure 2.6: Substrate temperature criterion (T_{sub})

The first criterion, also called substrate temperature criterion (T_{sub}), allows to locally track the temperature on which a droplet is deposited. Thus, making it possible to record all substrate temperatures on which each portion of the part has been deposited. As illustrated in Figure 2.6, The calculation of this criterion is based on a number of control nodes, positioned on the top surface of the mesh representing the portion of the substrate on which the next droplet will be deposited, i.e. the fusion interface of the droplet mesh and the substrate mesh. The value of this criterion will therefore be equal to the mean temperature of the control nodes, recorded just before the droplet is deposited, as expressed in the equation (2.1). The positioning of these control nodes changes constantly along the deposit path, and is updated automatically depending on where the next droplet will be deposited.

$$T_{sub} = \frac{1}{n}\sum_{i=1}^{n} T_i \tag{2.1}$$

Substrate temperature control remains the most common means in the study of the thermal phenomena affecting the quality of WAAM manufactured parts. However, most approaches only control the inter-layer substrate temperature. Moreover, the latter is controlled either by measuring it on a single control point, or by considering an average temperature value over the entire layer. Whereas, $\mathrm{T_{sub}}$ criterion enables to track the substrate temperature evolution, with sufficient precision, not only between layers, but also within the same layer. This makes it possible to closely follow the evolution of the deposition conditions in the different portions of the deposited layers, and thus allowing for a better investigation of the thermal behavior of parts manufactured by WAAM. In order to illustrate this, the two test-case parts are simulated using the FE thermal simulation, and the $\mathrm{T_{sub}}$ criterion is simultaneously calculated for both deposition strategies. The results are discussed in the following section.

2.3.1.2 Illustration

Figure 2.7.a allows to visualize the results of substrate temperature criterion, calculated based on the thermal history of both strategies. In strategy 1, the substrate temperature varies considerably in z direction. For the first two layers, the value of the criterion remains low enough (under 450°) due the important heat sink effect, then it highly increases with the increase in the number of layers to reach it's highest value (840°C) on the 60th layer. This important variation in substrate temperature according to build direction is due to the insufficient cooling idle-time (2 seconds), which favors the heat accumulation in this direction. As a result, the successive layers are deposited on a substrate whose temperature increases considerably as the part grows tall, which leads to a significant variation in the layers geometric and metallurgical quality along this direction.

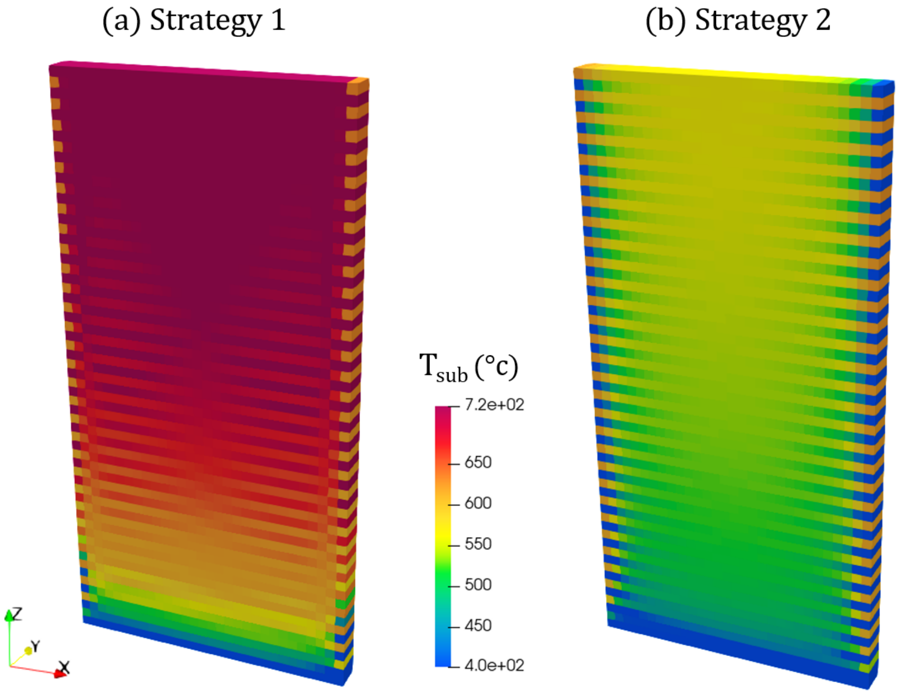

Figure 2.7: Results of substrate temperature criterion (T_{sub}) for: (a) strategy 1 and (b) strategy 2

In strategy 2, the introduction of a larger idle-time (30s) significantly reduced heat accumulation from occurring in build direction. As it can be seen in Figure 2.7.b, the increase in substrate temperature along build direction is considerably slowed down. The value of the criterion remains much cooler, and tends to be more constant in this direction compared to strategy 1. In order to verify this, the average substrate temperature per layer is calculated for both strategies, and plot in Figure 2.8.

T_{sub} evolution along build direction (z-axis)

As it can be seen in figure 2.8, for strategy 1, the average substrate temperature is relatively low in the first layers due to the heat sink effect, but it increases rapidly and reaches solidus temperature (580°C) at the 8th layer. Passed this temperature, the increase in mean substrate temperature continues but with a slower rate due to phase transformation, then reaches liquidus temperature (630°C) at the 16th layer. More specifically, due to the heat accumulation along build direction, only the first eight layers are deposited on a solid substrate. From the 8th layer, droplets are deposited on a substrate that is still on phase change (solid + liquid). Passed the 18th layer, droplets are deposited on a fully liquid substrate, which highly favors rheological deformations. Besides, this change in the substrate temperature along build direction would lead to a significant variation in the layers dimensions, as explained earlier. This can be clearly seen on the manufactured part, which experiences a significant increase in it's total width along build direction.

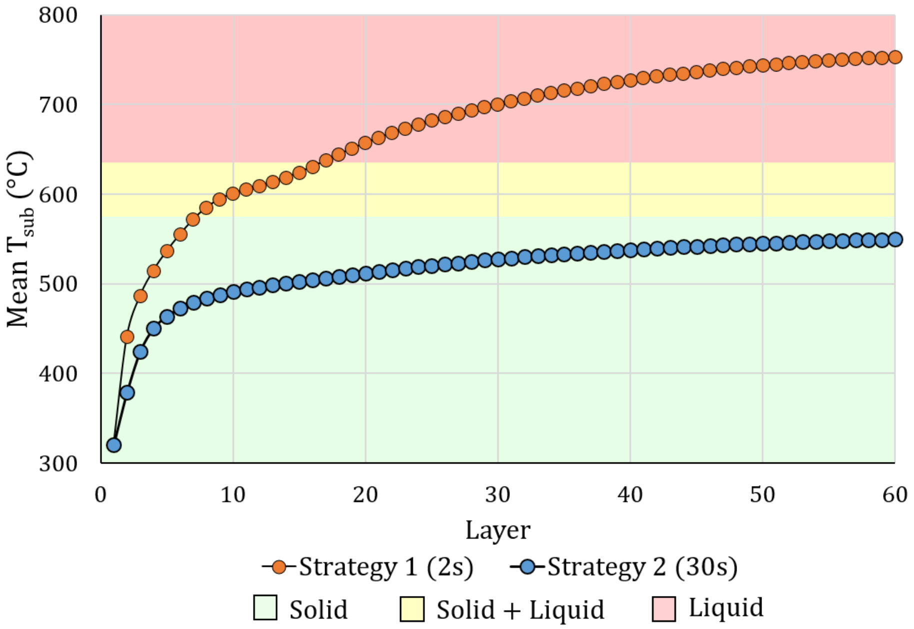

Figure 2.8: Comparison of Mean T_{sub}per layer index for both strategies

As for the thin-walled part manufactured according to strategy 2, the increase in the average substrate temperature per layer remains relatively small. Indeed, the average value of the criterion remains rather low for the first layers due to the heat sink effect, then increases significantly up to the 7th layer. But from this layer on, the increase in Mean T_{sub} continues at a much slower rate, without exceeding solidus temperature (i.e. all layers are deposited on a solid substrate). Simply put, the introduction of longer idle times between layers has allowed to keep a relatively constant deposition conditions compared to strategy 1. This allowed to ensure a more constant layer geometry according to this direction. And thus a thin-walled part with a more constant width, as can be noticed on the manufactured part.

$\mathbf{T_{sub}}$ evolution within the same layer (x-axis)

As explained previously, T_{sub} criterion makes it possible to locally monitor the evolution of temperature deposition conditions within the same layer, i.e. on the different portions of the layer. In order to investigate the start/end deposition failures visible in the thin-wall part fabricated according to strategy 2, the plot of $T_{sub}$of the 40^{th} layer (along x-axis) is shown in Figure 2.9 for both strategies. The latter confirms the explanation given in section 2.2.1.2 regarding this defect. Indeed, in strategy 2, the substrate temperature remains very low in the start portion of the layer (arc striking area) compared to the middle and end (arc extinguishing) portions. This is due to the excellent heat dissipation conditions at the beginning of the layer (lower interpass temperature), enhanced by its natural cooling of 30 seconds. This changes rapidly as the substrate temperature rises and stabilizes throughout the middle portion. However, by reaching the final portion of the layer, the substrate temperature rises considerably and quickly exceeds solidus temperature because of the poor heat dissipation conditions on this portion. This means that the droplets forming the same layer are not deposited on the same substrate temperature between the start, the middle and the end portions of the layer. That implies a tangible variation in the geometry of the layer between these three portions. That is, at the start portion, the layer tends to be narrower and higher, while it is wider and lower at the end portion compared to the middle portion of the layer. Except that, the sharp increase in substrate temperature on the final portion of the layer, as well as its exceeding of liquidus temperature, indicates that the substrate is undergoing a strong overheating in this area, and therefore, one or more previous layers are remelted on this portion of the part. Thus, given the adopted zigzag deposition trajectory, the start portion of the previous layer is remelted at the end of the subsequent layer, which causes both edges to collapse, leading to a height difference between the start/end portions and the middle portion of the thin-wall part. This assumption will be verified in the next section.

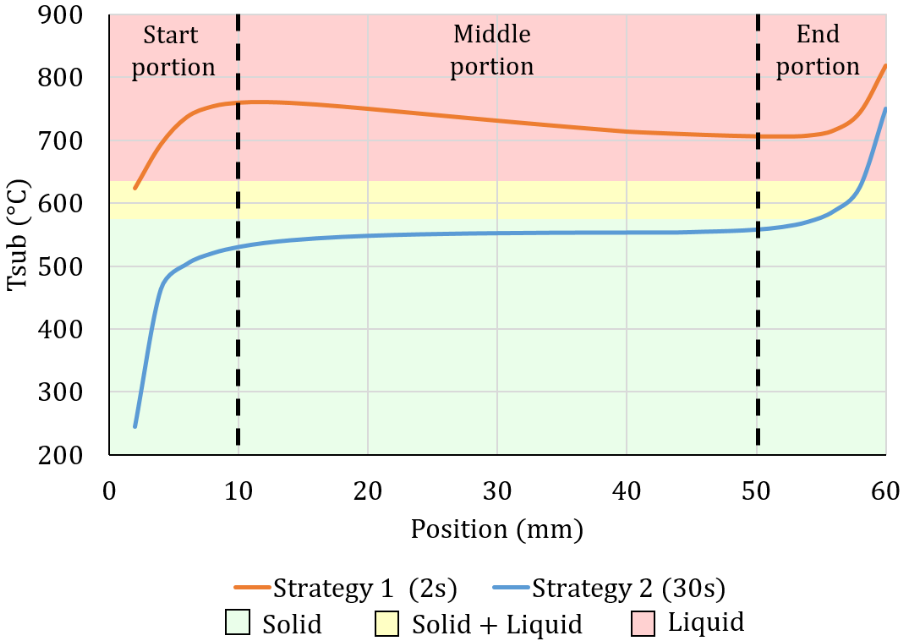

Figure 2.9: Comparison of Tsub distribution over the 40th layer (according to x-axis) for strategy 2

The start/end deposition failures are less visible in the thin-wall part manufactured according to strategy 1. This is because the substrate temperature difference between the start/end portions and the middle portion of the part's layers is not so important as that of strategy 2. In addition, from the 7th layer onwards, the substrate temperature of the layers becomes so high that all portions of the layers are collapsed. This is illustrated in Figure 2.9, which shows that all the three portions of the 40th layer of strategy 2 are deposited on a liquid phase substrate. Indicating a strong remelting of the previous layer along its entire length.

2.3.1.3 Conclusion

The proposed substrate temperature criterion allows to locally follow the temperature deposition conditions in the different layers, with sufficient precision, which provides a first overview on the thermal phenomena affecting the quality of the manufactured part. However, $\mathrm{T_{sub}}$ is calculated instantaneously before each droplet deposition, and does not give more insights on the thermal behavior of the layers after being deposited. In other words, monitoring the substrate temperature allows to get a preliminary idea of the thermal phenomenon that the part undergoes, as well as the defect that is likely to appear. But this is not enough, because the criterion does not allow to visualize the consequences that will take place after droplets deposition. For instance, a significant increase in $\mathrm{T_{sub}}$with the increasing number of layers indicates that heat is accumulating along the build direction, but does not allow to measure the amount of accumulated heat. Similarly, an increase in $\mathrm{T_{sub}}$ on the end portions, or on the inner/outer corners of thin-walled structures, signifies that the heat dissipation conditions worsen on these portions, thus indicating the occurrence of a localized overheating. However, it does not provide more information on the consequences of this overheating on the deposited droplets, nor does it allow a good visualization of the overheated portions. In order to overcome this, three other thermal quality criteria are proposed in the following. Unlike $\mathrm{T_{sub}}$ criterion, the following thermal criteria make it possible to investigate the consequences taking place after droplet deposition, taking into account the deposition of the subsequent layers. Each thermal criteria is designed to track the direct thermal cause of one of the three studied defects, as illustrated in Table 2.3.

	Defect	Thermal cause	Proposed thermal criteria
Geometric accuracy	Dimensional accuracy	Heat accumulation along build direction	Average temperature above solidus (ATAS)
	Start/end deposition failures	Overheating of the layers start/end portions	Maximum temperature (Tmax)
Material integrity	Porosity	Nucleation of hydrogen pores during molten pool solidification	Molten pool volume (MPV)

Table 2.3: Proposed thermal quality criteria in relation to the quality defect and its thermal cause

2.3.2 Maximum Temperature (Tmax)

2.3.2.1 Definition

In order to better capture the overheating phenomena occurring at the start/end portions and inner/outer corners of thin-walled structures, a second thermal quality criterion is proposed. This criterion, called $\mathrm{T}_{\mathrm{max}}$, records the maximum temperature reached by each element of the part during the entire deposition process.

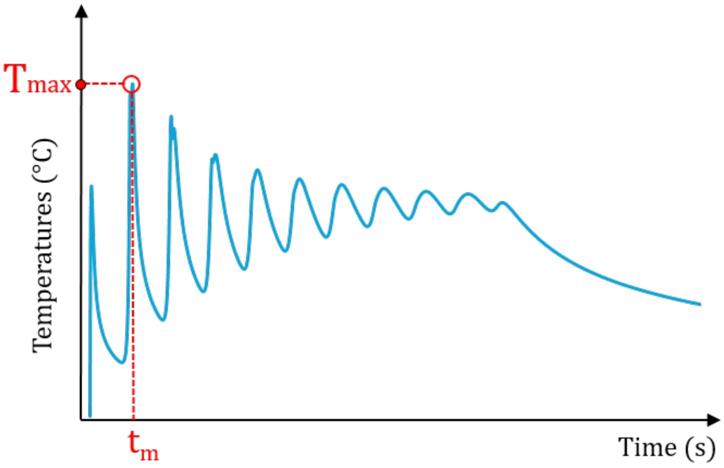

Figure 2.10: Tmax

$$T_{max} = T(t_m); \quad T(t_m) > T(t) \;\; \forall t \tag{2.2}$$

In fact, contrary to what it could be assumed, the highest peak temperature reached by a portion of a deposited layer is not necessarily reached at the moment of its deposition (i.e. when the droplet in liquid state gets to the melting pool), but sometimes later on during the deposition of the subsequent layers, as illustrated in Figure 2.10. Indeed, this portion of the layer can be remelted one or more times if it is located in an overheated zone. Thus, the latter can be subjected to a temperature increase exceeding its peak reached during its proper deposition.

Tmax criterion, expressed in equation 2.2, enables to browse the thermal history of each element of the simulated part, and to search for its maximum temperature reached during the entire manufacturing process (i.e. taking into account the deposition of the subsequent layers). Once the peak temperatures of each element are recorded, these are plotted as a maximum temperature field, based on the total mesh of the simulated part. This provides a 3D visual representation allowing to better spot the portions of the part affected by the overheating phenomena.

2.3.2.2 Validation

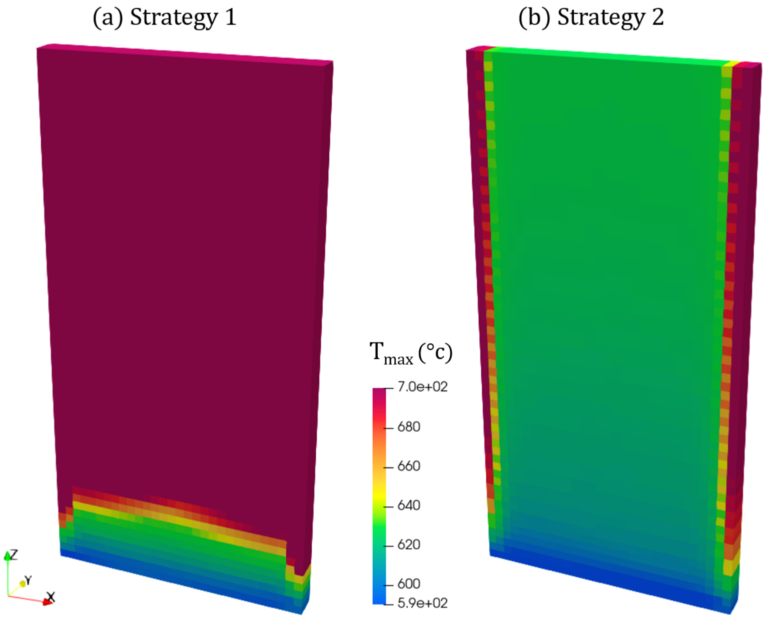

Figure 2.11: Results of T_{max}criterion for: (a) strategy 1 and (b) strategy 2

The results of T_{max} criterion for both strategies can be visualized in Figure 2.11. In strategy 1, the part undergoes a significant overheating on all portions of the layers due to the insufficient cooling idle-times. Indeed, due to heat accumulation according to build direction, the maximum temperature reached by the different portions of the layers exceeds 700°C starting from the 10th layer, as shown in figure 2.11.a. This indicates that all portions of the deposited layers are remelted, leading to an equivalent collapse of the different portions of the layers (along the x-axis). The collapse of the successive layers subsequently results in a significant loss in the part's total height.

The introduction of longer idle times (30s) in strategy 2, allowed to significantly reduce heat accumulation along build direction, which subsequently eliminated the overheating of the large middle portion of the part, as shown in Figure 2.11.b. However, this overheating is still persistent in the start/end portions of layers, which leads to the collapse of both portions. As the part grows tall, this defect accumulates along build direction, and becomes more apparent over the part's total height, as it can be noticed in Figure 2.12.b.

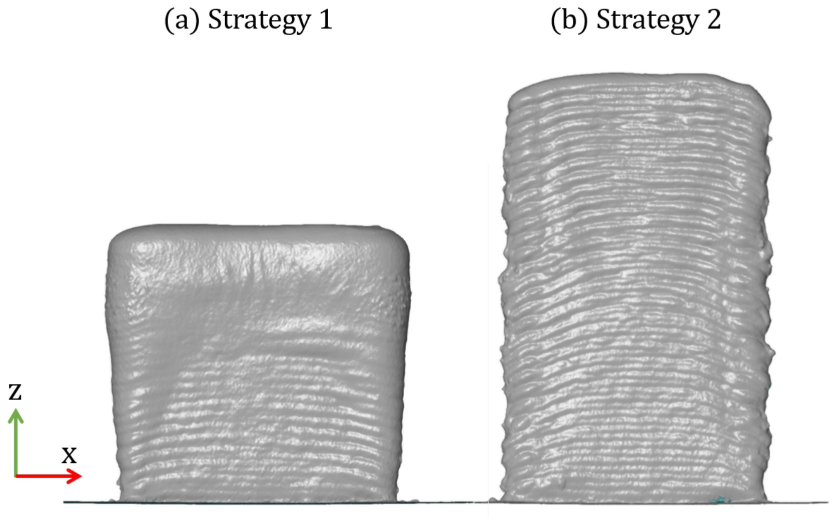

Figure 2.12: 3D scanned test-case parts (front view)

In order to better investigate the start/end deposition failure defect, the evolution of the part's total height along x-axis (xz plane), as well as the average of T_{max} criterion over the 60 layers, are plotted in Figure 2.13. A tangible height difference can be noticed between the start/end portions and the middle portion of the thin-wall part. This height loss of about 8 mm corresponds to an increase in the maximum temperature reached by the two overheated portions of the part. Also, it can be observed that the inflection points of T_{max} curve on the two start/end portions do not coincide exactly with the beginning of these collapsed portions. This is due to the fact that this defect has accumulated with the increasing number of layers, thus causing the two collapsed portions to widen in the top layers of the part.

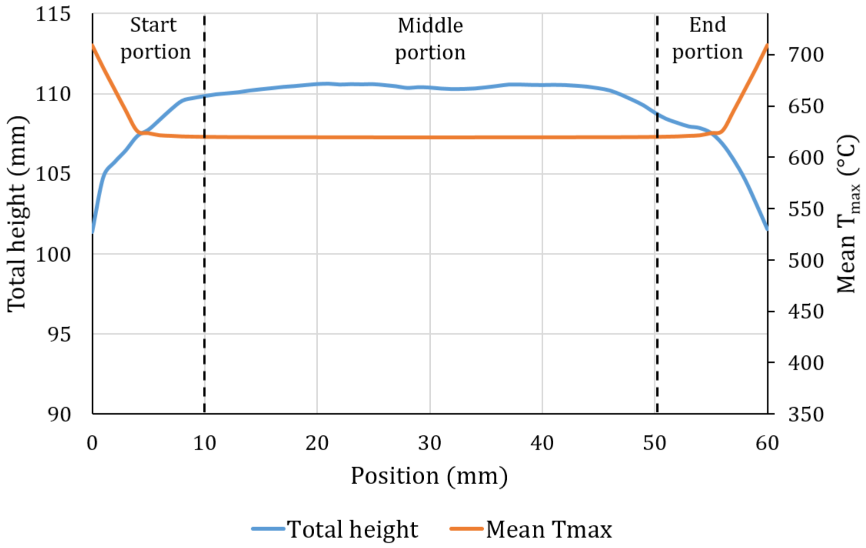

Figure 2.13: Correlation between the part's total height and mean Tmax criterion for strategy 2

2.3.3 Average temperature above solidus (ATAS)

2.3.3.1 Definition

As explained in section 2.2.1.1, heat accumulation along build direction is the main cause behind the geometric quality inconsistencies observed in WAAM of thin-walled structures. This heat accumulation can be observed by a gradual increase in the average temperature of the deposited layers as the part grows tall. This was verified in section 2.3.1, and can be clearly seen in Figure 2.7 and Figure 2.8. The reason behind this phenomena is the worsening of heat dissipation conditions with the increasing number of layers, leading to the variation of layers dimensions, which subsequently results in a significant increase in the part's width along build direction, and a great loss of its total height.

In order to better estimate this heat accumulation phenomena, a third thermal criterion, named average temperature above solidus (ATAS) is proposed. This criterion makes it possible to quantify the amount of heat accumulated by each layer, by calculating the average temperature value of the layers in the non-solid phase, taking into account the deposition of the subsequent layers. As for T_{max} criterion, ATAS criterion is calculated for each numerical droplet, by going through its simulated temperature history, as shown in Figure 2.14. The average temperature above solidus is then calculated based on the resulting temperature curve, as expressed in equation 2.3.

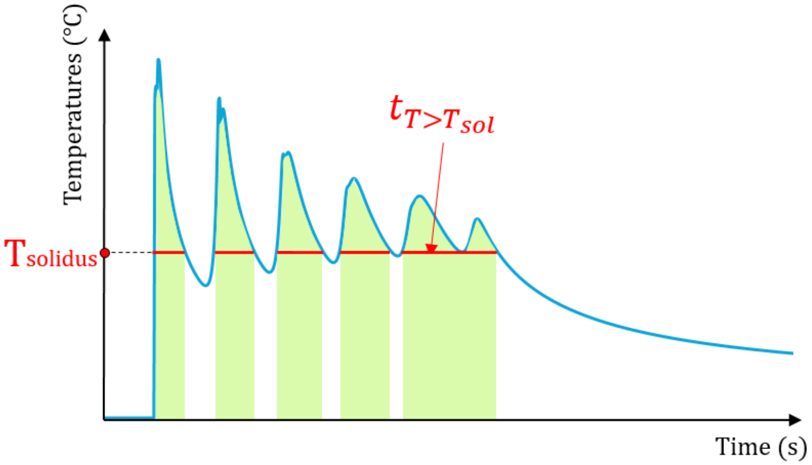

Figure 2.14: ATAS

$$ATAS = \int_{T>T_{solidus}} T(t)dt \;/\; t_{T>T_{solidus}} \tag{2.3}$$

Where T(t) is the temperature of the droplet as a function of time, and $t_{T>T_{solidus}}$is the time interval spent by the droplet above solidus temperature.

This criterion can also be plot based on the part total mesh, allowing to get a better visualization of heat accumulation phenomena experienced by the part, by following the evolution of the layers average temperature in the non-solid phase along build direction.

2.3.3.2 Validation

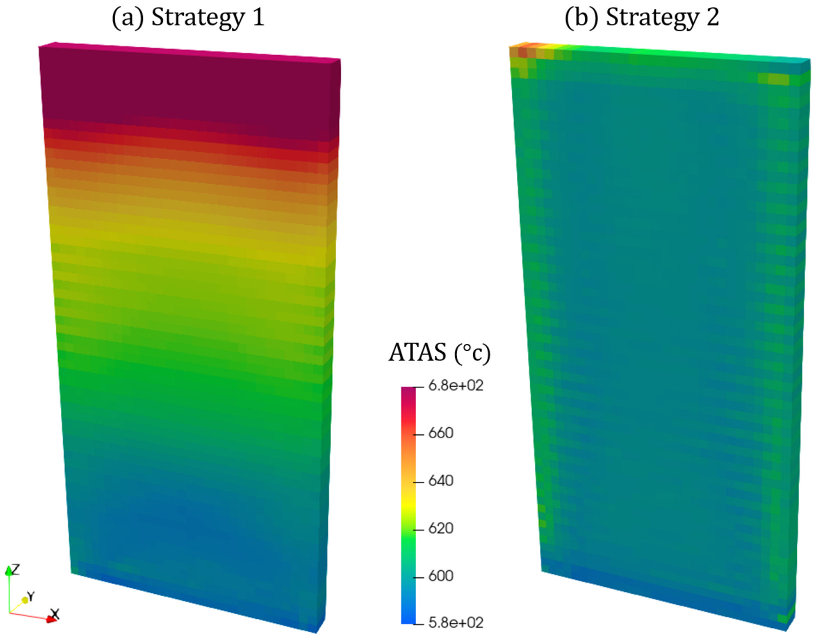

Figure 2.15: Results of average temperature above solidus (ATAS) for: (a) strategy 1 and (b) strategy 2

The results of ATAS criterion for both strategies can be visualized in Figure 2.15. As explained earlier, this criterion allows to better visualize the heat accumulation along build direction. Indeed, the part manufactured with shorter idle-times (2s) experiences a strong heat accumulation with the increasing number of layers, as shown by the corresponding ATAS criterion, plot in Figure 2.15.a. The part's average temperature in the non-solid phase increases continuously with the increasing number of layers, reflecting the heat accumulation phenomena responsible for the variation of layers dimensions along build direction, as shown in Figure 2.16. This heat accumulation was significantly reduced by the introduction of longer idle-times (30s) in strategy 2, as shown in Figure 2.15.b. Indeed, the average temperature of the 60-layers in the non-solid phase remains more or less constant along build direction, which explains the more constant layers geometry according to this direction. As a result, the variation in the part's total width along build direction is largely minimized compared to that of strategy 1, as can be noticed in Figure 2.16.

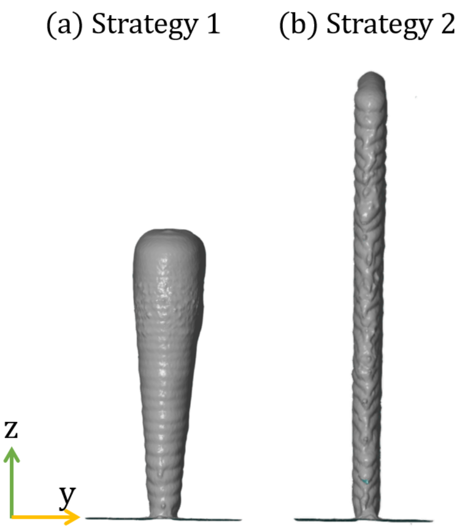

Figure 2.16: 3D scanned test-case parts (side view)

In order to check the effectiveness of ATAS criterion in predicting width variation of thin-walled parts along build direction, the evolution of the ATAS criterion along build direction (according to z-axis) is correlated with the evolution of the part's width along the same direction for both strategies. Width measurements are performed along the middle section of the part based on their 3D scans. This correlation is shown in Figure 2.17, where the continuous lines and the dashed lines represents the evolution of width and ATAS criterion as a function of layer's index, respectively.

Comparisons shows that ATAS criterion and width evolution along z-axis are correlated with good agreement between them for both strategies. Indeed, the evolution of the layers' average temperature in the non-solid phase follows the same trend as the evolution of the layers' width when both curves increase with the increase in the number of layers due to the insufficient cooling idle-times (strategy 1), but also when both correlated curves tend to be constant when introducing larger idle-times (strategy 2). This enables to verify the impact of heat accumulation on the layer's geometry and to prove the ability of this criterion in assessing the dimensional accuracy of the deposited thin-wall parts along build direction.

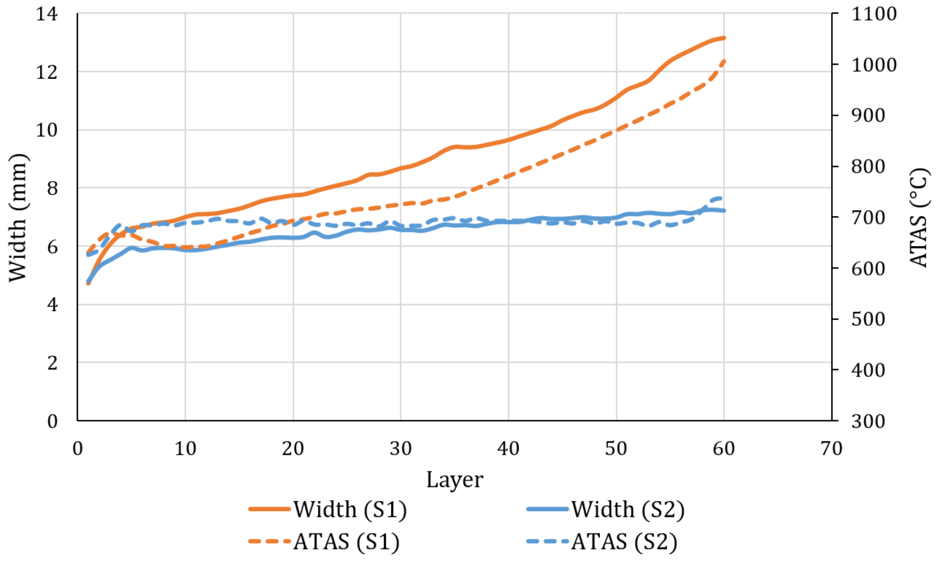

Figure 2.17: Correlation between ATAS criterion and the evolution of the parts total width along build direction

2.3.4 Molten Pool Volume (MPV)

2.3.4.1 Definition

As explained in section 2.2.2.2, the porosity defect often present in parts manufactured by WAAM is formed during the solidification process of the melting pool. The main reason behind this pore formation is the large difference in hydrogen solubility between the liquid and solid phases of the deposited metal. Therefore, the amount of hydrogen dissolved in the liquid phase of the deposited metal is strongly dependent on the volume of the molten pool. In other words, the larger the size of the molten pool, the higher the rate of hydrogen pores nucleating during the solidification process. Based on the present assumption, another thermal criteria is proposed in this section allowing to assess the metallurgical quality of WAAM deposited parts in terms of porosity formation risk and evolution.

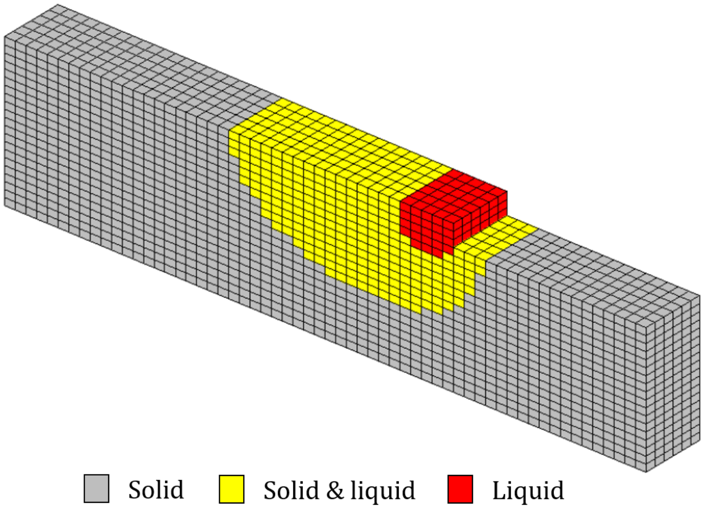

Figure 2.18: Molten pool (solid & liquid + liquid)

As its name indicates, this criterion allow to calculate the volume of the molten pool throughout the deposition process. Based on the temperature maps provided by the FE simulation after each deposition time-step, the volume of elements representing the molten pool (i.e, elements whose temperature exceeds that of solidus) is calculated, as illustrated in Figure 2.18. Thus, the evolution of the molten pool size can be monitored along the entire deposition process. Also, each calculated volume corresponds to a deposition time-step, and therefore to a position in the part total mesh. Thus, these data can be plotted based on the part total mesh, allowing to obtain an overview on the evolution of porosity in the different directions.

2.3.4.2 Validation

In order to investigate the relevance of the proposed molten pool volume criterion, and its capacity to provide an overview on porosity defect evolution in thin-walled structures, the criterion is calculated for both strategies based on their respective simulated thermal histories. Subsequently, the evolution of the molten pool size as a function of layer's index can be obtained at the mid-section of the two simulated parts. On the other hand, the spatial distribution of pores in both fabricated test-case parts were observed through an x-ray micro tomography. These observations

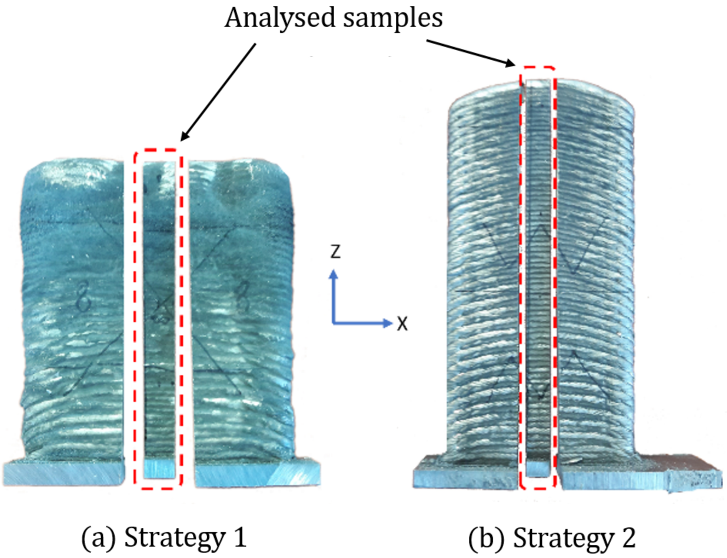

Figure 2.19: Manufactured part and sample definition (Limousin et al., 2020)

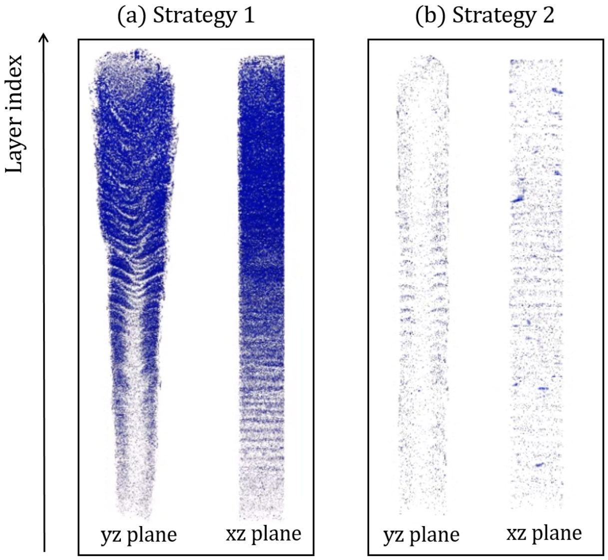

Figure 2.20: Pores spacial distribution of both strategies (represented in blue) (Limousin et al., 2020)

were carried out using two samples taken from the mid-portion of each test-case part (Limousin et al., 2020). The samples are shown in Figure 2.19, and the spacial porosity distribution as a function of layer's index along the mid-section of both deposited parts can be observed in Figure 2.20. Based on these results, the porosity rate evolution as a function of layer's index (i.e. pore volume fraction along build direction) is obtained for both strategies, and subsequently compared to the corresponding molten pool volume evolution along this direction. These comparisons are shown in Figure 2.21.

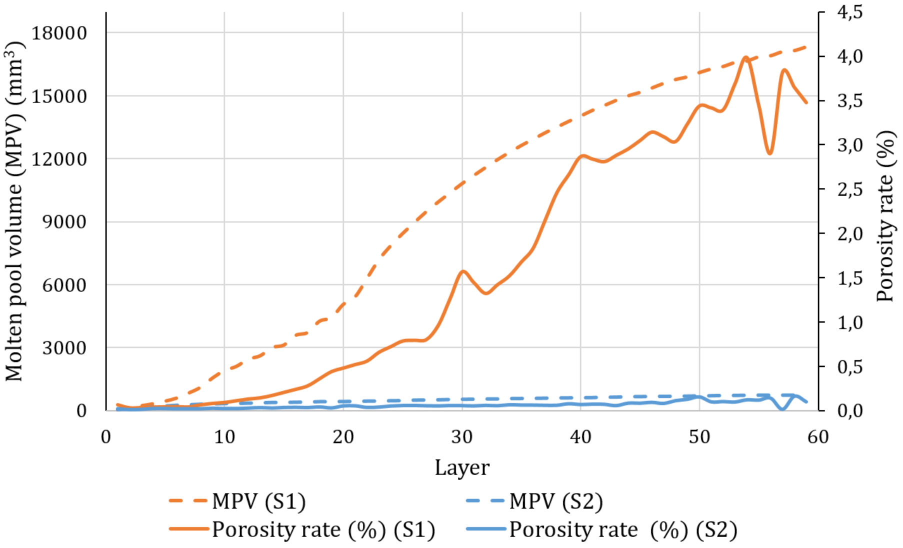

Figure 2.21: Correlations between molten pool volume criterion (MPV) and Porosity rate (%) evolution along build direction for both strategies

The results show a significant increase in the porosity rate along build direction in the part manufactured according to strategy 1 compared to the one manufactured according to strategy 2. Indeed, observations reveal that pores become larger and numerous with the increasing number of layers in strategy 1, but they are much smaller and homogeneous, and their rate remains constant along build direction in strategy 2 (Limousin et al., 2020). The difference in the porosity defect evolution between the two strategies can be explained using the molten criterion volume criterion. As can be seen from Figure 2.21, the molten pool volume evolution is perfectly correlated to the evolution of porosity rate along build direction for both strategies. Indeed, in strategy 1, the molten pool becomes larger as the part grows tall due to short idle-times, indicating that the amount of hydrogen trapped in the layers after solidification is much higher in the upper layers. On the other hand, the introduction of longer idle-times (strategy 2) allowed to keep a small and constant molten pool size along build direction, thus allowing to ensure an equivalent amount of soluble hydrogen in throughout the successive layers. This correlation enables to validate the effectiveness of MPV criterion in assessing the metallurgical integrity of WAAM produced thin-walled parts in terms of porosity.

2.4 Conclusion

In the present chapter, the most common defects encountered in WAAM of thin-walled structures were described and their thermal causes were identified through a literature review. Emphasis has been placed on three major defects, namely: dimensional accuracy, start/end deposition failures, and porosity. In order to gain more insights on the thermal phenomena at the origin of these defects, the substrate temperature criterion (T_{sub}) was proposed at first. The latter allowed to investigate the impact of the different thermal phenomena on the temperature deposition conditions, and to corroborate the conclusions of the literature. Thereafter, three thermal quality criteria were proposed in order to predict each defect more accurately. Each thermal criterion was designed to track the direct thermal cause of one of the three studied defects, namely: heat accumulation, localized overheating and molten pool expansion. Finally, the relevance of these criteria was checked by means of an experimental validation using two test-case parts, where the proposed thermal criteria were correlated with good agreement to the measurements of the different defects.

It should be noted that proposed criteria are not completely independent, due to the dependence of the thermal phenomena at the origin of the different defects. For instance, the heat accumulation at the origin of the variation of layers dimensions along build direction is the main reason behind the increase in the molten pool size, which in turn conditions the porosity rate evolution along this direction. Except that, each thermal criterion tracks the direct thermal cause of a given defect, thus enabling a better prediction of the latter.

Overall, the proposed thermal criteria allow to reach the objectives set previously. In particular, they allow:

- To evaluate off-line a part's quality in terms of geometrical accuracy and material integrity.
- To evaluate the deposition strategy according to which a part was deposited.
- To be integrated into deposition strategy optimization and correction algorithms.

In what follows, the set of proposed thermal quality criteria will be used as:

- Optimization criteria: the substrate temperature criterion (Tsub) will be used as a criterion for optimizing WAAM deposition strategies, since it allows to be calculated instantaneously between simulation time-steps, and because it allows to minimize the three defects simultaneously.
- Quality evaluation criteria: Tmax, ATAS and MPV criteria will be used to evaluate the quality of the parts and therefore the relevance of the chosen deposition strategies, as they allow defects to be predicted more accurately.

Chapter 3

Simulation-based deposition strategy optimization

3.1 Introduction

As shown in previous chapters, the quality of parts manufactured using WAAM can be evaluated from two aspects, the geometric accuracy and the material integrity. It was also shown that these quality aspects are greatly affected by the thermal phenomena occurring during the deposition process such as: heat accumulation, overheating, and changing substrate temperature within the same layer and along build direction. Therefore, the control of the part's thermal history during the manufacturing process is necessary for enabling a consistent and accurate quality in WAAM production. This chapter is therefore dedicated to the optimization of deposition strategies in WAAM process. The objective is to improve the quality of WAAM produced parts by controlling their thermal history using the proposed thermal simulation and quality criteria.

In the following, a literature review is first presented, exploring existing approaches for improving quality of WAAM manufactured parts. Following this state of the art, an adapted simulation-based optimization approach is proposed for optimizing deposition strategies in WAAM process. Based on the proposed approach, two simulation-based strategy optimization techniques are developed, allowing to dictate the desired thermal history in the fabricated parts by adjusting two strategy parameters, namely: the idle-times between layers and the energy input. The different stages of these optimization techniques will be described, and the optimization results will be presented.

3.2 State of the art

Two main approaches are reported in the literature for optimizing WAAM process and improving the quality of the produced parts. The first approach is to control and dictate the thermal history of the parts by adjusting deposition strategy parameters throughout the deposition process. The second approach is to use process add-ons and variants of WAAM to impose the desired thermal behavior to the produced parts. Several techniques have been introduced in literature illustrating the implementation of these two approaches, as detailed in the following.

3.2.1 Deposition strategy optimization approaches in WAAM

3.2.1.1 Real-time strategy optimization approaches

In this category, deposition strategy parameters are adjusted using in-process monitoring devices in a closed loop control system (Rodrigues et al., 2019). Sensors such as thermocouples, infrared cameras, and pyrometers are usually used to monitor the molten pool and the temperature at different regions in the produced parts. A comprehensive review on real-time process monitoring and control to increase part quality in different metal additive manufacturing processes was provided by (Tapia and Elwany, 2014). (Xu et al., 2018) reviewed process monitoring and control methods that have been used in WAAM, and proposed an *in-situ* multi-sensor system model for monitoring WAAM process, as shown in Figure 3.1. (Yang et al., 2017) used an infrared camera to investigate the thermal behavior in WAAM. They found that the prolongation of interlayer idle-time increased the temperature gradient in the deposition process and helped improve the final forming quality of the thin-wall parts. In the same perspective, (da Silva et al., 2020) studied the potential of IR pyrometry for monitoring interpass temperature in WAAM, and showed that IR pyrometry can be considered as a feasible technique to ensure a constant interpass temperature and schedule idle times between layers. (Xiong et al., 2016) proposed a self-adjusting controller for layer width in WAAM of thin-walled parts. They used a visual-sensing system in a closed-loop control system in which the travel speed is adjusted along the deposition path, with the objective of keeping the layer's width within an optimal range.

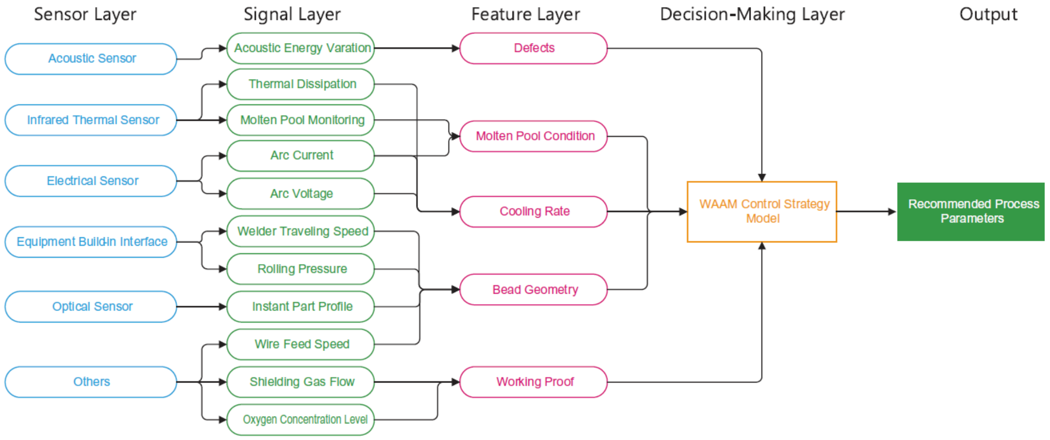

Figure 3.1: Shematic diagram of full state monitoring system for WAAM (Xu et al., 2018))

3.2.1.2 Simulation-based strategy optimization approaches

The basic idea behind simulation-based optimization was detailed by(Nguyen et al., 2014). This method was, for example, used to optimize part cooling during injection molding (Mathey, 2004), but also to improve the quality of parts produced with Electon Beam Melting (EBM) additive manufacturing, by optimizing melting strategies (Béraud et al., 2017; Beraud, 2016) and (Vignat et al., 2017). The coupling loop between simulation and optimization is illustrated in Figure 3.2.

In WAAM, process simulation was also used to study and optimize deposition strategies. (Lei et al., 2018) investigated the effect of inter layer idle-time on thermal behavior of thin-walled parts in WAAM, based on a finite element model, and showed that the total temperature gradient in the molten pool increases with the increasing idle-time. (Montevecchi et al., 2018) proposed an innovative technique based on a finite element model in order to schedule idle-times in WAAM, ensuring a constant inter-pass temperature and a constant molten pool size. (Zhao et al., 2020) proposed an alternative technique, aiming to improve layer's dimensional accuracy and manufacturing efficiency. In their approach, wire feed speed and travel speed are varied according to the predicted inter-pass temperature using a finite element simulation.

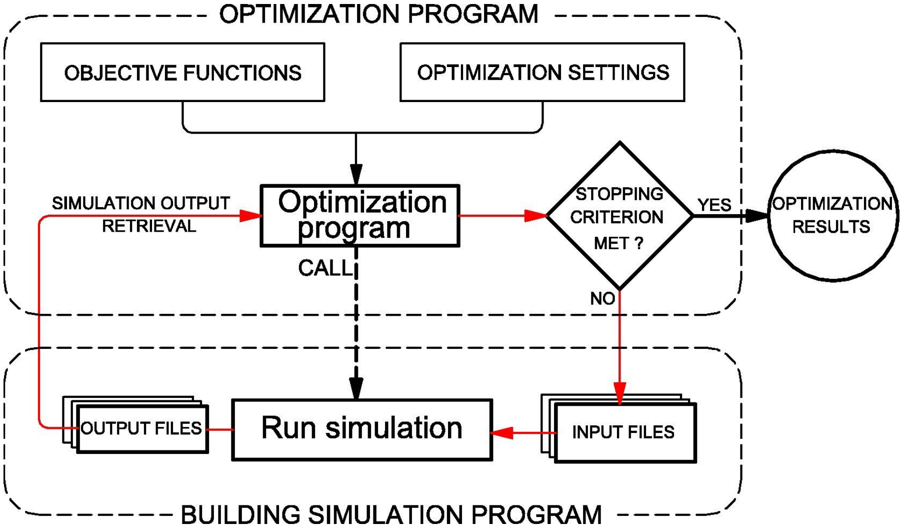

Figure 3.2: Simulation-based optimization principal (Nguyen et al., 2014)

3.2.2 WAAM process variants and in-process active cooling/heating techniques

A different approach to improve the quality of parts in WAAM other than adjusting the deposition strategy parameters, is the utilization of process add-ons and WAAM variants. In-process active cooling/heating techniques have already been tested in WAAM and can be considered as a promising alternative to control the thermal behavior in the produced parts. (Karunakaran et al., 2010) and (Ding et al., 2013) used water cooled fixtures to increase the heat sink effect of the substrate and enhance heat dissipation through conduction. In the same perspective, (Li et al., 2018) and (Shi et al., 2018) proposed a thermoelectric cooling system aiming to impose equivalent heat sink effect to the different layers of thin-walled parts. It was proven that the geometrical accuracy of the parts can be significantly improved with the aid of this technique. Another strategy is to increase the convective heat flux with the environment in order to mitigate heat accumulation in WAAM, using a near water-immersion active cooling technique, as proposed by (da Silva et al., 2020). (Montevecchi et al., 2018) proposed to increase the convective heat transfer using air jet impingement in order to prevent heat accumulation in the produced parts. (Wu et al., 2018) employed a forced interpass cooling using compressed CO2 in order to achieve a better quality in the WAAM of Ti6Al4V parts in terms of geometric accuracy, microstructure and mechanical properties.

3.3 Proposed deposition strategy optimization approach

As part of this thesis, simulation-based optimization method is adapted and specified for the optimization of deposition strategies in WAAM process. The aim is to improve the quality of the final parts in terms of geometric accuracy and material properties. The basic idea of the different techniques, that will be detailed later on, is to dictate the part's thermal history by adjusting the strategy parameters along the deposition path. The optimized strategies are determined based on the previously developed thermal simulation and thermal quality criteria, as shown in Figure 3.3.

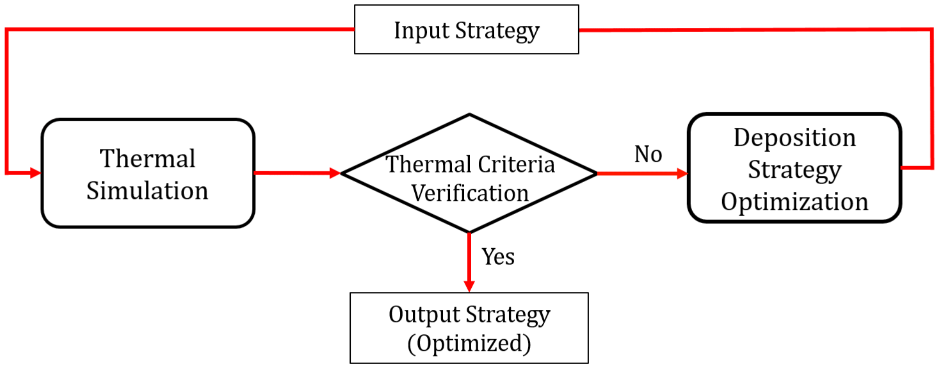

Figure 3.3: Proposed simulation-based strategy optimization in WAAM

The proposed simulation-based optimization approach consists of a closed loop that integrates several stages. This loop is executed at least once for each time-step of the deposition strategy concerned by the optimization. The different stages of the simulation-based optimization loop are detailed as follows:

Thermal simulation: The finite element simulation enables to analyze the thermal behavior of the part according to the input strategy. The temperature maps provided at the end of this stage will be used to calculate the different thermal quality criteria in the next stage, and will also serve as input data for the optimization function.

Thermal criteria verification: At this stage, an objective function is defined by setting a target in terms of thermal criteria. Then, the new thermal criteria, such as substrate temperature, or molten pool volume are calculated based on the temperature maps provided by the simulation, and subsequently compared with their targeted values. Input parameters will then become output parameters if the targeted criteria are reached. Otherwise, another iteration will be run.

Deposition strategy optimization: This step usually includes an optimization function, which allows to generate, from the results of the previous simulation, the deposition strategy parameters, a priori optimal, for the next simulation. The new parameters must allow the targeted thermal quality criteria to be met. The optimization function can take several forms. It can act as a proportional–integral–derivative (PID) controller, a model predictive controller, an iterative optimization algorithm, or a heuristic function.

Input strategy: These are the deposition strategy parameters initially set, or provided by the optimization function, which serve as input data for the following simulation.

Output strategy: These are the optimal deposition strategy parameters to meet the thermal quality criteria.

The usage of simulation in deposition strategy optimization rather than real-time monitoring has several advantages:

- Simulation allows offline optimization of WAAM process. This means that the optimization of deposition strategies is carried out upstream of the manufacturing process itself, which allows the latter to operate effortlessly, and still produce quality parts.
- It overcomes the problems often encountered in real-time temperature measurement, such as emissivity determination, and the interference coming from the electric arc and molten pool radiations.
- The previously developed thermal simulation provides access to more details regarding the thermal behavior in a valid and flexible way, which is

hardly achievable by means of direct measurements. In addition, it enables to optimize the deposition strategy parameters internally, by integrating optimization and correction algorithms into the simulation code.

- The optimization of the strategy parameters can be carried out using the different thermal quality criteria as optimization criteria.

In the following, two different techniques are developed based on the proposed simulation-based optimization approach. Both techniques aim to improve the quality of thin-walled parts manufactured in WAAM, by optimizing two different strategy parameters, separately: (i) Idle-times between layers, and (ii) energy input.

3.4 Idle-time optimization technique

As seen in the previous chapter, heat accumulation along build direction is one of the main thermal issues when fabricating thin-walled parts. With the increase in the number of layers, the heat dissipation conditions in the subsequent layers worsen, the cooling rates decrease, and the interlayer substrate temperature increases. This would lead to the variation of the layer's dimensions. As the part grows tall, this dimensional error will accumulate, resulting in a significant variation in the part's width and an obvious loss of its total height. Moreover, the molten pool grows bigger, and the temperatures reach higher values in the upper layers, which would increase the probability of pore formation.

Introduction of interlayer idle-times in WAAM deposition strategies remains a common practice in order to mitigate such issue. These inactive time intervals between layers would allow the part to cool down by transferring the excessive heat to the environment through conduction and convection. Hence, adjusting this parameter enables to control the interpass temperature between layers, and therefore the quality of each layer.

Today, idle-time determination and scheduling in WAAM process remains a matter of research, as it depends on several parameters: the geometry of the part, metallurgical properties of the wire, and the welding mode. And beyond these variables, it is difficult to achieve a compromise between quality and productivity. For now, the scheduling of idle-times can be done either by introducing fixed idle-times at the end of the deposition of each layer, or by monitoring the interpass temperature, namely, the interlayer substrate temperature at the start of the deposition of each layer. The first approach can be adopted in the absence of interpass temperature monitoring techniques. Nevertheless, series of trial and error tests are necessary to determine an appropriate idle-time value. The drawback of this method is that a constant idle-time does not necessarily ensure a constant interpass temperature, due to the difference in heat dissipation conditions in the successive layers. Therefore, a variation in the quality of the fabricated part can still be observed along build direction. The second approach, on the other hand, seems to be more efficient in order to maintain a constant interpass temperature and ensure the desired quality. This is achieved by varying the idle-times along the deposition process using a real-time monitoring technique to control the interpass temperature (often using a thermocouple, an IR camera, or a pyrometer), or by means of a reliable simulation. This idea has already been proposed in literature by (Montevecchi et al., 2018), and it has been proven to be effective in improving the geometric accuracy of the deposited layers. However, in this approach, the idle-time determination is not automatic, and requires a relatively long numerical-chain, with an interruption of the simulation between each two layers. More precisely, the proposed technique requires a twin-model, one for the heating (deposition) phase, and a second for the cooling phase, and the calculation of the idles times is performed externally, via a MATLAB code. In addition, the cooling phase is simulated for a fairly long time, and the cooling curve of a single node (control point) is subsequently processed in order to determine the idle-time required to reach the desired interpass temperature.

In this section, the approach proposed by (Montevecchi et al., 2018) is adapted and further developed in order to optimize idle-times in WAAM of thin-walled parts. The previously developed finite-element simulation and substrate temperature criterion are used to reliably predict and control the interpass temperature. An optimization algorithm is integrated to the finite-element code, allowing to select the appropriate idle-time for each layer, with the objective of maintaining a constant interpass temperature.

3.4.1 Technique description

The proposed simulation-based idle-time optimization loop consists of the following steps, outlined in Figure 3.4 and Figure 3.5. These steps are repeated for each layer of the deposited thin-wall part:

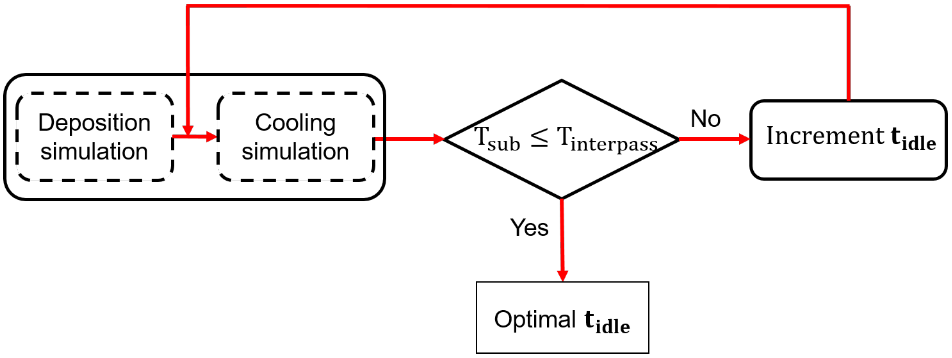

Figure 3.4: Idle-time optimization technique

- Simulation: First, the deposition of the current layer is completely simulated with the predefined deposition strategy. In the present case, a thin-wall part is fabricated according to a zigzag trajectory, and all the strategy parameters such as heat input, wire feed speed, and travel speed, are kept constant. Then, the simulation of the natural cooling phase takes part. Only, at this stage, the cooling simulation is controlled by the other functions of the optimization loop, i.e., the objective and the optimization functions. These are called after each time-step in the cooling phase, deciding to continue or stop the cooling of the current layer.

- Thermal criteria verification: The set objective function is to ensure a constant interpass temperature for all deposited layers. For this purpose, the substrate temperature criterion (T_{sub}) is used to monitor the inter-layer substrate temperature. In fact, this criterion was originally designed to locally track the substrate temperature on which each droplet is deposited, but it is used differently in the proposed optimization loop. Indeed, in order to calculate the inter-layer temperature, the T_{sub} criterion is calculated over the entire layer, once the deposition of the layer in question has ended. The average inter-layer substrate temperature is therefore calculated using a significant number of control nodes, evenly distributed on the top surface of the last deposited layer, as illustrated in Figure 3.5. This control is systematically performed after each time-step in the cooling phase simulation. The value of the criterion must reach the targeted interpass temperature, i.e : $T_{sub} \leq T_{interpass}$. If this condition is met, the corresponding cooling time is selected as the optimal idle-time for the current layer. Otherwise, the optimization loop will be run for another iteration.

- Idle-time increment function: In the present case, the role of the optimization function is simply to increment the idle-time if the targeted interpass temperature is not reached, and to subsequently launch the cooling simulation for another iteration, taking the new idl-time as input parameter.

The purpose of the proposed technique is to ensure the same forming conditions for all layers by imposing a constant interpass temperature at the beginning of each layer deposition. Therefore, the selection of the appropriate interpass temperature is crucial in order to ensure the layer's desired quality. However, choosing a proper interpass temperature is a tedious task, that depends on several variables, including:

- The interpass temperature sensitivity to the layer's quality: a too low interpass temperature may cause the humping defect, because of the layer's premature solidification. A high one, on the other hand, does not allow the part to cool down sufficiently, and tends to cause inconsistent layer dimensions.
- The material used: interpass temperature highly depends on the metallurgical properties of the deposited wire, such as melting point and conductivity. It is important to refer to the literature that provides the appropriate value for the considered material. In the absence of this data, trial and error remains the common way to fix a suitable interpass temperature.
- The impact on the production efficiency: The selection of optimal idle-time values depends on the fixed interpass temperature. Figure 3.6 highlights the k-th layer simulated cooling curve during a thin-wall part manufacturing. As shown in the figure, the lower the interpass temperature, the higher the idle time value, and therefore the total manufacturing time of the thin-wall part. For instance, by setting an interpass temperature of 200 °C, the resulting idle-time would be around 25 seconds. However, if the interpasse temperature is set to 50°C, the corresponding idle-time would be 270 seconds, that is, ten times longer.

In the present case, the interpass temperature value is set at 150°C. This choice is suitable for the material used (aluminum alloy 5356), and ensures a good compromise between the quality of the deposited layers and productivity.

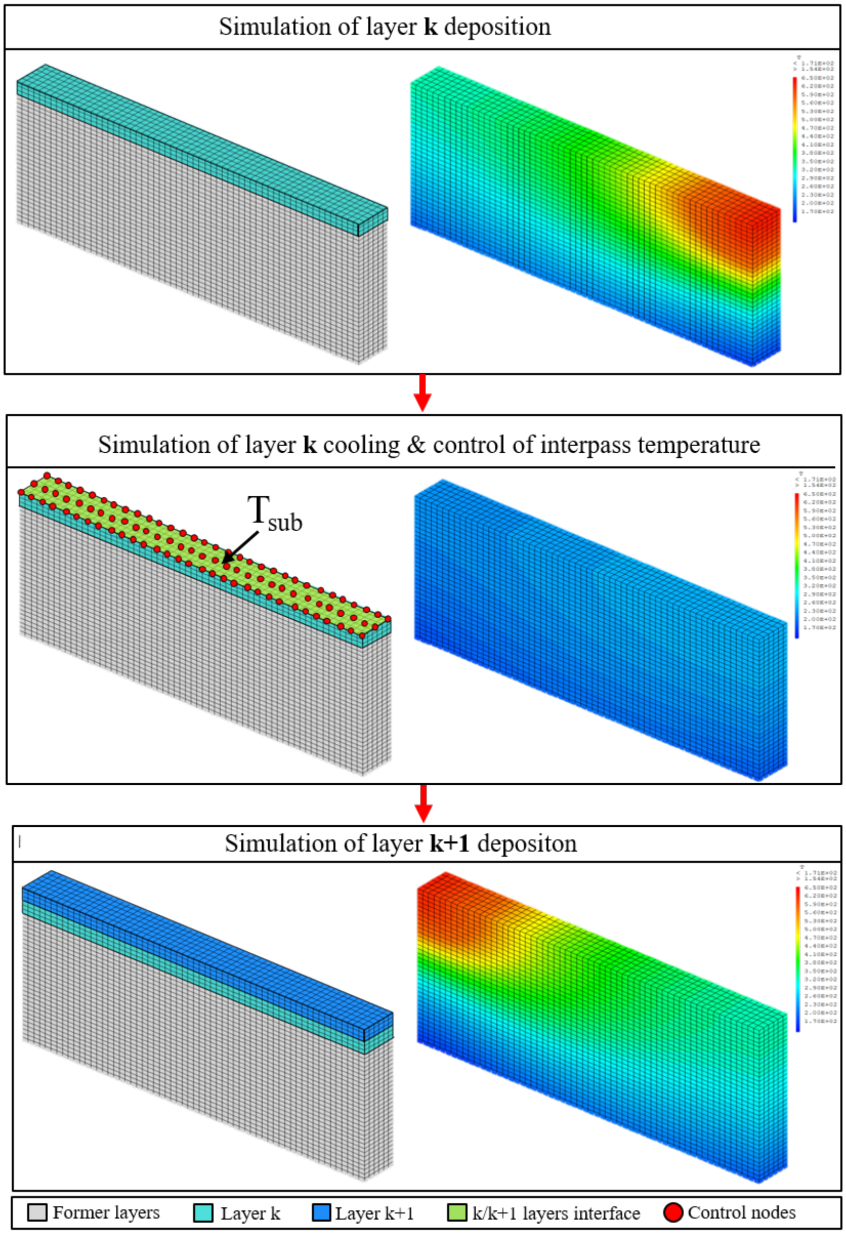

Figure 3.5: Inter-layer substrate temperature control

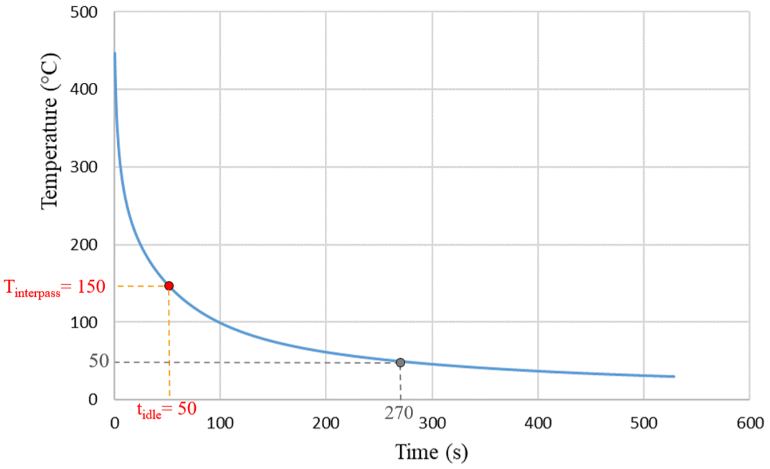

Figure 3.6: Interpass temperature evolution during cooling simulation

3.4.2 Validation test case

In order to verify the effectiveness of the proposed simulation-based idle-time optimization technique, a test case consisting of fabricating a thin-wall part according to two different deposition strategies is carried out. The schematic and dimensions of the part are shown in Figure 3.7. In the first strategy, the idle-time is set at 2 seconds for all layers, while in the second strategy, idle-times are calculated using the proposed technique. The parameters of both deposition strategies are listed in Table 3.1. The thermal behavior of the part under both strategies is simulated using the finite-element simulation, and the different thermal quality criteria are calculated in order to assess the quality of the fabricated parts.

	Deposition trajectory	Energy input (J/mm)	Travel speed (mm/s)	Wire feed speed (m/min)	Idle-time(s)
Strategy 1	Zigzag	77.8	10	5	2
Strategy 2	Zigzag	77.8	10	5	Variable (optimal)

Table 3.1: Test-case strategies parameters

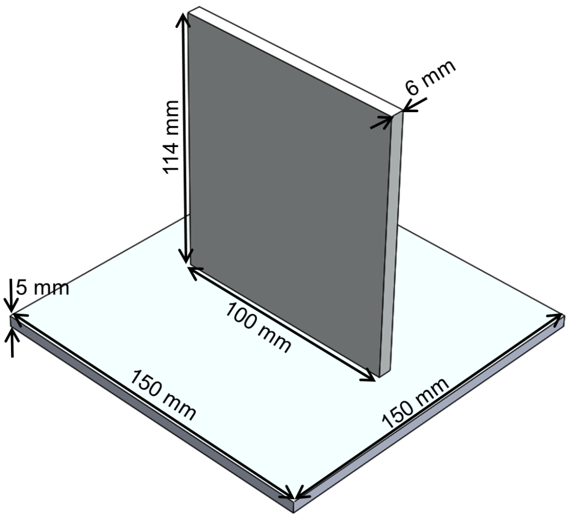

Figure 3.7: Test case part

3.4.3 Results

3.4.3.1 Idle time and interpass temperature evolution

The simulation results in terms of idle-times and interpass temperature as functions of layer's index for strategy 1 and strategy 2 are shown in Figure 3.8 and 3.9, respectively. In strategy 1, the introduction of a short and constant idle-time (2 seconds) led to a continuous increase in interpass temperature with the increasing number of layers, reaching its highest peak at the 60th layer. In contrast, in strategy 2, the idle-time is varied along the deposition process in order to ensure a constant interpass temperature (150°C). Indeed, the idle-time increases continuously with the increasing number of layers in order to compensate the reduction of the conductive heat flux towards the substrate plate. In fact, two regions, with different rate of increase, can be observed in the idle time evolution curve. The first region corresponds to the first layers, where the molten pool is close to the substrate plate. Because of the heat sink effect, the heat is mainly dissipated through conduction towards the substrate plate, which remains relatively cold as the first few layers are deposited. This explains the quick cooling of the first layers, where shorter idle-times are required in order to achieve the targeted interpass temperature. As the part grows tall, the substrate plate becomes saturated, the heat sink effect is significantly reduced, and the molten pool distance to the substrate plate increases. Moreover, the part's external surface increases with the increasing number of layers, which causes the heat to be dissipated mainly through convection. Only at this stage, longer idle-times are required for the part to cool down, as described in the second region of the idle-time curve.

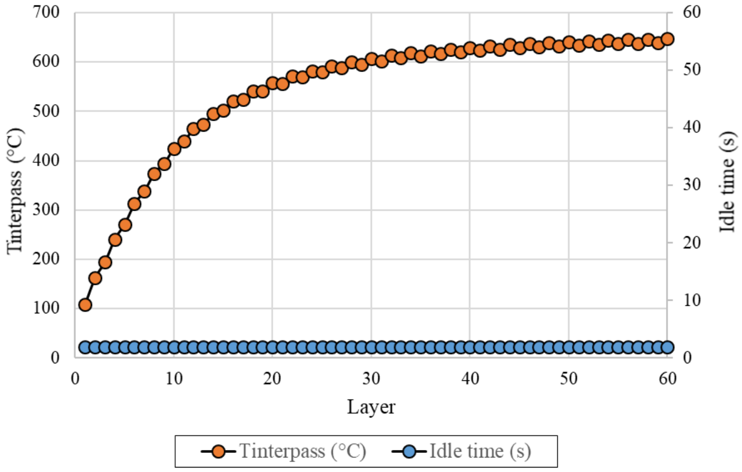

Figure 3.8: Interpass temperature and idle-time evolution in strategy 1

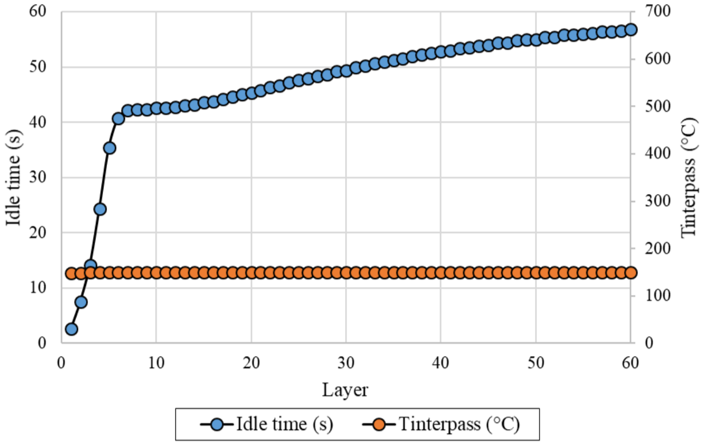

Figure 3.9: Interpass temperature and idle-time evolution in strategy 2

3.4.3.2 Thermal quality criteria

In order to evaluate the two deposition strategies and predict the defects that may occur in the manufactured thin-wall parts, the different thermal quality criteria presented in the previous chapter are calculated and discussed in the following.

Average temperature above solidus (ATAS)

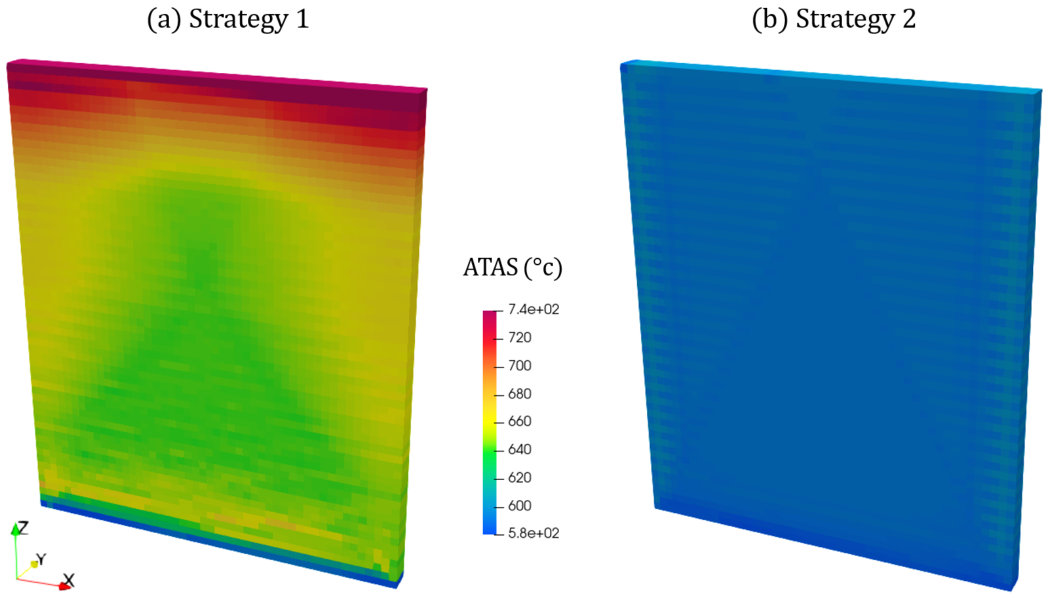

Figure 3.10: Results of average temperature above solidus (ATAS) for: (a) strategy 1; (b) strategy 2

In order to evaluate the dimensional accuracy of the fabricated parts along build direction, the average temperature above solidus (ATAS) criterion is calculated for both strategies, and can be visualized in Figure 3.10. In strategy 1, the criterion increases significantly with the increasing number of layers, as shown in Figure 3.10.a. Its value increases from 590°C to 830° between the 1^{st} and the 60^{th} layer. This important increase in ATAS criterion indicates that the part would experience a strong heat accumulation along build direction due to the insufficient idle-times, which would result in a significant variation in the part's width along this direction. As for the thin-wall part manufactured according to strategy 2, the calculted ATAS criterion is shown to be constant along build direction, as can be seen in Figure 3.10.b. In fact, the introduction of optimal idle-times prevented heat accumulation in build direction, and kept the value of the criterion around 590°C for all layers. As a result, the width of the manufactured thin-wall part would be kept constant in this direction.

Maximum temperature ($\mathbf{T_{max}}$)

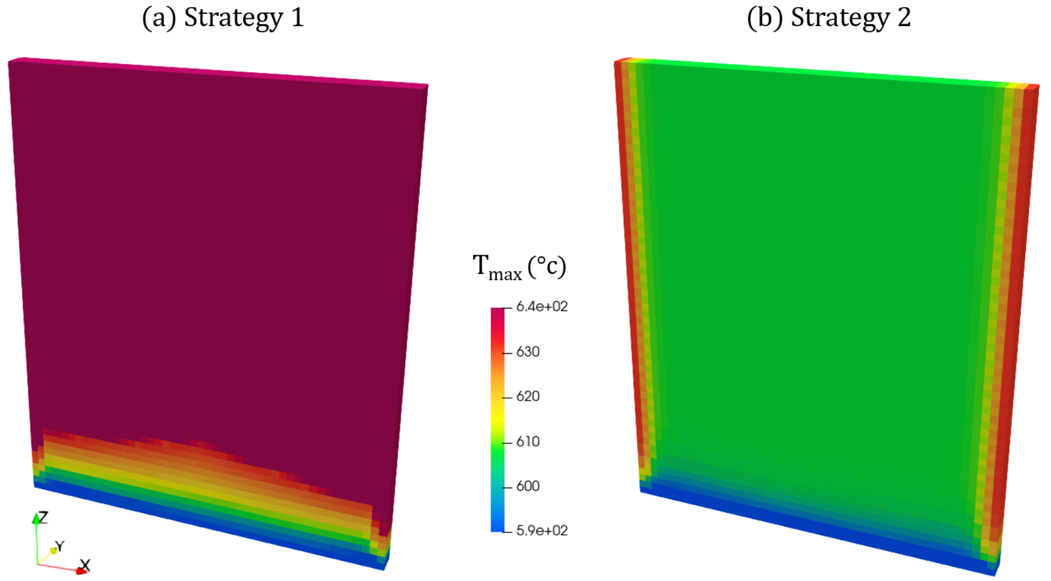

Figure 3.11: Results of maximum temperature criterion ($T_{max)}$ for: (a) strategy 1 and (b) strategy 2

The results of maximum temperature (T_{max}) criterion calculated for both strategies can be visualized in Figure 3.11. For strategy 1, the maximum temperature reached exceeds liquidus temperature for all portions of the deposited layers, starting from the 10th layer. This indicates that the part experiences a significant overheating on all portions of the deposited layers, as shown in Figure 3.11.a. This overheating would lead to a significant collapse of the different portions of the deposited layers and a significant loss in the part's total height. In strategy 2, the maximum temperature reached by the elements representing the middle and largest portion of the thin-wall part is kept constant at 607°C, as shown in Figure 3.11.b. However, on the start/end portions of the part, the deposited droplets are overheated, since the criterion value in these portions is higher than that of the middle potion. Consequently, the part is prone to the collapse of the start/end portions of the part relative to its middle portion.

The criterion also shows that the first two layers remain relatively cold in both strategies, indicating their quick solidification due the strong heat sink effect. In fact, at the beginning of the deposition process, the substrate plate is at room temperature, resulting in an excellent heat dissipation conditions. Therefore, the deposited droplets solidifies quickly and do not have enough time to spread. Thus, the first deposited layers are expected to be narrower and higher, and their grip to the substrate would appear fragile.

Molten pool volume (MPV)

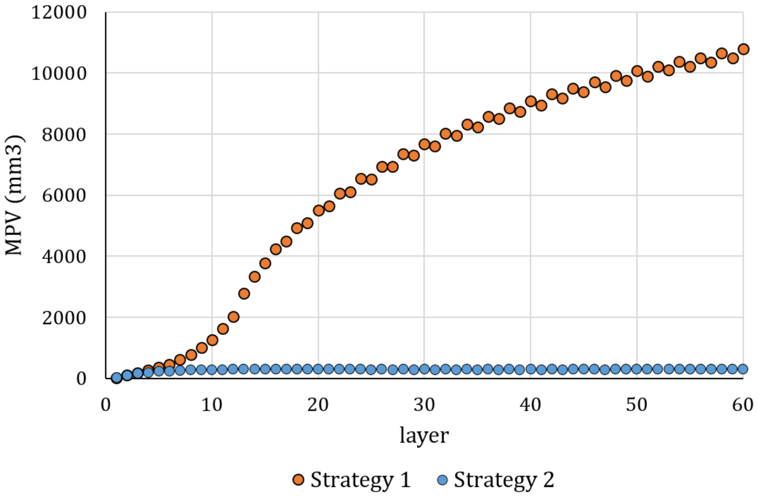

Figure 3.12: Comparison of molten pool volume criterion (MPV) between strategy 1 and strategy 2

The material integrity of the thin-wall part under both strategies can be evaluated using the molten pool volume criterion (MPV), since the latter correlates best with the evolution of porosity rate, as seen in the previous chapter. This criterion is calculated based on the simulated thermal history of both strategies, and its evolution according to build direction is shown in Figure 3.12. The results shows that the molten pool volume in the wall-part manufactured according to strategy 1 significantly increases with the increase in the number of layers, indicating a significant increases in porosity rate and pores size in this direction. As for the thin-wall part fabricated according to strategy 2, the molten pool volume is much smaller than that of strategy 1, and remains constant (3500 mm^3) along build direction, except for the first ten layers where the molten pool is slightly smaller due to heat sink effect. This means that in strategy 2, the porosity rate remains much lower and constant along build direction compared to strategy 1.

3.4.3.3 Fabricated thin-wall parts

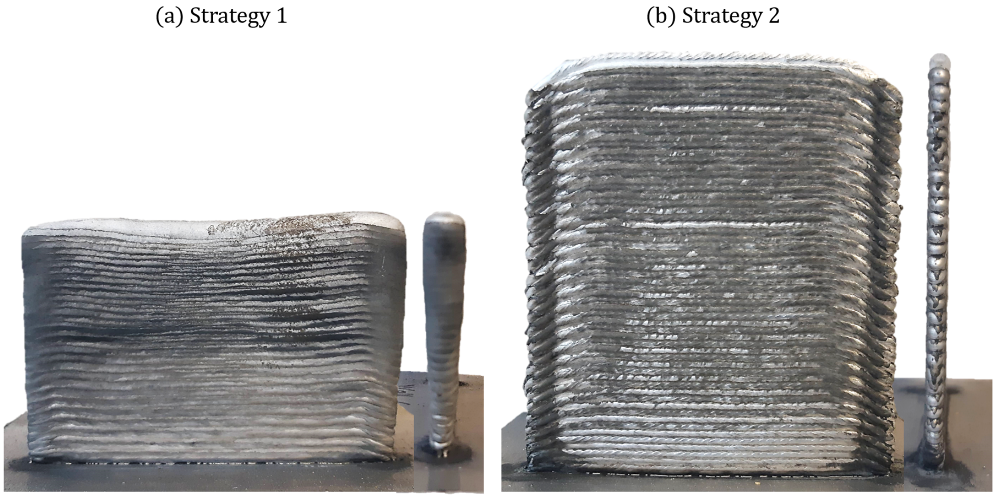

Figure 3.13: Thin-wall part fabricated according to (a) strategy 1; (b) strategy 2

The actual thin-wall parts are fabricated according to both strategies and shown in Figure 3.13. As expected, the important heat accumulation and overheating experienced by the part manufactured according to strategy 1 led to a significant variation in the layers dimensions along build direction. As shown in Figure 3.13.a, the part manufactured under this strategy exhibits a great variation in total width along build direction and a great loss in total height. In contrast, the quality of the part manufactured according to strategy 2 has been significantly improved compared to strategy 1, as shown in Figure 3.13.b. The introduction of optimal idle-times into the deposition strategy allowed to ensure the same deposition conditions for all deposited layers. As a result, the part's total width is shown to be constant along build direction, and it's total height is significantly corrected. However, a start/end deposition defect can be observed on the fabricated part, as predicted previously. In fact, a significant height difference can be noticed between the start/end portions and the middle portion of the thin-wall part. This defect remain uncorrected using the proposed idle-time optimization technique, and requires further optimization and correction.

3.4.3.4 Summary

Overall, the proposed simulation-based idle-time optimization technique allowed to dictate the desired thermal history by introducing the appropriate idle-time for each layer and ensuring a constant interpass temperature. This allowed to improve the quality of the manufactured thin-wall part in terms of dimensional accuracy and metallurgical integrity, which was verified using the different thermal quality criteria. These improvements can be summarized as follows:

- The introduction of optimal idle-times allowed to achieve a constant substrate temperature for all layers and eliminate heat accumulation along build direction, as demonstrated using ATAS criteria. As a result, the layers dimensional accuracy is kept constant along build direction, which made it possible to ensure a constant part width along build direction, and significantly correct it's total height.

- The overheating and remelting phenomena were significantly reduced in most regions of the part, as demonstrated using T_{max} criterion, which helped avoid major rheological deformations and collapses in the final thin-wall part.

- The proposed technique allowed to limit the increase in the molten pool size, responsible for porosity formation, and enabled to ensure a low and constant porosity rate along build direction, as verified using MPV criterion.

However, two major geometric quality issues remain unresolved. Namely, the weak grip of the part to the substrate plate due to the quick solidification of the first layers, and the start/end deposition failures caused by the overheating phenomena occurring at the start/end portions of the thin-wall part. The first issue can be easily tackled by preheating the substrate plate at the previously set interpass temperature, thus eliminating the heat sink effect. The start/end deposition failures issue however, is a little more difficult to manage and requires adjusting another deposition strategy parameter: the energy input.

3.5 Energy-input

One of the most relevant deposition strategy parameters affecting the thermal history of the deposited layers is the energy input. This parameter can be defined as the amount of energy supplied to the part by means of arc direct transfer and wire melting energy, for a given length traveled by the torch. Also known as linear energy or line-energy. It is measured in units of energy per unit length, and can be calculated using the following formula:

$$EI = \frac{\eta U I}{TS} \tag{3.1}$$

Where U and I are the arc voltage and current, η is the welding efficiency, and TS is the travel speed.

3.5.1 Process parameters affecting energy input

As described above, energy input is variable dependent of two description parameters, the arc voltage and current (U and I). However, these two parameters are not directly controllable but rather depend on several process parameters, in particular:

3.5.1.1 CMT-mode

As detailed in chapter 1, CMT process offers four welding modes, namely, CMT, CMT Pulse (CMT-P), CMT Advanced (CMT-ADV), and CMT Pulse Advanced (CMT-PADV). These variants differ from each other in arc phases, current and voltage curves, droplets detachment mode, and therefore in heat input. In order to illustrate this difference, four separate beads were deposited under the same substrate temperature conditions, with the same wire feed and travel speeds ($\mathrm{R}_{\mathrm{WFS/TS}}$

= 0.5). The average values of arc current and voltage are recorded, and the corresponding energy inputs are calculated subsequently. Results are presented in Table 3.2, and the four deposited beads are shown in Figure 3.14.

Mode	WFS (m/min)	TS (mm/s)	I (A)	U (V)	Power (W)	EI (J/mm)
CMT	5	10	81	12.5	840.4	84
CMT-P			100	16.9	1402.7	140.3
CMT-ADV			80	9.5	630.8	63.1
CMT-PADV			85	11.7	825.4	82.5

Table 3.2: CMT mode influence

The results shows that the arc current and voltage varies considerably when changing the CMT mode. The CMT-ADV mode remains the coldest among the four modes, but this is only true over a range of wire feed speeds. For wire feed speeds above 5.5 m/min, the CMT-PADV mode guarantees a lower heat input. CMT-P mode is shown to be the hottest mode, with an increased energy input compared to the other modes. The impact of these modes energy levels on the geometric quality of the deposited beads can be observed in Figure 3.14.

The CMT mode is a parameter that can be controlled directly by the user in order to adjust the energy input, but this is still not recommended because the metallurgical quality changes considerably when changing mode, as explained in the previous chapter. Consequently, the manufactured parts would presents dispersed porosity levels, which correspond to the interchanged CMT modes. Moreover, it is not possible to change modes within the same layer without arc extinguishing. This restricts the change of CMT-mode to only between layers.

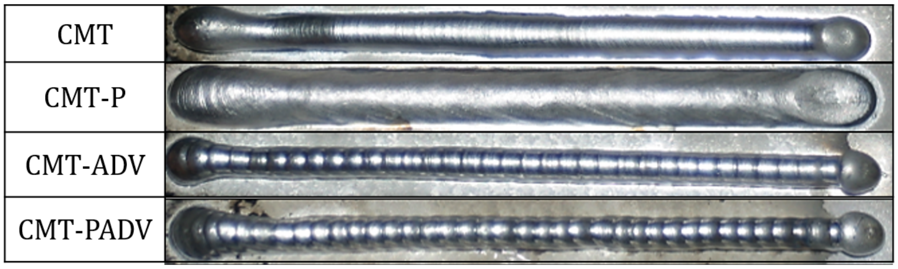

Figure 3.14: CMT mode influence

3.5.1.2 Positive and negative polarity ratio (EP/EN)

A more controlled heat input can be achieved using the variable polarity variant of CMT process, i.e. the CMT advanced mode. In this welding mode, the synergic cycle is composed of both positive and negative electrode semi-cycles, with an electrode polarity reversal taking place in the short circuit phase. Because of this polarity reversal feature, the arc current and voltage are varied depending on the time spent with the electrode in the positive polarity (EP) and in the negative polarity (EN), and can be adjusted using the CMT-ADV process parameter EP/EN. This parameter is defined as the ratio of positive electrode semi-cycles to negative electrode semi-cycles, and ranges from -5 to +5.

In order to assess the influence of EP/EN polarity ratio on the energy input levels, an experimental procedure was carried out, where eleven separate beads are deposited side-to-side, with the eleven EP/EN values as variables. The beads were deposited under the same substrate plate temperature conditions (25°C), with a constant wire feed and travel speeds. The average deposition arc current and voltage are recorded, and the corresponding energy inputs are calculated. The experiment results are detailed in Table 3.3 and Figure 3.15, and the eleven deposited beads are shown in Figure 3.16.

EP/EN	WFS (m/min)	$R_{WFS/TS}$	I (A)	U (V)	EI (J/mm)
-5	10	0.5	73.8	8.7	53.4
-4			73.8	8.9	53.8
-3			73.9	8.7	53.4
-2			73.9	8.7	53.5
-1			76.8	10.6	60.4
0			79.6	11.4	70.1
+1			82.1	12.1	77.8
+2			84.1	12.1	84.3
+3			84.1	12.1	84.5
+4			84.3	12.1	84.8
+5			84.1	12.1	84.4

Table 3.3: EP/EN influence

The results show that the arc current and voltage, and therefore the energy input, increases when EP/EN switches towards positive polarity. This increase is more tangible when EP/EN ranges from -2 to +2. In this range, the energy input increases proportionally to the EP/EN ratio, while it tends to be constant when EP/EN is under -2 or above +2, as shown in Figure 3.16. Also, the very low heat input induced by the extreme negative values of EP/EN (below -2) hinders the formation of a continues layer, and gives a balling appearance to the deposited layer, as shown in Figure 3.16. In fact, when changing EP/EN towards extremely negative values, the travel speed becomes too high in relation to the energy input, thus leading to the premature solidification of the deposited droplets. This defect can accumulate and turn into a part-scale humping, but can be rectified by reducing the travel speed, or by preheating the substrate if the travel speed is forced to remain constant.

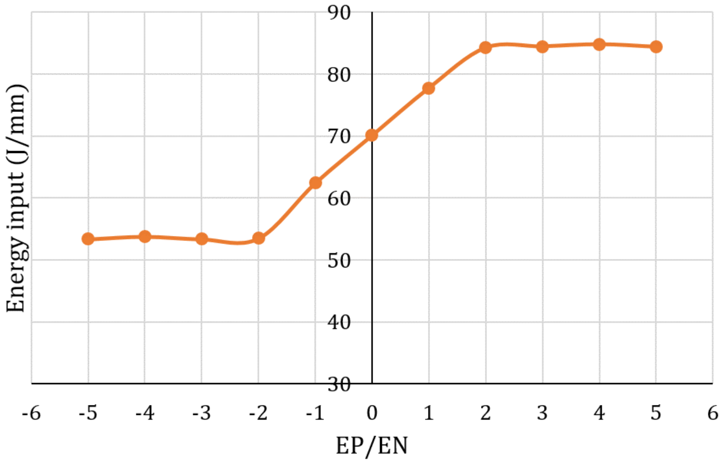

Figure 3.15: EP/EN influence

The EP/EN polarity ratio can be considered as an attractive deposition strategy parameter, since it can be used to adjust the energy input between layers but also within the same layer without arc extinguishing. In addition, it makes it possible to modulate the energy input while remaining in the same welding mode (CMT-ADV), thus avoiding having different metallurgical properties within the same part due to the interchange of welding modes.

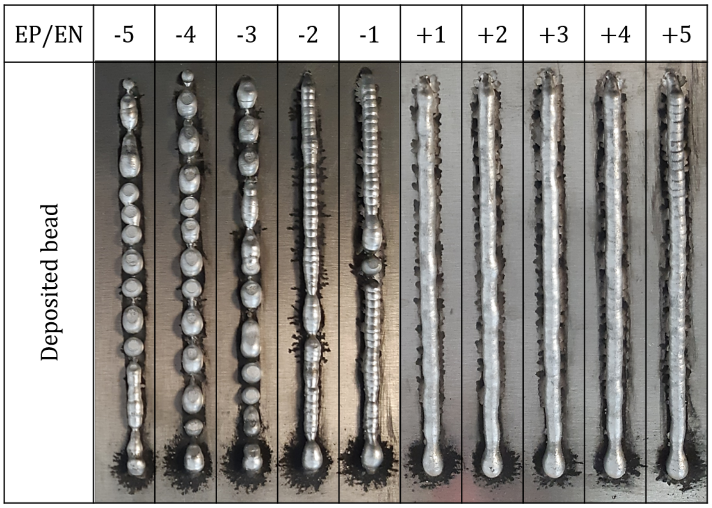

Figure 3.16: EP/EN influence

3.5.1.3 Wire feed speed (WFS)

The arc current and voltage are also known to vary as a function of wire feed speed (WFS), as verified in welding literature. This is because the amount of weld metal that is deposited during a given time interval is controlled by the arc current, and the arc length, i.e. the distance between the molten pool and the wire, is controlled by the arc voltage. In order to assess the influence of wire feed speed on arc current, voltage, and energy input, another experimental procedure was carried out. In this procedure, the wire feed speed is varied according to ten values. These values correspond to the ten inflection points, as defined by the welding mode CMT-ADV. However, in order to ensure a constant deposited volume, the ratio of wire feed speed to travel speed ($\mathrm{R}_{\mathrm{WFS/TS}}$) should be kept constant. For this reason, the travel speed (TS) is also varied in order to ensure a constant $\mathrm{R}_{\mathrm{WFS/TS}}$, which is set at 0.5 in the present case. The ten beads are deposited under the same substrate temperature conditions, and the EP/EN polarity ratio is set at 0. The experiment data and results are detailed in Table 3.4 and Figure 3.17. The ten deposited beads are shown in Figure 3.18.

WFS (m/min)	TS (mm/s)	$R_{WFS/TS}$	EP/EN	I (A)	U (V)	EI (J/mm)
2.2	4.4	0.5	0	51	8.6	82.4
3.1	6.2			60.6	8.9	72.7
4.2	8.4			73.2	9.4	67.7
5	10			79.6	10.6	70.1
5.34	10.68			86	11.9	79.2
5.5	11			87.9	12.2	81
5.6	11.2			108.8	14.2	114.2
6	12			119.5	15.5	129.4
6.6	13.2			130.2	16.9	138.4
8.2	16.4			157.6	17.6	140.3

Table 3.4: WFS influence

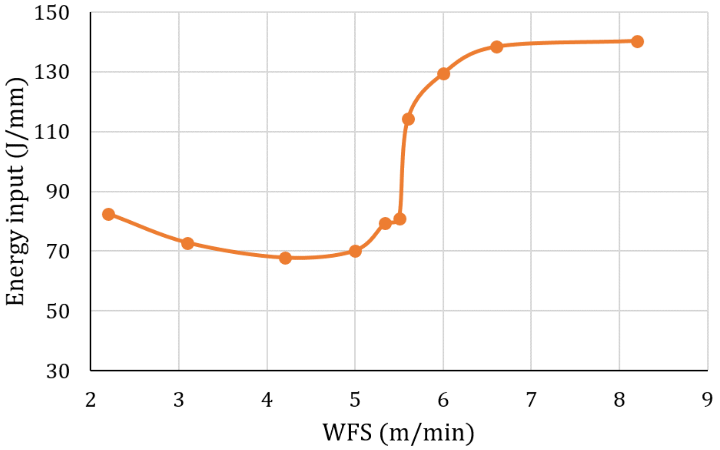

Figure 3.17: WFS influence

The results shows that the arc current and voltage continuously increases with the increase of WFS. In other words, the arc total power increases with the increase of WFS. However, the energy input does not vary in the same manner due to the variation of travel speed (TS). This energy input begins by decreasing slightly between WFS = 2.2 m/min and WFS =4.2 m/min, to increase again according to different rates from WFS = 5 m/min, and its value is double value when reaching WFS of 8.2 m/min. It is important to note that the energy input and therefore the geometric quality of the deposited beads varies considerably, as shown in Figure 3.18, even though the deposited volume is kept constant($R_{WFS/TS}$=0.5). This can be very useful subsequently, in adjusting the energy input while ensuring a constant deposition volume.

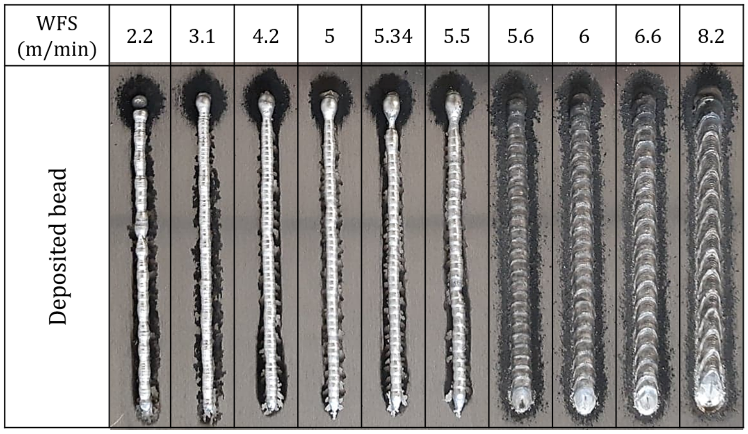

Figure 3.18: WFS influence

3.5.2 Effect of energy input on thermal behavior and layers quality

Energy input is an important characteristic because it affects different thermal aspects, such as the molten pool size, the peak temperature, and the cooling rate. Therefore, the geometric quality and the material properties of the deposited layers are highly impacted by this parameter. In order to illustrate the influence of energy input on the thermal behavior and the geometric quality of the deposited layers, eight beads were deposited with an increasing energy input for each layer, as detailed in Table 3.5. These beads are deposited under the same temperature conditions of the substrate plate (25°C), and a constant ratio of the wire feed speed to travel speed ($R_{WFS/TS}$=0.5), ensuring the same amount of deposited material per bead. The eight deposited beads are shown in Figure 3.19.

Bead	1	2	3	4	5	6	7	8
I (A)	8.6	8.8	10.9	11.3	13.1	14.3	15.6	16.2
U (V)	70.6	76.8	82.9	84.8	104.9	115.3	125.6	152.1
EI (J/mm)	60.3	62.4	70.53	72.12	101.6	114.3	123.2	124.9

Table 3.5: Ten case energy input

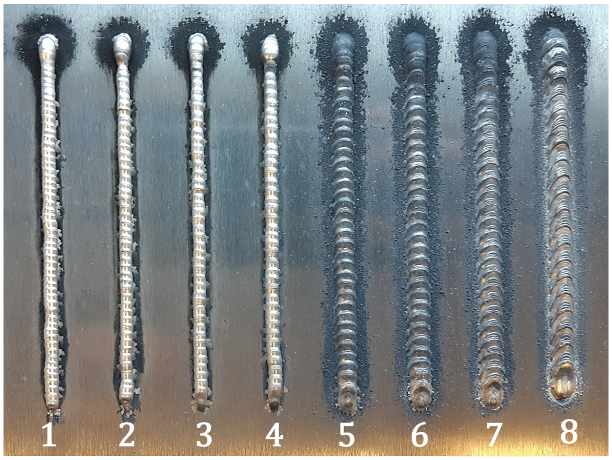

Figure 3.19: Ten deposited beads

The deposition and the cooling phases of beads 1, 5 and 8 were simulated using the finite element simulation, and the evolution of substrate temperature, cooling rate, maximum temperature and molten pool volume for the three beads are shown in Figure 3.20. Comparisons show that the increase in energy input results in a significant increase in the bead's substrate temperature and molten pool size, as shown in Figure 3.20.a and Figure 3.20.c, respectively. The cooling curves of the middle point of the three beads are presented in Figure 3.20.b, and shown to have different rates. In fact, the higher the energy input, the longer the cooling time. Also, the maximum temperature reached by the middle point of each bead highly increases with increase in the energy input. As it can be seen from Figure 3.20.b, the maximum temperature values are 486.4°C, 631.5°C, and 981.8°C for bead 1, bead 5 and bead 8, respectively .

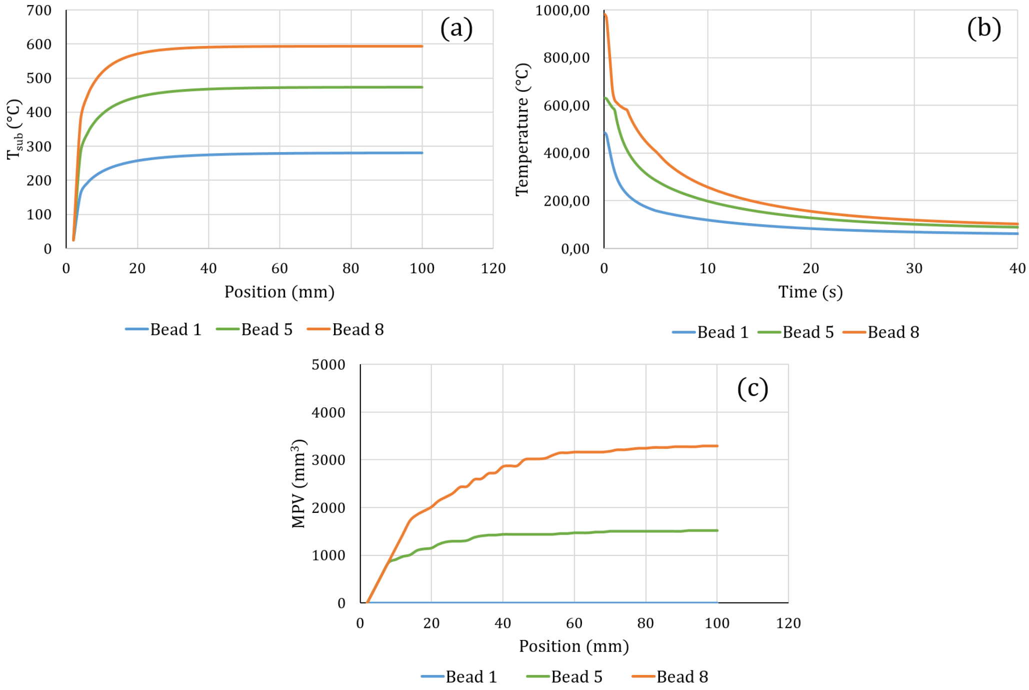

Figure 3.20: Energy input influence on: (a) Substrate temperature (Tsub); (b) cooling rate; (c) molten pool volume (MPV) for layers 1, 5, and 8

The results also show that the geometry of the deposited beads changes with the increase in the energy input, as it can be seen in Figure 3.19, but also in Figure 3.16 and 3.18. The beads deposited with a low energy input tend to be narrow and tall, but turns wider and flattened with the increasing energy input. This is because low energy input would result in a low substrate temperature, a smaller molten pool and a quick solidification of the deposited droplets, as shown in Figure 3.20. On the other hand, high energy input would result in a high substrate temperature, a wider molten pool, and a slower cooling rate. As a result, the deposited bead would be wider and flattened (Manokruang et al., 2020).

3.5.3 Conclusion

For deposition strategies optimization purposes, the use of wire feed speed (WFS) as well as EP/EN polarity ratio as optimization parameters seems to be relevant. These two process parameters can be controlled directly by the user, making it possible to modulate the energy input and dictate the desired thermal history. In addition, these two parameters allow to vary the energy input within the same layer while ensuring a continues and a constant volume of deposited material. Moreover, it is possible to combine both WFS and EP/EN polarity ratio and adjust both parameters simultaneously, thus enabling to access to a maximum of energy input levels. To this end, the two curves of energy-input as a function of EP/EN polarity ratio and WFS, shown in Figures 3.17 and 3.19 respectively, are combined. Consequently, the evolution of energy input as a function of wire feed speed, and EP/EN polarity ratio is constructed, and the obtained response surface is shown in Figure 3.21. The latter consists of 110 points, which corresponds to the possible energy levels obtained by varying EP/EN (ranging from -5 to +5), and WFS (ranging from 2.2 m/min to 8.2 m/min). Also, an experimental verification was carried out, consisting of depositing several separate beads, with different combinations of EP/EN polarity ratio and WFS. The beads were deposited under the same substrate temperature conditions, and the arc current and voltage, and therefore the energy-input levels were recorded, and found to be in agreement with the constructed ones.

It is important to note that the obtained energy input levels are not exhaustive, but rather correspond to a constant $R_{WFS/TS}$ratio, set at 0.5 in the present case. Therefore, the travel speed (TS) is varied depending on this ratio, but other energy levels can be accessed by changing the ratio. In the present case, the constructed response surface allows to determine, based on the targeted energy input, the suitable parameter pair (WFS , EP/EN). Possible energy input levels ranges from 51.55 J/mm to 169.75 J/mm, which is a fairly large range for strategy optimization purposes. Also, It can be seen that certain combinations of WFS and EP/EN provide the same energy inputs. These duplicates may be removed to simplify the search for possible solutions, but it is rather useful to keep them as alternatives, in the case where the energy supplied is too low compared to the torch travel speed. Thus avoiding the appearance of humping defect.

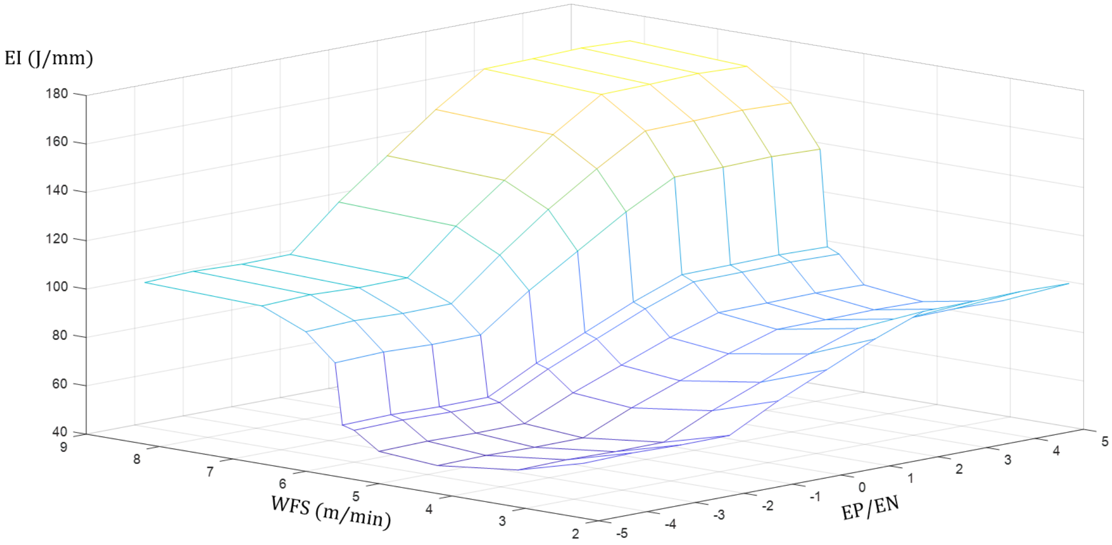

Figure 3.21: Energy input

3.6 Energy-input optimization technique

Recall that the problem of start/end deposition failures remain unsolved. This defect caused by the strong overheating phenomena occurring at the end portion of each layer proves difficult to rectify by optimizing idle-times only. For this reason, another simulation-based optimization technique is proposed in order to tackle this issue. The basic idea of this technique is to adjust the energy input at the end of each layer in order to ensure the same deposition conditions between the middle and the end portions of each layer. This energy-input optimization technique works in combination with the idle-time optimization technique. The latter intervenes between layers in order to prevent heat from accumulating in build direction, while the former is called up during the deposition of each layer in order to prevent the overheating of its end portion.

At first , the energy input is adjusted by varying the EP/EN polarity ratio only. The wire feed speed (WFS) and travel speed (TS) are kept constant. In fact, the energy levels accessible by the variation of the EP/EN polarity ratio seem sufficient to correct the start/end deposition failures. The range of variation of this parameter is limited between -2 and +2, which corresponds to the polarity ratios for which the energy input varies the most, as seen in Figure 3.17.

As detailed in the previous chapter, the main cause behind the start/end deposition failures is the overheating of the start/end portions of the thin-wall part compared to its middle portion. This overheating is also characterized by an increase in substrate temperature on the final portion of each deposited layer (considering the zigzag deposition path) due to the bad heat dissipation conditions on these portions. In order to illustrate this further, the evolution of substrate temperature along the middle and the end portion of the 41th layer (along x-axis) is plotted in Figure 3.22 for strategy 2, and compared to its mean value. The substrate temperature remains relatively constant on the middle portion of the layer, but increases sharply when the layer comes to an end, with a difference that exceeds 100 °C compared to its middle portion, indicating the presence of a strong overheating phenomena. This overheating phenomena causes the droplets deposited on the final portion of each layer to be more spread out and collapsed, and can also causes the remelting of the previous layers, thus accentuating the deformation of the start/end portions of the thin-wall part.

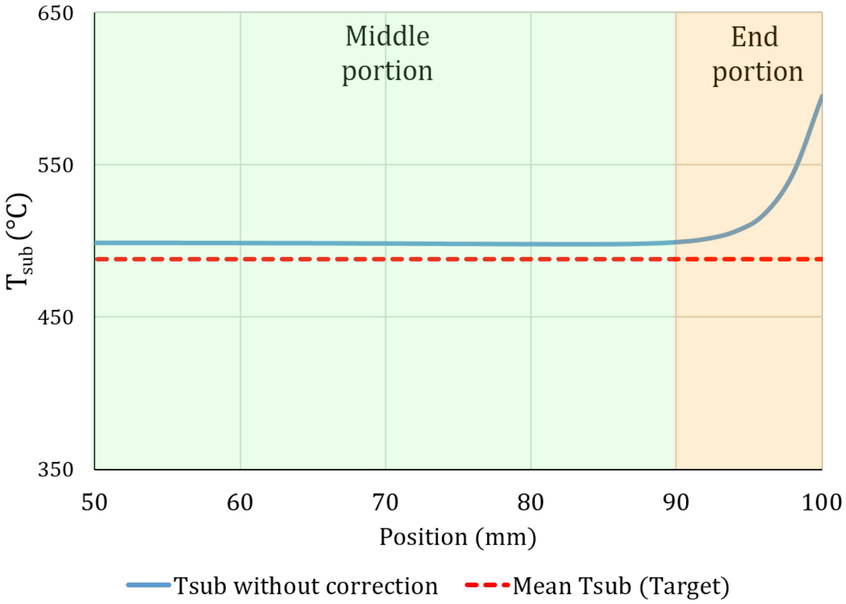

Figure 3.22: Tsub evolution over a layer

The objective of the proposed simulation-based energy optimization technique is to adjust the energy input of the deposited droplets at the end portion of the layer, in order to bring the layer's substrate temperature curve, represented by the blue continuous curve in Figure 3.22, as close as possible to the mean substrate temperature of the layer, represented by the red dotted curve. Thus ensuring the same deposition conditions between the middle and the final portions of each deposited layer. To do so, an optimization function taking the form of a proportional-derivative (P-D) controller is integrated into the finite element simulation, allowing to select the appropriate EP/EN polarity ratios, and thus the energy input levels, of the droplets deposited at the end portion of each layer. The major steps of this technique, and the obtained results are detailed in the following sections.

3.6.1 Technique description

The proposed simulation-based energy-input optimization technique consists of a loop that is called up only during the deposition phase simulation, and is composed of three major steps, as outlined in Figure 3.23. These steps are repeated for each numerical droplet deposited during a given layer deposition phase:

- Simulation: First, the deposition of the *k-th* droplet is simulated using the finite element simulation, and the temperature field of the already deposited regions is obtained for the corresponding time-step t. Simulation is run according to the previously set deposition strategy parameters. In the present case, only EP/EN polarity ratio is varied, and all other parameters, such as wire feed speed, and travel speed are kept constant.

- Thermal criteria: Based on the obtained temperature field, the local substrate temperature, on which the next droplet will be deposited, is calculated using $\mathrm{T_{sub}}$criterion, and is called $\mathrm{T_{sub}}_{droplet}$. At the same time, the mean substrate temperature of the current layer is updated, and is called $\mathrm{T_{sub}}_{mean}$. The latter is simply the average of the local substrate temperatures on which the previous droplets were deposited. The set objective function is to minimize the difference between the mean substrate temperature of the layer, and the substrate temperature of the next droplet. Therefore, this difference, called $E_{\mathrm{T_{sub}}}$, is calculated at this step, and a decision is subsequently made based on its value. That is, if $E_{\mathrm{T_{sub}}}$ is small enough, the energy input is considered adequate, and the current EP/EN polarity ratio will be maintained for the deposition of the next droplet. Otherwise, i.e. in the case where $E_{\mathrm{T_{sub}}}$ is important, the optimization function will be called in the next step in order to adjust the energy input of the next deposited droplet.

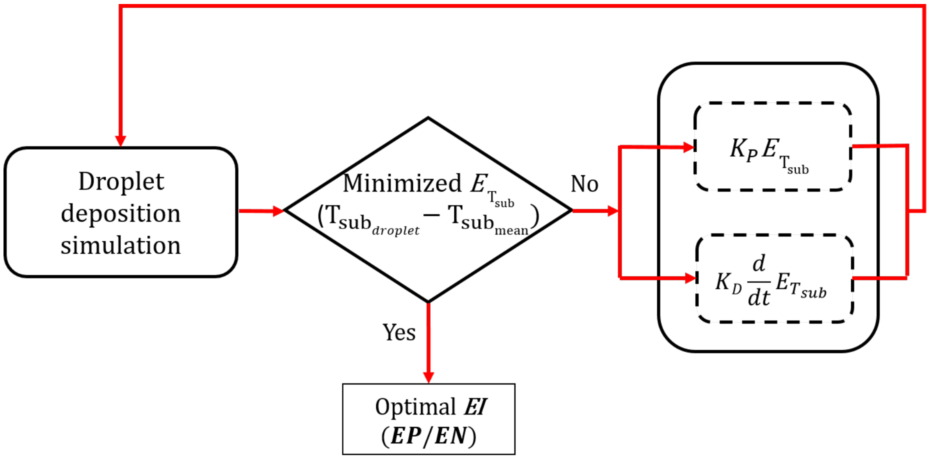

Figure 3.23: Simulation-based energy input optimization technique

- Energy-input optimization function: In the present case, the optimization function takes the form of a proportional-derivative (P-D) controller. This function enables to select the appropriate EP/EN polarity ratio, and therefore the appropriate energy input, for the next deposited droplet. The energy input level is decreased, increased, or maintained depending on the magnitude of the error $E_{\mathrm{T_{sub}}}$, and the derivative of the error $\frac{d}{dt}E_{Tsub}$,as shown in Table 3.6. The deposition of *(k + 1)*th droplet will be simulated afterwards with the new selected energy input.

$E_{T_{sub}} > 0$		
$\frac{d}{dt}E_{T_{sub}} < k_1$	$k_1 < \frac{d}{dt}E_{T_{sub}} < k_2$	$\frac{d}{dt}E_{T_{sub}} > k_2$
EP/EN	EP/EN+	EP/EN++
$E_{T_{sub}} < 0$		
$\frac{d}{dt}E_{T_{sub}} > -k_1$	$-k_2 < \frac{d}{dt}E_{T_{sub}} < -k_1$	$\frac{d}{dt}E_{T_{sub}} < -k_2$
EP/EN	EP/EN-	EP/EN--

Table 3.6: EP/EN P-D controller

3.6.2 Validation test case

In order to verify the effectiveness of the proposed simulation-based energy-input optimization technique, the test-case carried out in section 3.4.2 is hereby repeated. Only this time, the thin-wall part is manufactured according to a third deposition strategy, where both idle-times and energy input are optimized. To do so, both idle-time and energy-input optimization techniques are called-up simultaneously, and the thin-wall part is manufactured according to the obtained deposition strategy. The latter is compared to the part manufactured according to strategy 2, where only idle-times are optimized. The parameters of both deposition strategies are listed in Table 3.7, and the results are detailed in the following section.

	Trajectory	TS (mm/s)	WFS (m/min)	Idle time (s)	EP/EN	EI (J/mm)
Strategy 2	Zigzag	10	5	Variable	+1	77.8
Strategy 3	Zigzag	10	5	Variable	Variable	Variable

Table 3.7: Test-case strategies parameters

3.6.3 Results

3.6.3.1 Energy-input and idle-time evolution

Layer portion	Layer number				
	1	2	3	4 and 5	6 to 60
[0, 88] mm	+1	+1	+1	+1	+1
[88, 90] mm	0	+1	0	0	0
[90, 92] mm	0	+1	0	0	0
[92, 94] mm	+1	+1	0	+1	+1
[94, 96] mm	-2	-1	0	-2	-2
[96, 98] mm	-2	-1	-1	-2	-2
[98,100] mm	-2	0	0	-1	-2

Table 3.8: EP/EN polarity ratio results of strategy 3

The simulation-based energy optimization results in terms of EP/EN polarity ratios are listed in Table 3.8, and the resulted energy-input curves are shown in

Figure 3.24. In order to facilitate the reading of the results, the EP/EN polarity ratio and the energy-input levels are varied as a function of the layer's portion, regardless of the deposition direction. In other words, each layer starting point is pointed at 0 mm, and its end point is at 100 mm.

As expected, the EP/EN polarity ratio is kept constant (EP/EN = +1) throughout the middle portion of the different layers, i.e. the section between 0 mm and 88 mm. From this point, the EP/EN polarity ratio, and thus the energy-input, is adjusted due to the increase in the substrate temperature at the layers end portions. The way EP/EN polarity ratio is adjusted is different for the first five layers due to the strong heat sink effect, which corresponds to the first region of the idle-time evolution curve. In this transitional region, the layers average substrate temperature, and more importantly, the increase in the substrate temperature at the end portion of the layers, behaves differently from one layer to another, due to the progressive change in the cooling rate. From the sixth layer, the EP/EN parameter is adjusted in the same manner, because the increase in substrate temperature at the end portion of the layers is almost identical in the second region of the idle-time curve.

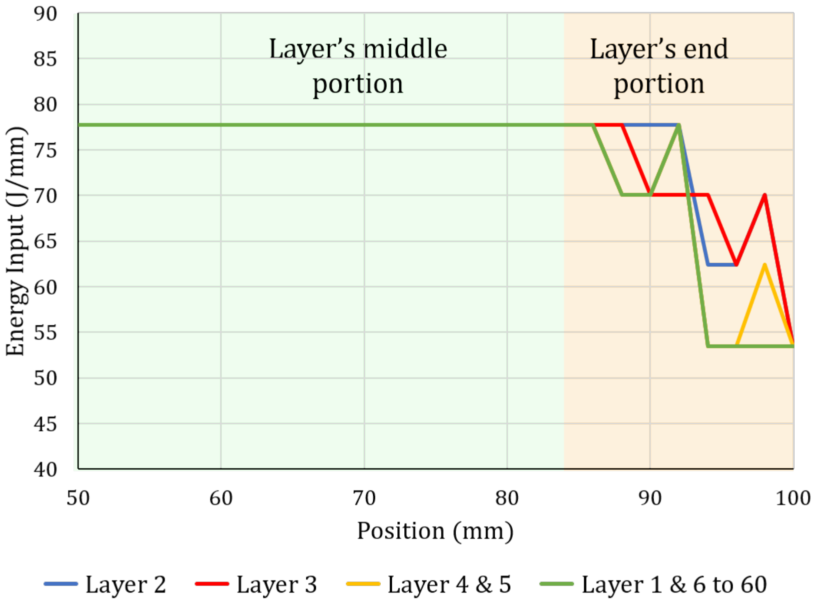

Figure 3.24: Energy input evolution in strategy 3

Figure 3.25 shows the results of the idle time calculation for strategies 2 and 3. As shown in the figure, the idle-time curve of strategy 3 follows the same trend as in strategy 2, describing the two heat dissipation modes described in Section 3.4.3.1. Except that, the idle-times of strategy 3 are slightly shorter than those of strategy 2, due to the reduced energy input on the final portions of the layers. The difference between the two curves is almost constant, and is equal to 7 seconds.

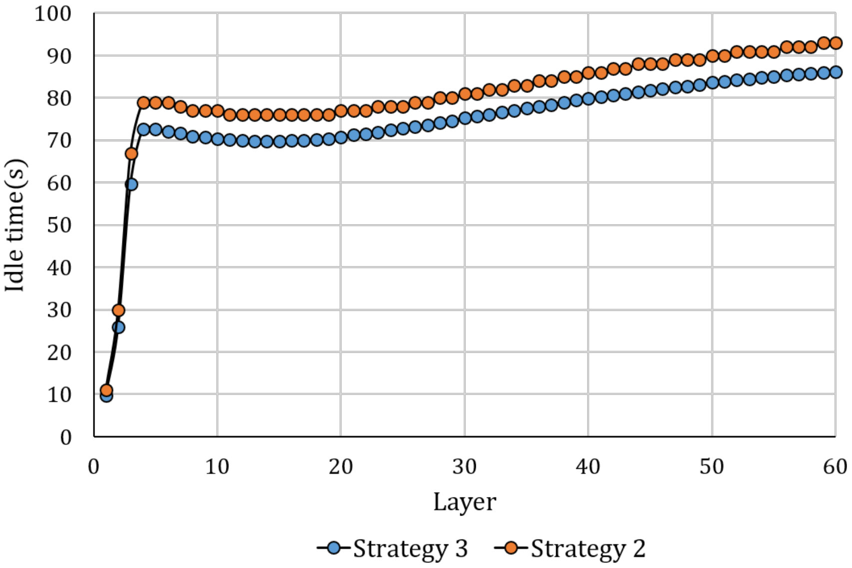

Figure 3.25: Idle-time evolution in strategy 2 and 3

3.6.3.2 Thermal quality criteria

Substrate temperature (T_{sub})

The evolution of substrate temperature along the middle and end portions of the 41th layer (along x-axis) under strategy 2 and strategy 3 is shown in Figure 3.26. As intended, the variation of EP/EN polarity ratio in strategy 3 allowed to reduce the substrate temperature gap between the middle and the end portion of the layer compared to strategy 2. Thanks to the proportional-derivative optimization function, the substrate temperature could be brought closer to its target value on the final portion of the layer. Indeed, the T_{sub} curve of strategy 3 is shown to oscillates around its target value on the end portion of layer, in contrast to strategy 2 where the T_{sub} curve increases continuously. This result indicates that the deposition conditions on the end portions of the layers have been clearly improved and that the overheating phenomenon has been reduced.

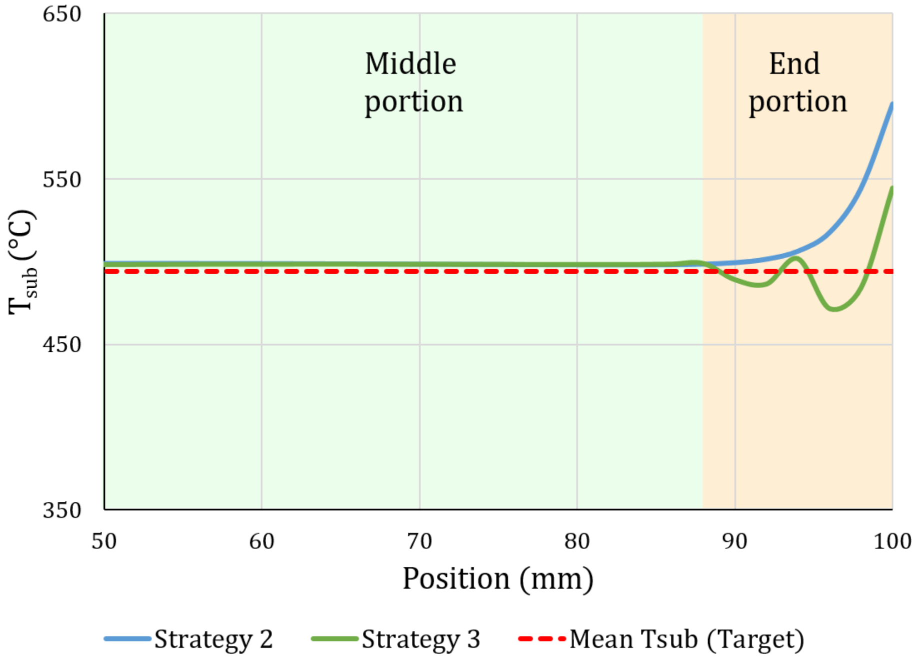

Figure 3.26: Comparison of substrate temperature evolution over the 41th layer of strategy 2 & 3

Maximum temperature (T_{max})

In order to investigate the effectiveness of the proposed energy-input optimization technique in reducing the overheating of the start/end portions of the thin-wall part, the maximum temperature (T_{max}) criterion is calculated for strategy 3 and compared to that of strategy 2. The results are shown in Figure 3.27. As detailed earlier in section 3.4.3.2, the proposed idle-time optimization technique allowed to ensure a constant T_{max} over the largest middle portion of the thin-wall part, but did not allow to eliminate the overheating of the start/end portion of the part, as can be seen in Figure 3.27.a. However, the optimization of the energy-input on the end portion of the layers allowed to tackle this issue. As can be seen in Figure 3.27.b, the T_{max} criterion is shown to be constant on all portions of the thin-wall part. This implies that the overheating of the start/end portions of the part has been significantly reduced. Therefore, the start/end deposition failures present on the part manufactured according to strategy 2 is expected to be significantly improved by adopting strategy 3.

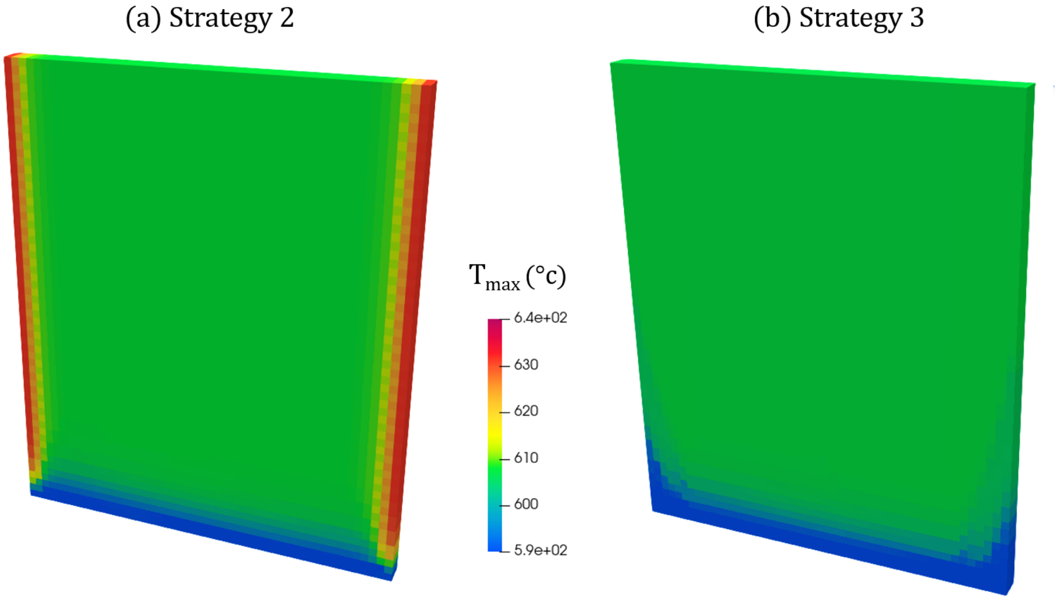

Figure 3.27: Results of maximum temperature criterion (T_{max}) for: (a) strategy 2 and (b) strategy 3

3.6.3.3 Fabricated thin-wall parts

The actual thin-wall parts manufactured according to strategy 2 and strategy 3 are shown in Figure 3.28. As shown in the figure, the start/end deposition failures observed on the thin-wall part manufactured according to strategy 2 has been corrected in strategy 3. Indeed, the height difference between the start/end portions and the middle portion of the thin-wall part has been significantly minimized compared to strategy 2, which further validates the effectiveness of the proposed energy-input optimization technique.

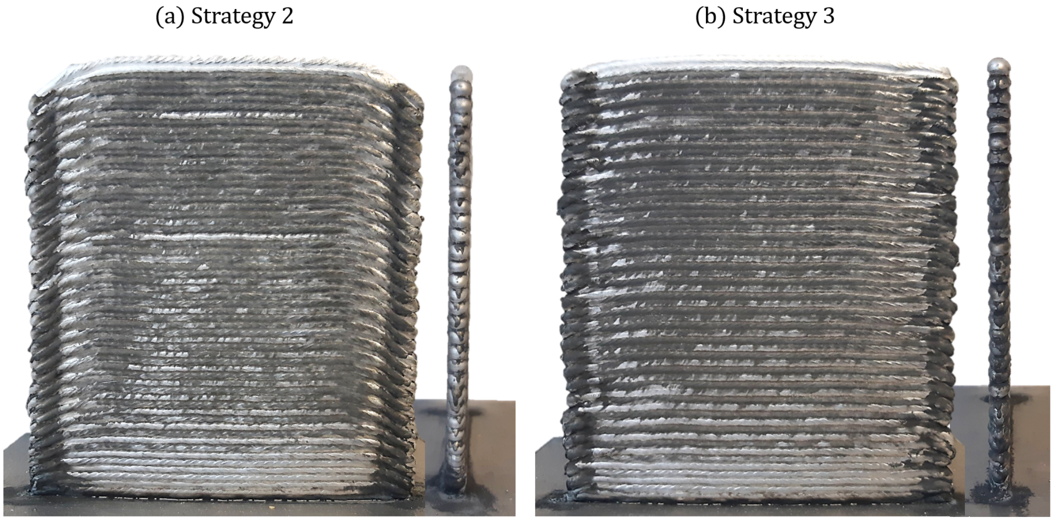

Figure 3.28: Thin-wall part fabricated according to (a) strategy 2; (b) strategy 3

3.7 Conclusion

This chapter proposes a simulation-based approach for deposition strategies optimization in WAAM process. The proposed approach integrates the previously developed thermal simulation and thermal quality criteria with the objective of improving the quality of the produced parts in terms of geometric accuracy and material properties. Based on this approach, two simulation-based deposition strategy optimization techniques were proposed. In these techniques, two different strategy parameters are adjusted with the aim of dictating the desired thermal history in the fabricated parts, namely: the idle-times between layers, and the energy-input. The combination of the two techniques allowed to improve the quality of the thin-walled part, as verified by the different thermal quality criteria and the actual manufactured parts. That is:

- The idle-time optimization technique allowed to prevent heat accumulation in build direction, and ensured a low and constant molten-pool size along this direction, which made it possible to guarantee a constant part width and a low and constant porosity rate along build direction.

- The energy-input optimization technique allowed to prevent the overheating of the start/end portions of the thin-wall part, which enabled to correct the start/end deposition failures.

In this chapter, it has been proven that with the use of the proposed thermal simulation and quality criteria, it is possible to evaluate and optimize WAAM deposition strategies, and improve the quality of the produced parts . This optimization appears to be difficult to achieve experimentally. Moreover, the number of experiments needed to find the optimal deposition strategy would have been very important.

Conclusions and perspectives

Conclusions

In this thesis, it has been proven that the quality of WAAM produced parts is strongly influenced by their thermal history, mainly dictated by deposition strategies. Therefore, this work's aim was **to guarantee the quality of WAAM deposited parts by controlling and optimizing their deposition strategies**. In order to achieve such goal, a simulation-based strategy evaluation and optimization approach was proposed. This approach is based on three main stages, including the thermal simulation of the process, the thermal quality criteria, and deposition strategy optimization. Each of the stages was the subject of one of the three chapters of this manuscript, and allowed the three underlying questions of the thesis to be answered.

The finite element modelling techniques proposed in Chapter 1, including material and heat input, boundary conditions, and material properties modelling techniques, provided a valid and rapid simulation for WAAM process. Thanks to the proposed model, it is possible **to simulate the thermal history of an entire WAAM deposition strategy in a reasonable time and with sufficient accuracy allowing for its off-line optimization**.

The review of WAAM literature, presented in Chapter 2, has allowed the most encountered defects in WAAM of thin-walled structures to be characterized and their thermal causes to be identified. On the basis of this characterization, and with the aid of the proposed thermal simulation, a set of thermal quality criteria were proposed. These criteria enables to track the thermal phenomena at the origin of these defects, and thus **to evaluate the quality of WAAM produced parts in terms of geometric accuracy and material integrity using process simulation**.

The development of the two previous stages led to the successful implementation of the proposed simulation-based strategy optimization approach. In chapter 3, proposals for simulation-based strategy optimization techniques have been developed and tested. The proposed techniques allowed to dictate the desired thermal history in the manufactured parts by adjusting their deposition strategy parameters along the deposition path, which improved the quality of the final parts. Overall, it has been proven that **with the use of the proposed thermal simulation and quality criteria, it is possible to evaluate and optimize WAAM deposition strategies, and improve the quality of the produced parts**.

Contributions

Development of a novel FE thermal simulation for WAAM process

A valid finite element simulation is proposed in order to investigate the thermal behavior of WAAM process in a reasonable time. The proposed model is based on a novel element deposition technique allowing to incorporate the metal deposition feature of the process into the modelling of material input, heat input, and boundary conditions. Indeed, this element deposition technique enables, for each deposition time-step, to add new elements to the previous mesh, following the passage of an adapted heat source, which allows to model both material and heat input properly, and to better consider heat exchange in the external surfaces. Moreover, a creative latent heat modelling technique is proposed in order to overcome temporary shortcomings in phase change modeling algorithms.

Overall, the proposed thermal simulation enables to simulate an entire WAAM deposition strategy within a reasonable time, and with the sufficient precision required for its optimization.

Development of a set of thermal quality criteria for WAAM produced parts

A set of thermal quality criteria are proposed, allowing off-line evaluation of the quality of WAAM fabricated parts in terms of geometric accuracy and material integrity. Calculated using the finite element simulation, T_{sub}, ATAS, T_{max}, and MPV criteria allow to track the thermal phenomena at the origin of the most common defects in WAAM of thin-walled structures, namely, the dimensional accuracy, deposition failures, and porosity.

Moreover, the proposed criteria can be used both to evaluate the quality of the parts and the relevance of their deposition strategies, but also to minimize these defects when integrated into optimization algorithms.

Proposition of a simulation-based deposition strategy optimization approach for WAAM process

A simulation-based approach is developed for the optimization of WAAM deposition strategies. The proposed optimization techniques allow to adjust both idle-times between layers and energy-input, based on the results of the thermal simulation, and the set substrate temperature criterion ($\mathrm{T}_{\mathrm{sub}}$). The proposed techniques make it possible to prevent from heat accumulation and overheating phenomena, responsible for the variation of layers dimensions along build direction and the start/end deposition failures defects, often encountered in WAAM of thin-walled parts. Therefore, it is possible, thanks to the proposed optimization tool, to guarantee the quality of WAAM produced parts while reducing time and costs.

Perspectives

The work presented in this manuscript can be continued and further improved. Some of the areas to be explored are presented in the following.

Development of a simulation software for WAAM process

The proposed finite element simulation allowed the off-line optimization WAAM process in a reduced time and at a lower cost thanks to the different modelling techniques described in this manuscript. Nevertheless, the implementation of these techniques remains difficult when using commercial simulation softwares. For this reason, the proposed model has been implemented using the finite element code Cast3M, as the latter offers great programming flexibility and allows the integration of optimization and correction algorithms. However, the use of Cast3M requires a good knowledge of Gibiane programming language, and is not necessarily convenient for all final users. Therefore, the development of a simulation environment with a graphical software interface would allow a more simplified usage of the proposed simulation. This could be the subject of a future computer development work which would facilitate the use of the simulation by a greater number of users.

In addition, further computer development would allow further improve the performance and robustness of the simulation and reduce the computational time. For instance, by integrating new functionalities and model reduction techniques.

Further development of the thermal quality criteria

The use of thermal quality criteria has proven to be an effective approach in off-line defect prediction and deposition strategies optimization. However, the proposed criteria can only detect three quality defects, namely dimensional accuracy, start/end deposition failures, and porosity. WAAM manufactured parts are subject to other quality issues, such as humping and microstructure evolution. The development of broad thermal quality criteria capable of predicting such quality aspects can be very useful in the process of improving the quality of WAAM parts.

Furthermore, in the context of this work, the proposed quality criteria are designed to predict whether or not these defects will appear, and although they make it possible to monitor the evolution of a given defect, they do not make it possible to quantify the defect precisely. One prospect for improvement would be to enable these criteria to assess defects with precision.

The development of new deposition strategy optimization algorithms

The proposed simulation-based strategy optimization techniques are shown to be effective in improving the quality of simple thin-walled parts produced by WAAM. This demonstrates the potential of the proposed approach in increasing the performance of WAAM process both in terms of quality and productivity, and raises the prospect of several future works:

- The proposed techniques can be further improved and adapted for strategy optimization of more complex thin-walled structures.
- The use of the molten pool volume criterion (MPV) as an optimization criterion instead of the substrate temperature ($\mathrm{T}_{\mathrm{sub}}$) criterion could also be the subject of future work. The use of MPV would allow to control the size of the molten pool along the deposition path, and could also be further integrated in real-time strategy optimization techniques, using Infrared (IR) cameras.
- New optimization functions can be developed to optimize other strategy parameters such as deposition paths or wire feed speeds, thanks to the

flexibility of the proposed simulation. Also, functions allowing to optimize all strategy parameters simultaneously would allow to better respect the set quality criteria and further improve the quality of the parts and reduce manufacturing times.

Application to other direct energy deposition processes

In this manuscript, the focus was on the simulation and optimization of WAAM process. However, this process is very similar to other direct energy deposition processes, such as Laser Engineered Net Shaping (LENS). Therefore, the different stages of the proposed simulation-based optimization approach can be used for these processes, including simulation, thermal quality criteria, and strategy optimization techniques. On the other hand, the differences in the processes characteristics, such as the nature of the energy source, and material feed stock, require an adaptation of the proposed models, or rather a generalization of the latter. This would then make it possible to have a simulation and an optimization tool for all DED processes.

Bibliography

Näsström, J., Brueckner, F., and Kaplan, A. F. H. (2019) Laser enhancement of wire arc additive manufacturing. *Journal of Laser Applications 31*, 022307.

Schoinochoritis, B., Chantzis, D., and Salonitis, K. (2016) Simulation of metallic powder bed additive manufacturing processes with the finite element method: A critical review. *Proceedings of the Institution of Mechanical Engineers, Part B: Journal of Engineering Manufacture 231*, 96–117.

Michaleris, P. (2014) Modeling metal deposition in heat transfer analyses of additive manufacturing processes. *Finite Elements in Analysis and Design 86*, 51–60.

Adebayo, A., J, J. M., and X, T. In *Limiting travel speed in additive layer manufacturing*; in Welding Research : Proceedings of the 9th International Conference on Trends in Welding Research June 4-8 2012 Chicago Illinois USA, T., Ed.; ASM International: Materials Park, Ohio, 2013.

Limousin, M., Martin, G., Lhuissier, P., Robert, P., Vignat, F., and Blandin, J. J. (2020) Effect of Wire Arc Additive Manufacturing (WAAM) processing parameters on microstructure and porosity in a 5000 Al alloy. *The 17th International Conference on Aluminum Alloys ICAA17*

Xu, F., Dhokia, V., Colegrove, P., McAndrew, A., Williams, S., Henstridge, A., and Newman, S. T. (2018) Realisation of a multi-sensor framework for process monitoring of the wire arc additive manufacturing in producing Ti-6Al-4V parts. *International Journal of Computer Integrated Manufacturing 31*, 785–798.

Nguyen, A.-T., Reiter, S., and Rigo, P. (2014) A review on simulation-based optimization methods applied to building performance analysis. *Applied Energy 113*, 1043–1058.

ISO/ASTM, (2015) ISO/ASTM 52900 Additive manufacturing - General principles -Terminology.

Wong, K. V., and Hernandez, A. (2012) A Review of Additive Manufacturing. *ISRN Mechanical Engineering 2012*, 1–10.

Vayre, B., Vignat, F., and Villeneuve, F. (2012) Designing for Additive Manufacturing. *Procedia CIRP 3*, 632–637.

Pour, M. A., Zanardini, M., Bacchetti, A., and Zanoni, S. (2016) Additive Manufacturing Impacts on Productions and Logistics Systems. *IFAC-PapersOnLine 49*, 1679–1684.

Zhang, Y., Bernard, A., Gupta, R. K., and Harik, R. (2014) Evaluating the Design for Additive Manufacturing: A Process Planning Perspective. *Procedia CIRP 21*, 144–150.

Bikas, H., Stavropoulos, P., and Chryssolouris, G. (2015) Additive manufacturing methods and modelling approaches: a critical review. *The International Journal of Advanced Manufacturing Technology 83*, 389–405.

Frazier, W. E. (2014) Metal Additive Manufacturing: A Review. *Journal of Materials Engineering and Performance 23*, 1917–1928.

Liberini, M., Astarita, A., Campatelli, G., Scippa, A., Montevecchi, F., Venturini, G., Durante, M., Boccarusso, L., Minutolo, F. M. C., and Squillace, A. (2017) Selection of Optimal Process Parameters for Wire Arc Additive Manufacturing. *Procedia CIRP 62*, 470–474.

Derekar, K. S. (2018) A review of wire arc additive manufacturing and advances in wire arc additive manufacturing of aluminium. *Materials Science and Technology 34*, 895–916.

Wu, B., Pan, Z., Ding, D., Cuiuri, D., Li, H., Xu, J., and Norrish, J. (2018) A review of the wire arc additive manufacturing of metals: properties, defects and quality improvement. *Journal of Manufacturing Processes 35*, 127–139.

Campocasso, S., Hugel, V., and Vayre, B. Génération de trajectoires pour la fabrication additive par dépôt de fil robotisé multi-axes - Application à une tubulure torique. 15ème Colloque national AIP-Primeca. La Plagne, France, 2017; pp 1–5.

Zhao, Y., Jia, Y., Chen, S., Shi, J., and Li, F. (2020) Process planning strategy for wire-arc additive manufacturing: Thermal behavior considerations. *Additive Manufacturing 32*, 100935.

Montevecchi, F., Venturini, G., Grossi, N., Scippa, A., and Campatelli, G. (2018) Idle time selection for wire-arc additive manufacturing: A finite element-based technique. *Additive Manufacturing 21*, 479–486.

Goldak, J., Chakravarti, A., and Bibby, M. (1984) A new finite element model for welding heat sources. *Metallurgical Transactions B 15*, 299–305.

Klocke, F., Beck, T., Hoppe, S., Krieg, T., Müller, N., Nöthe, T., Raedt, H.-W., and Sweeney, K. (2002) Examples of FEM application in manufacturing technology. *Journal of Materials Processing Technology 120*, 450–457.

F. Hosseinpour,, and H. Hajihosseini, (2009) Importance Of Simulation In Manufacturing.

Smith, J. S. (2003) Survey on the use of simulation for manufacturing system design and operation. *Journal of Manufacturing Systems 22*, 157–171.

Stavropoulos, P., and Foteinopoulos, P. (2018) Modelling of additive manufacturing processes: a review and classification. *Manufacturing Review 5*, 2.

Parandoush, P., and Hossain, A. (2014) A review of modeling and simulation of laser beam machining. *International Journal of Machine Tools and Manufacture 85*, 135–145.

Foteinopoulos, P., Papacharalampopoulos, A., and Stavropoulos, P. (2018) On thermal modeling of Additive Manufacturing processes. *CIRP Journal of Manufacturing Science and Technology 20*, 66–83.

Ganeriwala, R., and Zohdi, T. I. (2016) A coupled discrete element-finite difference model of selective laser sintering. *Granular Matter 18*.

Xia, M., Gu, D., Yu, G., Dai, D., Chen, H., and Shi, Q. (2016) Influence of hatch spacing on heat and mass transfer, thermodynamics and laser processability during additive manufacturing of Inconel 718 alloy. *International Journal of Machine Tools and Manufacture 109*, 147–157.

Turner, M. J., CLOUGH, R. W., MARTIN, H. C., and TOPP, L. J. (1956) Stiffness and Deflection Analysis of Complex Structures. *Journal of the Aeronautical Sciences 23*, 805–823.

Madenci, E., and Guven, I. *The Finite Element Method and Applications in Engineering Using Ansys®*; Springer US, 2006.

Luo, Z., and Zhao, Y. (2018) A survey of finite element analysis of temperature and thermal stress fields in powder bed fusion Additive Manufacturing. *Additive Manufacturing 21*, 318–332.

Zeng, K., Pal, D., and Stucker, B. A review of thermal analysis methods in Laser Sintering and Selective Laser Melting. 2012.

Galati, M., and Iuliano, L. (2018) A literature review of powder-based electron beam melting focusing on numerical simulations. *Additive Manufacturing 19*, 1–20.

Stender, M. E., Beghini, L. L., Sugar, J. D., Veilleux, M. G., Subia, S. R., Smith, T. R., Marchi, C. W. S., Brown, A. A., and Dagel, D. J. (2018) A thermal-mechanical finite element workflow for directed energy deposition additive manufacturing process modeling. *Additive Manufacturing 21*, 556–566.

Yang, Q., Zhang, P., Cheng, L., Min, Z., Chyu, M., and To, A. C. (2016) Finite element modeling and validation of thermomechanical behavior of Ti-6Al-4V in directed energy deposition additive manufacturing. *Additive Manufacturing 12*, 169–177.

Graf, M., Pradjadhiana, K. P., HÃ€lsig, A., Manurung, Y. H. P., and Awiszus, B. Numerical simulation of metallic wire arc additive manufacturing (WAAM). 2018.

Xiong, J., Lei, Y., and Li, R. (2017) Finite element analysis and experimental validation of thermal behavior for thin-walled parts in GMAW-based additive manufacturing with various substrate preheating temperatures. *Applied Thermal Engineering 126*, 43–52.

Xiong, J., Li, R., Lei, Y., and Chen, H. (2018) Heat propagation of circular thin-walled parts fabricated in additive manufacturing using gas metal arc welding. *Journal of Materials Processing Technology 251*, 12–19.

Montevecchi, F., Venturini, G., Scippa, A., and Campatelli, G. (2016) Finite Element Modelling of Wire-arc-additive-manufacturing Process. *Procedia CIRP 55*, 109–114.

Ding, J., Colegrove, P., Mehnen, J., Ganguly, S., Almeida, P. S., Wang, F., and Williams, S. (2011) Thermo-mechanical analysis of Wire and Arc Additive Layer Manufacturing process on large multi-layer parts. *Computational Materials Science*

Montevecchi, F., Venturini, G., Grossi, N., Scippa, A., and Campatelli, G. (2017) Finite Element mesh coarsening for effective distortion prediction in Wire Arc Additive Manufacturing. *Additive Manufacturing 18*, 145–155.

Cast3M, http://www-cast3m.cea.fr/.

Hu, J., and Tsai, H. (2007) Heat and mass transfer in gas metal arc welding. Part I: The arc. *International Journal of Heat and Mass Transfer 50*, 833–846.

Dupont, J. N., and Marder, A. R. (1995) Thermal efficiency of arc welding processes. *Welding Journal 74*.

El-Sayed, M., Shash, A., and Abd-Rabou, M. (2018) Finite element modeling of aluminum alloy AA5083-O friction stir welding process. *Journal of Materials Processing Technology 252*, 13–24.

Li, F., Chen, S., Shi, J., Zhao, Y., and Tian, H. (2018) Thermoelectric Cooling-Aided Bead Geometry Regulation in Wire and Arc-Based Additive Manufacturing of Thin-Walled Structures. *Applied Sciences 8*, 207.

Bai, X., Zhang, H., and Wang, G. (2013) Improving prediction accuracy of thermal analysis for weld-based additive manufacturing by calibrating input parameters using IR imaging. *The International Journal of Advanced Manufacturing Technology 69*, 1087–1095.

Montevecchi, F., Venturini, G., Grossi, N., Scippa, A., and Campatelli, G. (2018) Heat accumulation prevention in Wire-Arc-Additive-Manufacturing using air jet impingement. *Manufacturing Letters 17*, 14–18.

Wu, B., Ding, D., Pan, Z., Cuiuri, D., Li, H., Han, J., and Fei, Z. (2017) Effects of heat accumulation on the arc characteristics and metal transfer behavior in

Wire Arc Additive Manufacturing of Ti6Al4V. *Journal of Materials Processing Technology 250*, 304–312.

Venturini, G., Montevecchi, F., Scippa, A., and Campatelli, G. (2016) Optimization of WAAM Deposition Patterns for T-crossing Features. *Procedia CIRP 55*, 95–100.

Diourté, A., Bugarin, F., Bordreuil, C., and Segonds, S. (2021) Continuous three-dimensional path planning (CTPP) for complex thin parts with wire arc additive manufacturing. *Additive Manufacturing 37*, 101622.

Xiong, J., Zhang, G., and Zhang, W. (2015) Forming appearance analysis in multi-layer single-pass GMAW-based additive manufacturing. *The International Journal of Advanced Manufacturing Technology 80*, 1767–1776.

Xiong, J., Yin, Z., and Zhang, W. (2016) Forming appearance control of arc striking and extinguishing area in multi-layer single-pass GMAW-based additive manufacturing. *The International Journal of Advanced Manufacturing Technology 87*, 579–586.

Zhang, Y., Chen, Y., Li, P., and Male, A. T. (2003) Weld deposition-based rapid prototyping: a preliminary study. *Journal of Materials Processing Technology 135*, 347–357.

Manokruang, S., Vignat, F., Museau, M., and Limousin, M. Process parameters effect on weld beads geometry deposited by Wire and Arc Additive Manufacturing (WAAM). International Joint Conference on Mechanics, Design Engineering and Advanced Manufacturing (JCM 2020). Aix-en-Provence, France, 2020.

Nie, Y., Zhang, P., Wu, X., Li, G., Yan, H., and Yu, Z. (2018) Rapid prototyping of 4043 Al-alloy parts by cold metal transfer. *Science and Technology of Welding and Joining 23*, 527–535.

Bradstreet, B. (1968) Effect of Surface Tension and Metal Flow On Weld Bead Formation. *Weld. J. 47 314-322*

Xu, G., Cao, Q., Hu, Q., Zhang, W., Liu, P., and Du, B. (2016) Modelling of bead hump formation in high speed gas metal arc welding. *Science and Technology of Welding and Joining 21*, 700–710.

Yuan, L., Pan, Z., Ding, D., He, F., van Duin, S., Li, H., and Li, W. (2020) Investigation of humping phenomenon for the multi-directional robotic wire and arc additive manufacturing. *Robotics and Computer-Integrated Manufacturing 63*, 101916.

Jia, C., Liu, W., Chen, M., Guo, M., Wu, S., and Wu, C. (2020) Investigation on arc plasma, droplet, and molten pool behaviours in compulsively constricted WAAM. *Additive Manufacturing 34*, 101235.

Colegrove, P. A., Coules, H. E., Fairman, J., Martina, F., Kashoob, T., Mamash, H., and Cozzolino, L. D. (2013) Microstructure and residual stress improvement in wire and arc additively manufactured parts through high-pressure rolling. *Journal of Materials Processing Technology 213*, 1782–1791.

Wu, B., Pan, Z., Chen, G., Ding, D., Yuan, L., Cuiuri, D., and Li, H. (2019) Mitigation of thermal distortion in wire arc additively manufactured Ti6Al4V part using active interpass cooling. *Science and Technology of Welding and Joining 24*, 484–494.

Hönnige, J., Colegrove, P., Ganguly, S., Eimer, E., Kabra, S., and Williams, S. (2018) Control of residual stress and distortion in aluminium wire mathplus arc additive manufacture with rolling. *Additive Manufacturing 22*, 775–783.

Sames, W. J., List, F. A., Pannala, S., Dehoff, R. R., and Babu, S. S. (2016) The metallurgy and processing science of metal additive manufacturing. *International Materials Reviews 61*, 315–360.

Bordreuil, C., and Niel, A. (2014) Modelling of hot cracking in welding with a cellular automaton combined with an intergranular fluid flow model. *Computational Materials Science 82*, 442–450.

Horgar, A., Fostervoll, H., Nyhus, B., Ren, X., Eriksson, M., and Akselsen, O. (2018) Additive manufacturing using WAAM with AA5183 wire. *Journal of Materials Processing Technology 259*, 68–74.

Bai, J., Ding, H. L., Gu, J. L., Wang, X. S., and Qiu, H. (2017) Porosity evolution in additively manufactured aluminium alloy during high temperature exposure. *IOP Conference Series: Materials Science and Engineering 167*, 012045.

Lee, P., and Hunt, J. (2001) Hydrogen porosity in directionally solidified aluminium–copper alloys: a mathematical model. *Acta Materialia 49*, 1383–1398.

Hwang, L.-R., Gung, C.-H., and Shih, T.-S. (2001) A study on the qualities of GTA-welded squeeze-cast A356 alloy. *Journal of Materials Processing Technology 116*, 101–113.

Cong, B., Ding, J., and Williams, S. (2014) Effect of arc mode in cold metal transfer process on porosity of additively manufactured Al-6.3%Cu alloy. *The International Journal of Advanced Manufacturing Technology 76*, 1593–1606.

Fang, X., Zhang, L., Li, H., Li, C., Huang, K., and Lu, B. (2018) Microstructure Evolution and Mechanical Behavior of 2219 Aluminum Alloys Additively Fabricated by the Cold Metal Transfer Process. *Materials 11*, 812.

Rodrigues, T. A., Duarte, V., Miranda, R., Santos, T. G., and Oliveira, J. (2019) Current Status and Perspectives on Wire and Arc Additive Manufacturing (WAAM). *Materials 12*, 1121.

Tapia, G., and Elwany, A. (2014) A Review on Process Monitoring and Control in Metal-Based Additive Manufacturing. *Journal of Manufacturing Science and Engineering 136*.

Yang, D., Wang, G., and Zhang, G. (2017) Thermal analysis for single-pass multilayer GMAW based additive manufacturing using infrared thermography. *Journal of Materials Processing Technology 244*, 215–224.

da Silva, L. J., Souza, D. M., de Araújo, D. B., Reis, R. P., and Scotti, A. (2020) Concept and validation of an active cooling technique to mitigate heat accumulation in WAAM. *The International Journal of Advanced Manufacturing Technology 107*, 2513–2523.

Xiong, J., Yin, Z., and Zhang, W. (2016) Closed-loop control of variable layer width for thin-walled parts in wire and arc additive manufacturing. *Journal of Materials Processing Technology 233*, 100–106.

Mathey, E. Automatic optimization of the cooling of injection mold based on the boundary element method. AIP Conference Proceedings. 2004.

Béraud, N., Vignat, F., Villeneuve, F., and Dendievel, R. (2017) Improving dimensional accuracy in EBM using beam characterization and trajectory optimization. *Additive Manufacturing 14*, 1–6.

Beraud, N. Fabrication assistée par ordinateur pour le procédé EBM. Theses, Université Grenoble Alpes, 2016.

Vignat, F., Béraud, N., and Villeneuve, F. (2017) Simulation based optimized beam velocity in additive manufacturing. *Journal of Physics: Conference Series 885*, 012016.

Lei, Y., Xiong, J., and Li, R. (2018) Effect of inter layer idle time on thermal behavior for multi-layer single-pass thin-walled parts in GMAW-based additive manufacturing. *The International Journal of Advanced Manufacturing Technology 96*, 1355–1365.

Karunakaran, K., Suryakumar, S., Pushpa, V., and Akula, S. (2010) Low cost integration of additive and subtractive processes for hybrid layered manufacturing. *Robotics and Computer-Integrated Manufacturing 26*, 490–499.

Ding, J., Colegrove, P., Mehnen, J., Williams, S., Wang, F., and Almeida, P. S. (2013) A computationally efficient finite element model of wire and arc additive manufacture. *The International Journal of Advanced Manufacturing Technology 70*, 227–236.

Shi, J., Li, F., Chen, S., Zhao, Y., and Tian, H. (2018) Effect of in-process active cooling on forming quality and efficiency of tandem GMAW–based additive manufacturing. *The International Journal of Advanced Manufacturing Technology 101*, 1349–1356.

Wu, B., Pan, Z., Ding, D., Cuiuri, D., Li, H., and Fei, Z. (2018) The effects of forced interpass cooling on the material properties of wire arc additively manufactured Ti6Al4V alloy. *Journal of Materials Processing Technology 258*, 97–105.